The boundary of the subducting slab and mantle wedge of an incipient arc: *P-T-D* history, mixing, and fluid-related processes recorded in the Dalrymple Amphibolite, Palawan Ophiolite (the Philippines)

Gabriel Theophilus V. VALERA

Doctoral Thesis submitted to
Department of Geology and Mineralogy,
Division of Earth and Planetary Sciences,
Graduate School of Science,
Kyoto University

January 31, 2022

Abstract

The boundary between the subducting slab and the overlying mantle wedge is a dynamically evolving site of complex physical and fluid-related chemical processes. The nature of these processes and the lithologies comprising this slab-mantle wedge boundary also changes at different stages of subduction, i.e. initiation, incipient, and mature. In this contribution, the pressure-temperature-deformation (*P-T-D*) history and petrogenesis of the Dalrymple Amphibolite in Palawan Island, Philippines is investigated. The Dalrymple Amphibolite occurs below the residual mantle peridotites of the Palawan Ophiolite composed of dunite and harzburgite interlayers. The Amphibolite exhibits a block-in-matrix fabric consisting of metamafic and minor metasedimentary blocks surrounded by a highly sheared matrix (kyanite + Ca-amphibole + biotite + ilmenite ± garnet).

Zr-in-rutile geothermometry and quartz-in-garnet geobarometry of the garnet amphibolite block revealed the *P-T* conditions of the prograde metamorphism of the blocks from ~625 °C, 11.5 kbar to ~700 °C, 13 kbar. The Zr-in-rutile geothermometer and the TZARS geobarometer, utilizing the equilibrium of clinozoisite + rutile + quartz = anorthite + titanite + H_2O, further indicated comparable peak metamorphic conditions for the amphibolite and epidote amphibolite (~605–710 °C, 10–13 kbar) blocks. Geothermobarometry of the matrix surrounding the blocks revealed similar peak metamorphic conditions of ~700 °C and 13 kbar to the garnet amphibolite blocks.

The paleogeothermal gradient preserved in the Dalrymple Amphibolite (~16 °C/km) and its block-in-matrix structure are atypical of metamorphic soles, and are more akin to high-*T* eclogites which typically exhibit a mélange occurrence and interpreted to have formed during incipient subduction. These *P-T* estimates and its block-in-matrix structure suggest that the Dalrymple Amphibolite likely represents the slab-mantle wedge interface of a young arc complex already transitioning from the much warmer paleogeothermal gradients of the slab-mantle wedge interface when subduction was first initiated. The similar peak metamorphic conditions constrained in the matrix and the metamafic blocks in the Dalrymple Amphibolite indicate that the matrix-forming deformation started before the sequence reached peak metamorphic conditions at depths of around 45 km.

The whole-rock composition of the blocks and the surrounding matrix of the Dalrymple Amphibolite is furthermore utilized to determine the protolith of the blocks and the effect of mechanical mixing and fluid infiltration in the sheared matrix of this fossil slab-mantle wedge interface. The major and trace element contents of the metamafic blocks indicate a mid-oceanic ridge basalt origin similar to the mafic lavas of the crustal section of Palawan Ophiolite. Similarities in their rare earth element (REE) and trace element patterns indicate the genetic relationship between the two mafic sequences. This confirms that the metamafic blocks represent the basalt to gabbro section of the oceanic lithosphere of the subducting slab.

The matrix surrounding the blocks exhibit highly variable phase assemblage. In order to determine its petrogenesis, we distinguished groups of components/elements which behave similarly (Group 1 TiO_2, Al_2O_3, Zr, Th and the light REEs; Group 2 Cr, Ni and MgO) based on geostatistical (correlation coefficient) analysis. These groups indicate mixing of metasedimentary (Group 1) and metamafic (Group 2) end-members to form the matrix. The mixing proportions of the end-members were estimated by employing regression analysis wherein the measured concentration of fluid immobile elements/components (Cr, Ni, Zr, TiO_2 and Al_2O_3) in the matrix samples were fitted against a modelled concentration by changing the end-member and their relative proportions. The end-members and mixing ratio with the highest regression value (r^2) was selected to obtain the modelled composition of the matrix. The modelled and the measured matrix compositions were then used as the original (unmetasomatized) rock and the altered rock respectively in the isocon analysis, assuming that TiO_2, Al_2O_3, Cr, Nd, Zr, and Hf are immobile. This assumption is supported by the prevalence of kyanite, ilmenite and zircon in the matrix mineral assemblage.

This procedural workflow helped distinguish end-member components, estimate their mixing ratios, and determine the effects of infiltrating fluids. In particular, the whole-rock composition of the matrix was controlled by mixing of a subordinate amount of metamafic blocks in a metasedimentary-dominated shear zone. This is supported by the Cr-Nb content of rutile grains included in the matrix samples which indicate mixed metamafic and metapelitic signatures. The metamafic-metasedimentary dominated matrix in the Dalrymple Amphibolite contrasts with other

high-pressure/temperature (*P/T*) type metamorphic terranes which are dominated by low-*T* minerals (serpentine, Mg-chlorite, and talc) derived from an ultramafic end-member, and could be reflective of conditions in warmer subduction zones.

Mass balance calculations further revealed that an early fluid infiltration event likely occurred following the mixing process. This preferentially leached out elements which are either fluid-mobile (e.g. CaO and SiO_2) or are not incorporated into the growing minerals in the matrix. The strong control of mineral assemblage of the matrix in its chemistry is exhibited by a number of samples which showed variable degrees of losses and gains in elements traditionally interpreted to be fluid immobile (e.g. heavy REEs and Y). A later advection event linked to retrograde stage, imprinted gains of K_2O, Rb, and Ba in the matrix samples with the growth of replacive minerals (e.g. muscovite after kyanite). This later fluid infiltration event possibly masked the original loss of these fluid-mobile elements in the matrix samples during the earlier fluid-rock interaction.

The Dalrymple Amphibolite was originally regarded as simply the metamorphic sole of the Palawan Ophiolite. Field investigation, geothermobarometric data, and mineral and whole-rock geochemical analyses presented in this study however tell a more complex story involving slivers of the subducting slab undergoing deformation, high-grade metamorphism, mechanical mixing, and infiltration by multiple generation of fluids. All these processes, transpiring in the slab-mantle wedge interface of an arc in its infancy. Subduction zones with similar geothermal gradients (e.g. warm subduction zones) possibly share these petrological characteristics.

Acknowledgement

This decade old dream to learn metamorphic petrology concluding with this doctorate degree would not have come to realization without the people who pushed me, walked with me, and guided my hand throughout the journey. The author would like to express his sincere gratitude to the following people:

Tetsuo Kawakami-sensei for patiently teaching me from scratch, the ways of metamorphic petrology. Where I am now would not have been possible without your guidance. I am forever grateful;

Betchaida Payot for continuously supporting me as a mentor 3000 kms away;
Takao Hirajima-sensei, Kosuke Naemura-san, *Fumiko Higashino-san*, *Kenta Yoshida-san* for the fruitful discussions which helped me formulate and refine this thesis one working hypothesis at a time;

My thesis panel *Takahiro Tagami-san, Yohei Igami-san* for the comments, questions and suggestions which helped improve this work;

Hiroe Ito-san for the administrative support and *Masaki Takaya-san* for the high quality thin sections that served as the building block of this thesis;

My labmates since D1, *Kota Suzuki* and *Ayu Yamazaki*, for all your help with the machines and, equally important, your friendship. Adjusting to life here in Japan became alot easier thanks to you.

My Filipino support group: *Kim Castro, Kim Garcia, Kevin Cruzado, Pia Medrano, Julius Garcia, and Rhu Mohammad* with whom I shared stories and memories I will forever treasure;

Housemates *Roberto Espinoza, Niku Guinea* & Misasagi friends *Marcello Savassi, Chong Shin Yit, George Nana Yaw* among others for all the experiences shared, difficult times conquered together;

Gaijin group: *Leila Navasal Bouillet, Francesca Giangrandi, Alexis Sandes, Gabo Nuñez, Arantxa Ramos* and all the other *"Sanjō University scholars"*. By all accounts, the last year of PhD would've been the hardest. Luckily I've met you all and Spring 2021–Winter 2022 turned out instead to be the most memorable and interesting thus far. For all the memories generated on the last leg of this journey, thank you very much. 'til our next kanpai;

My family *Nanay, Tatay, Ate, Ditse, Kuya, Sansi, Ate Angel, Ditsenem, Sansi Aza, Ate Riarose, Diko, Elbien, SJ, Phia, Massi, Lucluc, Dutdut, and Gadiel* for supporting this endeavor, and understanding my absence. Your encouragement is the cornerstone upon which this dream was built;

H-Kuma for being the light on my darkest hour and seeing this dream all the way through. I love us!

The great Architect of this life, for once again providing me with everything and everyone that I needed to grow and to conquer my insecurities and weaknesses. The road was never easy, so thank you for the strength and fortitude to continue pushing forward, albeit with small steps at times.

Table of contents

Preface

Island arc magmatism remains an enigmatic element of the Earth system manufacturing magmatic products with petrological characteristics not found in other tectonic settings (e.g. Tatsumi, 2005). These unique products are ultimately linked with the formation and growth of the continental crust (e.g. Debari and Greene, 2011). Such unique characteristics of arc magmas (e.g. calc-alkaline lavas) are attributed to the crustal components derived from the subducting slab which interacts with the overlying mantle wedge (Fig. 1a-b). These components are traditionally interpreted to be mobilized via fluids and/or melts derived from the slab's mafic and sedimentary crustal section (e.g. Pearce and Cann, 1971; Elliot, 2003; Fig. 1a). This recycling process likely occurs as the slab subducts and undergoes devolatilization and/or partial melting during prograde metamorphism (i.e. Kawamoto et al., 2012; Schmidt and Poli, 2014). An alternative model, however, argues that mixing between these crustal components in the slab-mantle wedge interface serves as an integral part of the process (e.g. Marschall and Schumacher, 2012; Fig. 1b). This is supported by empirical data from arc lavas (Nielsen and Marschall, 2017; Fig. 1c) and experimental analyses (Codillo et al., 2018; Fig. 1d). The postulated mixing between crustal and ultramafic components is also consistent with observations on fossil slab-mantle wedge interface localities, mostly high-*P/T* type metamorphic terranes, typically exhibiting block-in-matrix fabric (e.g. Agard et al., 2016; Bebout and Penniston-Dorland, 2016). The matrix in these localities represents a hybrid composition, i.e. affected by extensive interaction with infiltrating fluids and or mixing of crustal and ultramafic components (Bebout and Penniston-Dorland, 2016).

In order to understand the complex interplay between these processes - deformation, metamorphism, mixing, devolatilization, preserved slab-mantle wedge interface localities now exhumed to the surface along ancient collision zones are typically utilized. Compilation of the information from known slab-mantle wedge interface localities, however, reveals that the geothermal gradient across the slab-mantle wedge interface also varies as subduction progresses (Fig. 2a–d; Agard et al., 2018). Along with the changing geothermal gradient and availability of fluids, the lithologies comprising the slab-mantle wedge interface and the processes acting on it therefore also varies.

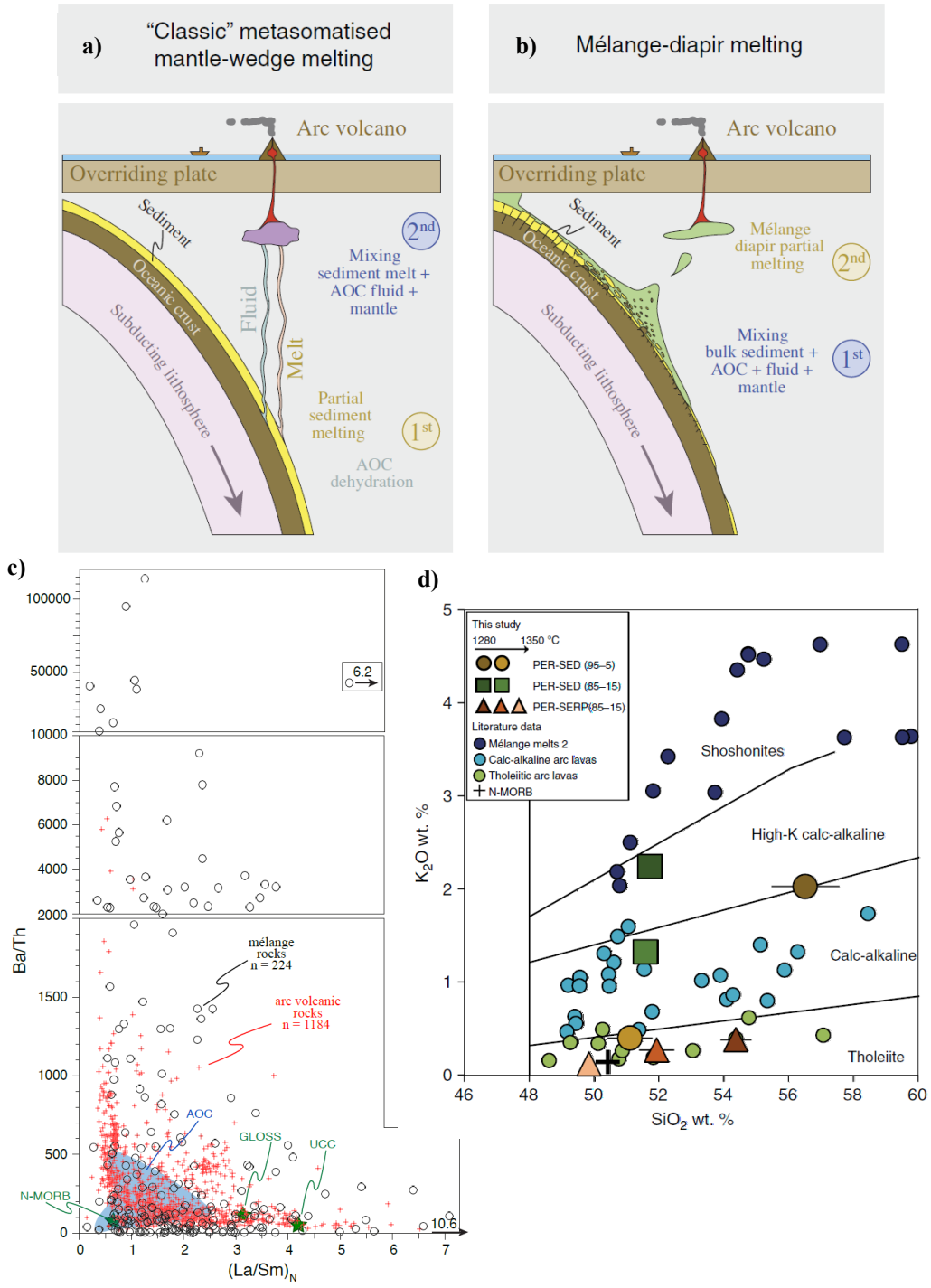

Fig. 1. a) Classic and b) Alternative models on the transfer of crustal components from the subducting slab to the overlying mantle. In the classic model, fluids and melts derived from the basalts and sediments are delivered as discrete pulses while in the alternative model, mixing of these components occurs first in the slab-mantle wedge interface (adopted from Nielsen and Marschall, 2017). c) Empirical geochemical data on arc volcanic rocks showing similar trace element signature of arc lavas and mélange rocks from Marschall and Schumacher (2012). d) Experimental analyses (Codillo et al., 2018) replicating typical arc magmatic series by mixing variable ratios of peridotite (PER) and mélange material (SED-sediment; SERP-serpentinite).

The warmest conditions (>20 °C/km) are generally observed at the start of subduction either due to subduction being initiated along spreading centers composed of young, warm oceanic lithosphere (van Hinsbergen et al., 2015) or due to upwelling of asthenospheric mantle during forearc rifting (e.g. Stern, 2004). Observations of metamorphic soles indicate that the slab-mantle wedge interface during this stage consist predominantly of coherent sheets of amphibolites and granulites. Deformation along the interface is also predominantly accommodated by shearing of the rheologically weaker sediments (e.g. Agard et al., 2016).

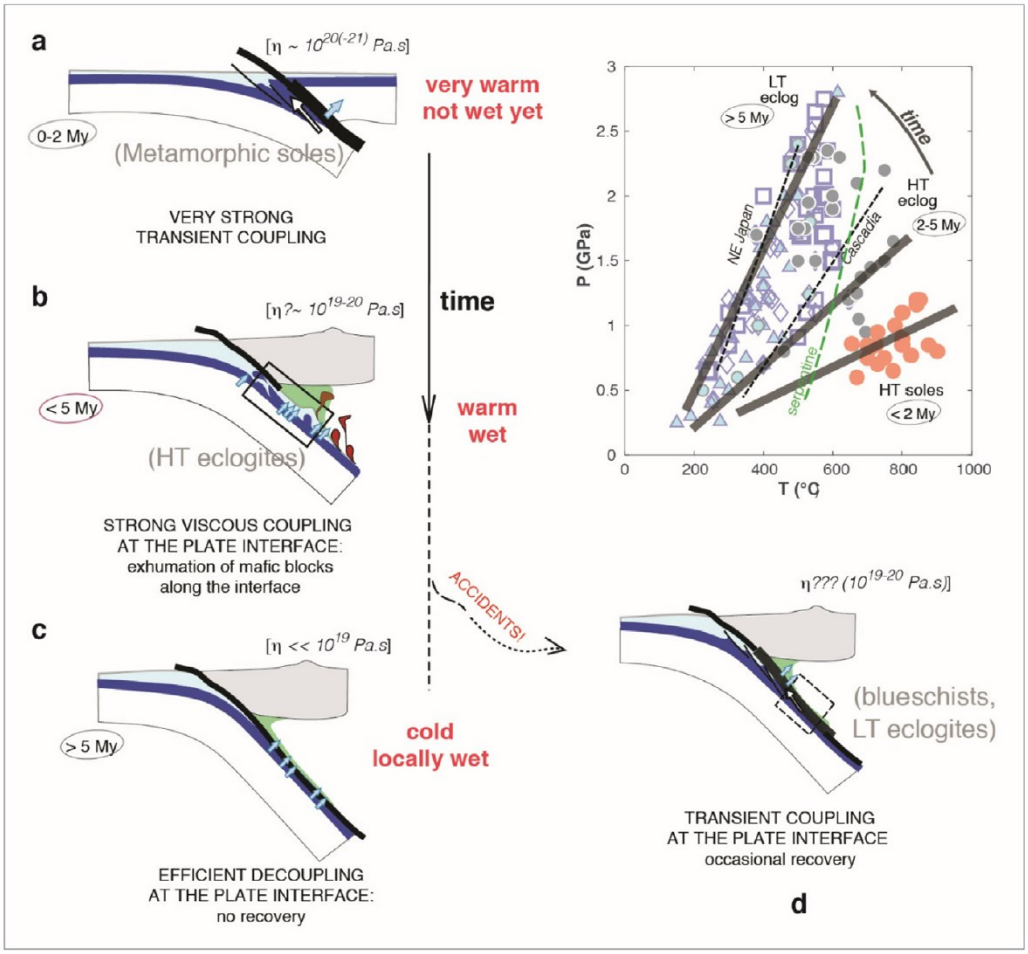

Fig. 2. a-d) Evolution of the slab-mantle wedge interface (referred to as plate interface in Agard et al., 2018) as subduction progresses. a) The earliest stage of subduction, 0-2 Myr since subduction initiation, are preserved in metamorphic soles while the interface in b) Incipient arcs (<5 Ma) are thought to be represented by high-*T* eclogites. c-d) The coldest geothermal gradients are observed in developed arcs (>5 Ma) dominated by blueschists and low-*T* eclogites.

In contrast to conditions during subduction inception, the coldest *P/T* gradients (~4–10 °C/km) are observed in developed subduction zones preserved in high-*P*/*T* type metamorphic terranes. These interface localities are composed of mélange localities with blocks surrounded by a matrix typically dominated by soft phyllosilicate minerals such as chlorite, talc, and serpentine (e.g. Bebout and Penniston-Dorland, 2016). Such complexes are composed predominantly of blocks metamorphosed at blueschists to low-*T* eclogite-facies conditions. Deformation and mass transfer by infiltrating fluids in these localities are channelized along the weaker matrix materials resulting to its hybrid composition (e.g. Bebout, 2013). Subduction complexes in transition from initiation are thought to be characterized by *P/T* gradients intermediate between the two extremes. Such localities composed of high-*T* eclogite and high-*P* amphibolite (e.g. Agard et al., 2018) are however less common. In theory studies of such localities can further provide unique insights on modern arcs with comparably high-*P/T* gradients.

In drawing a model of what comprises the slab-mantle wedge interface and the processes that occur along it therefore, the stage of subduction that the interface represents must also be considered. One such locality where the *P-T-D* history and petrological processes in the slab-mantle wedge interface can be evaluated is the Dalrymple Amphibolite associated with the Palawan Ophiolite in western Philippines. The Dalrymple Amphibolite is composed of high-grade metamorphic rocks and was originally thought to be a typical metamorphic sole (Encarnacion et al., 1995; Keenan et al., 2016) based on its limited occurrence, proximity to the Palawan Ophiolite, and its apparent inverted *P-T* gradient. The last basis was inferred from the apparent abundance of garnet amphibolites closer to the residual peridotites and the predominance of epidote amphibolites farther from the mantle section of the Palawan Ophiolite. This work however reveals key distinctions from a typical metamorphic sole. As will be discussed in more detail below, the Dalrymple Amphibolite exhibits a block-in-matrix configuration and do not preserve an inverted *P-T* gradient, i.e. different amphibolite blocks (garnet vs. epidote amphibolite) preserve comparable peak metamorphic conditions.

In Part 1 the pressure-temperature-deformation history of the Dalrymple Amphibolite is therefore first reevaluated. Advances on trace element geothermometry and elastic geobarometry are utilized

in this study along with conventional geothermobarometric techniques. The paleogeothermal gradient preserved in this fossil slab-mantle wedge interface is then used to constrain the specific stage of subduction that this block-in-matrix sequence likely represents. The latter half of this thesis, Part 2, investigates in detail the petrogenesis of the blocks comprising the Dalrymple Amphibolite and the processes that occurred along this slab-mantle wedge interface which controlled the chemistry of its matrix. Comparison of the whole-rock composition of the metamafic blocks with the mafic crust of the central Palawan Ophiolite reveals their genetic relationship and tectonic setting of formation. Application of a procedural workflow involving geostatistical (correlation coefficient), regression, and isocon analyses helped elucidate the effects of mixing and multiple fluid infiltrations in the evolution of whole-rock chemistry of the matrix of this mélange sequence. The petrological and geochemical characteristics of the matrix highlight mixing of crustal components along the slab-mantle wedge interface promoted by multiple deformation events and the ubiquity of fluids throughout its history. Observations from the Dalrymple Amphibolite are likely applicable to other subduction zone systems with similar geothermal gradients and provide clues on the nature of the slab-mantle wedge interface which ultimately affects arc magma chemistry.

References

Agard, P., Plunder, A., Angiboust, S., Bonnet, G., Ruh, J., 2018. The subduction plate interface: rock record and mechanical coupling (from long to short timescales). Lithos 320–321, 537–566.

Agard, P., Yamato, P., Soret, M., Pringent, C., Guillot, S., Plunder, A., Dubacq, B., Chauvet, A., Monie, P., 2016. Plate interface rheological switches during subduction infancy: Control on slab penetration and metamorphic sole formation. Earth and Planetary Science Letters 451, 208–220.

Bebout, G.E., 2013. Metasomatism in subduction zones of subduction zones of subducted oceanic slabs, mantle wedges, and the slab-mantle interface *In*: Harlov, D.E., Austrheim, H. Metasomatism (eds.) Metasomatism and the chemical transformation of rock. Lecture notes in Earth system sciences, Springer-Verlag Berlin Heidelberg, 289–349.

Bebout, G.E., Penniston-Dorland, S.C., 2016. Fluid and mass transfer at subduction interfaces-The field metamorphic record. Lithos 240–243, 228–258.

Codillo, E.A., Le Roux, V., Marschall, H.R., 2018. Arc-like magmas generated by melange-peridotite interaction in the mantle wedge. Nature Communications 9, 1–11.

Debari, S.M., Greene, A.R., 2011. Vertical stratification of composition, density and inferred magmatic processes in exposed arc crustal section. In: Brown, D., Ryan, P.D. (Eds.), Arc continent collision. Springer-Verlag, Berlin Heidelberg, 121–144.

Elliot, T., 2003. Tracers of the slab. *In*: Eiler, J. (Ed.). Inside the subduction factory. Geophysical Monograph 138. American Geophysical Union, Washington D.C. 23–45.

van Hinsbergen, D.J.J, Peters, K., Maffione, M., Spakman, W., Guilmette, C., Thieulot, C., Plümper, O., Gürer, D., Brouwer, F.M., Aldanmaz, E., Kaymackci, N., 2015. Dynamics of intraoceanic subduction initiation: 2. Suprasubduction zone ophiolite formation and metamorphic sole exhumation in context of absolute plate motions. Geochemistry, Geophysics, Geosystems 16, 1771–1785.

Kawamoto, T., Kanzaki, M., Mibe, K., Matsukage, K. N., Ono, S. 2012. Separation of supercritical slab-fluids to form aqueous fluid and melt components in subduction zone magmatism. Proceedings of the National Academy of Sciences of the United States of America 109, 18695–18700.

Marschall, H.R., Schumacher, J.C., 2012. Arc magmas sourced from melange diapirs in subduction zones. Nature Geoscience 5, 862–867.

Nielsen, S.G., Marschall, H.R., 2017. Geochemical evidence for mélange melting in global arcs. Science Advances 3:e1602402, 1–6.

Pearce, J.A., Cann, J.R., 1971. Ophiolite origin investigated by discriminant analysis using Ti, Zr, and Y. Earth and Planetary Science Letters 12, 339–349.

Schmidt, M.W., Poli, S., 2014. Devolatilization during subduction. *In*: Holland H.D., Turekian, K.K. (Eds), Treatise on Geochemistry, 2nd Edition. Elsevier Ltd, 669–701.

Stern, R.J., 2004. Subduction initiation: spontaneous and induced. Earth and Planetary Science Letters 226, 275–292.

Tatsumi, Y., 2005. The subduction factory: How it operates in the evolving Earth. GSA Today 15, 10:1130/1052-5173.

Part 1. The slab-mantle wedge of an incipient subduction zone: Insights from the *P-T-D* evolution and petrological characteristics of the Dalrymple Amphibolite, Palawan Ophiolite, Philippines

1.1 Introduction

The boundary between the subducting oceanic lithosphere and the mantle wedge, i.e. slab-mantle wedge interface (also termed subduction channel by Bebout, 2013 and plate interface by Agard et al., 2016, 2018), is a dynamically evolving component of intraoceanic subduction zones. Processes that occur in this interface are thought to control arc magma chemistry (Marschall and Schumacher, 2012; Codillo et al., 2018). Much of the information on the slab-mantle wedge interface beneath a mature arc comes from studies of high *P*/*T* type metamorphic terranes (e.g. Locatelli et al., 2019). These studies reveal chaotic mélange complexes that preserve paleogeothermal gradients of 4–10 °C/km (e.g. Guillot et al., 2009; Bebout and Penniston-Dorland, 2016). These complexes are composed of blocks derived from the underthrusting slab and the overlying serpentinized mantle surrounded by a highly sheared, fluid-rich matrix (e.g. Guillot et al., 2009; Bebout, 2013). This matrix represents the mixture of end-member lithologies (sediment, basalt/gabbro, and peridotite) in the slab-mantle wedge interface (e.g. Bebout and Barton, 2002; Marschall and Schumacher, 2012).

The slab-mantle wedge interface during the earliest stages of intraoceanic subduction on the other hand, is sometimes preserved as relatively intact sheets of metamorphic soles that underlie the mantle section of ophiolites. Ophiolites, which are fragments of fossil oceanic lithosphere, allow direct observation of the spatial, temporal and structural relationships of the different sections comprising an oceanic crust and mantle. Studies of metamorphic soles (e.g. Semail Ophiolite, Oman) reveal that these thin sheets of amphibolite- and granulite-facies grade metamorphic rocks preserve much higher geothermal gradients of >20 °C/km and are typically formed within the first 2 Myr of subduction inception (e.g. Soret et al., 2017; Agard et al., 2018).

Less information is however available on the petrological characteristics and metamorphic evolution of the slab-mantle wedge interface as it transitions from a young and hot subduction zone

to a mature arc with more hydrous minerals (e.g. chlorite and serpentine) stabilized at depth and marked by cold geothermal gradients (e.g. Guillot et al., 2009). A potential candidate for understanding relatively young island arcs is the Philippine island arc system which preserves a complex history of subduction, rifting, and arc-continent collision (e.g. Yumul et al., 2003). In its western margin, the collision between a nascent arc and the southward drifting North Palawan Continental Terrane (NPCT) led to the emplacement of the Palawan Ophiolite. The Dalrymple Amphibolite, a relatively well preserved high-grade metamorphic block-in-matrix complex, is located at the base of this ophiolite. Earlier works interpret these metamafic blocks as the slab-mantle wedge interface (i.e. metamorphic sole) of the Palawan Ophiolite (e.g. Encarnacion et al., 1995; Keenan et al., 2016).

In this contribution, detailed field characteristics of the metamafic blocks coupled with trace element geothermometry (i.e. Zr-in-rutile geothermometer) and elastic geobarometry (i.e. quartz-in-garnet Raman geobarometer) are used to constrain the pressure-temperature-deformation (*P-T-D*) history of the blocks and the matrix which comprise the Dalrymple Amphibolite. Additional constraints are obtained from conventional geothermobarometry, thermodynamic modelling and fluid inclusion microthermometry. Mineral abbreviations are after Whitney and Evans (2010) except for Ca-amphibole (Camp).

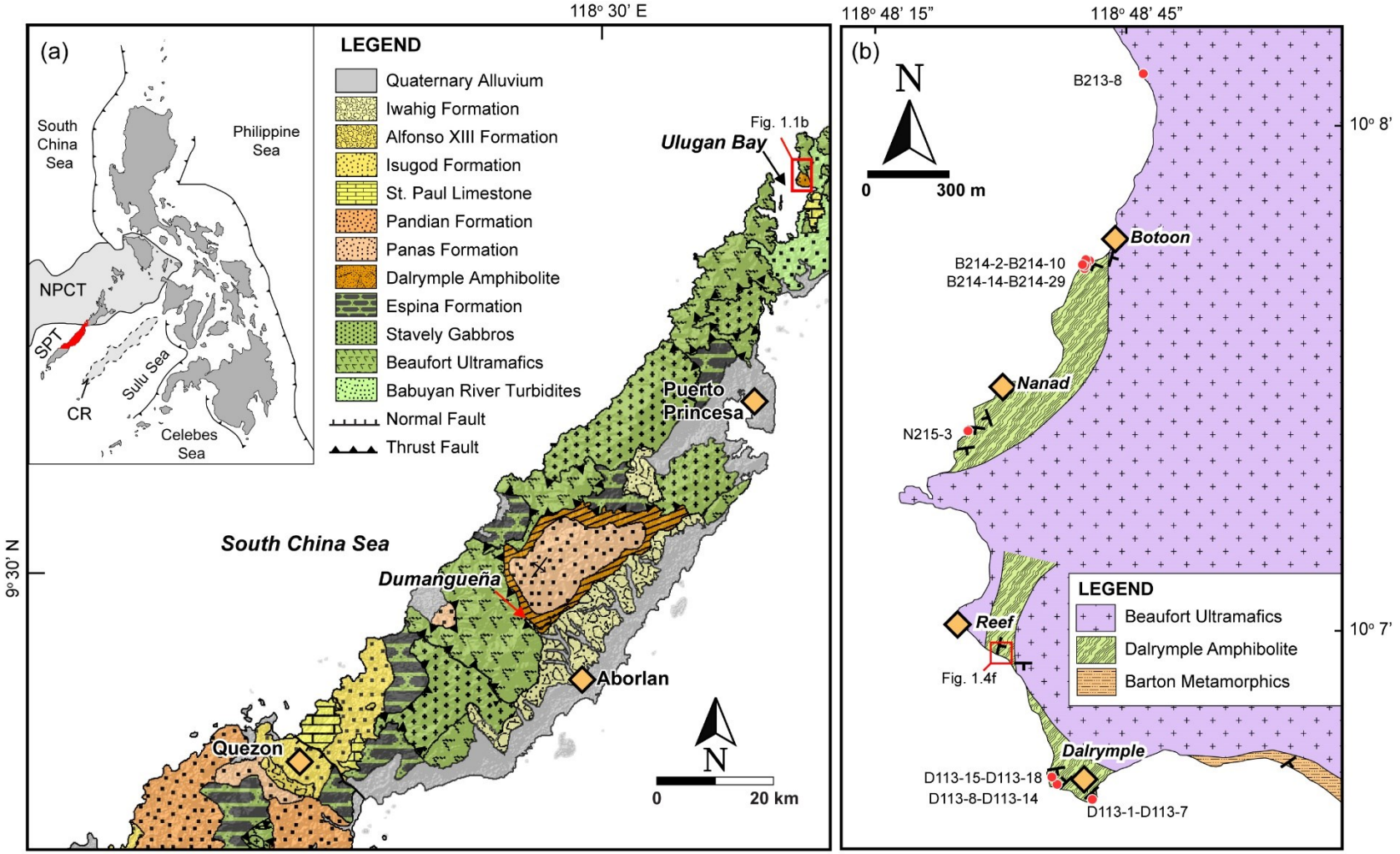

Fig. 1.1. a) Map showing the distribution of lithologies in central Palawan. The metamorphic sole is exposed in Ulugan Bay, Puerto Princesa and Dumangueña, Aborlan. Inset map shows tectonic map of the Philippines, the surrounding marginal basins and trenches. NPCT-North Palawan Continental Terrane, SPT-South Palawan Terrane, CR-Cagayan de Sulu Ridge. Modified from Labis et al. (2020); b) Distribution of Dalrymple Amphibolite and sampling points in Ulugan Bay modified from Encarnacion et al. (1995). The localities discussed in the text are marked as diamonds.

1.2 Geological Setting

Palawan island is located in western Philippines and forms part of the Palawan Microcontinental Block (PCB). It is divided into two terranes, the North Palawan Continental Terrane (NPCT) and the oceanic South Palawan Terrane (SPT, Fig. 1.1a). The NPCT was part of the Southeast Asian continental margin from Paleozoic through Mesozoic (Padrones et al., 2017; Cao et al., 2020). During the Eocene to Oligocene, rifting in the Southeast Asian margin resulted to the southward drift of the NPCT and ultimately led to the opening of the South China Sea marginal basin (Yumul et al., 2003; Keenan et al., 2016). The compression due to the southward drift of the NPCT was accommodated by subduction on its southeastern front forming a nascent arc. Some authors argue that the Cagayan de Sulu Ridge (CR in Fig. 1.1a) is the remnant of this nascent arc (Rangin and Silver, 1991). There is however, a significant difference in the proposed age of subduction initiation based on the igneous crystallization age of the ophiolite (~34 Ma; Encarnacion et al., 1995) and the cooling age of the metamorphic sole (~34 Ma; Keenan et al., 2016) compared to the age of arc magmatism in the CR (~18−16 Ma; Rangin and Silver, 1991). During the Late Oligocene to Early Miocene, the NPCT collided with this nascent arc and segments of the overlying plate were thrusted on top of the continent-derived turbidites as the Palawan Ophiolite (e.g. Keenan et al., 2016). Slivers of this fossil oceanic lithosphere crops out extensively in the central and southern segments of the island and is referred to as the South Palawan Terrane. Questions remain with regard to the presence of another Mesozoic ophiolite exposed in south Palawan and underthrusting the Eocene Palawan Ophiolite in central Palawan (e.g. Muller, 1991; Labis et al., 2020). This work focuses on the Eocene ophiolite exposed in central Palawan (e.g. Encarnacion et al., 1995; Keenan et al., 2016).

The Palawan Ophiolite represents a complete ophiolite sequence with basaltic pillow lava flows, isotropic and layered gabbroic and ultramafic cumulates comprising the crustal section and the residual mantle peridotites below (e.g. Dilek and Furnes, 2014). U-Pb geochronology of zircon separates from a plagiogranite associated with the ophiolite revealed the igneous crystallization age of the ophiolite to be 34.1 ± 0.1 Ma (Encarnacion et al., 1995). A thin block-in-matrix complex

composed of high-grade metamorphic rocks underlie the interlayers of mostly fresh to moderately serpentinized dunite and harzburgite in the localities of Botoon, Nanad and Dalrymple points (Fig. 1.1b). This unit is collectively referred to as the Dalrymple Amphibolite (Fig. 1.1b). Less extensive metamafic exposures also occur further south along Malatgao river in Dumangueña, Aborlan (Fig. 1.1a; Raschka et al., 1985). The Dalrymple Amphibolite, along with the other ophiolitic lithologies, are thrusted on top of deformed Eocene turbidites referred to either as Panas-Pandian Formation or the Barton Metamorphics (Fig. 1.1a; Aurelio et al., 2014).

Earlier studies on the Dalrymple Amphibolite exposed in Ulugan Bay in central Palawan, estimated the peak *P-T* conditions of its formation at 700–760 °C at a minimum pressure of 9 kbar using conventional geothermobarometry, i.e. Grt-Camp-Pl-Qz geobarometer and Grt-Bt and Grt-Camp geothermometers (cf. Encarnacion et al., 1995). $^{40}Ar/^{39}Ar$ ages of 34.2 ± 0.5 Ma, 34.2 ± 0.6 Ma and 34.3 ± 0.3 Ma were obtained from two amphibole samples in metamafic blocks and one muscovite from kyanite-chlorite-muscovite schists, respectively (Encarnacion et al., 1995; Keenan et al., 2016). These were interpreted as metamorphic cooling age of the Dalrymple Amphibolite (Encarnacion et al., 1995). Chemical Abrasion Thermal Ionization Mass spectrometry (CA-TIMS) U-Pb dating of oscillatory-zoned zircons from competent pods in the Dalrymple Amphibolite yielded weighted mean ages of 35.242 ± 0.062 Ma, 35.862 ± 0.048 Ma and 35.25 ± 0.15 Ma (Keenan et al., 2016). This was interpreted as the igneous crystallization age of the mafic protolith of the metamafic blocks.

1.3 Field Occurrence

The Dalrymple Amphibolite occurs as a mélange complex with blocks surrounded by a highly sheared matrix in contrast to the relatively coherent sheets that characterize most metamorphic soles (Agard et al., 2016; 2020). Earlier works, based on kinked quartz and kyanite in the metamafic blocks, attributed the mélange-like appearance to a later, ‘cold’ deformation event that transformed a more coherent metamafic and schist unit (Encarnacion et al., 1995). Several stages of deformation are however possible in these shear zones as described below.

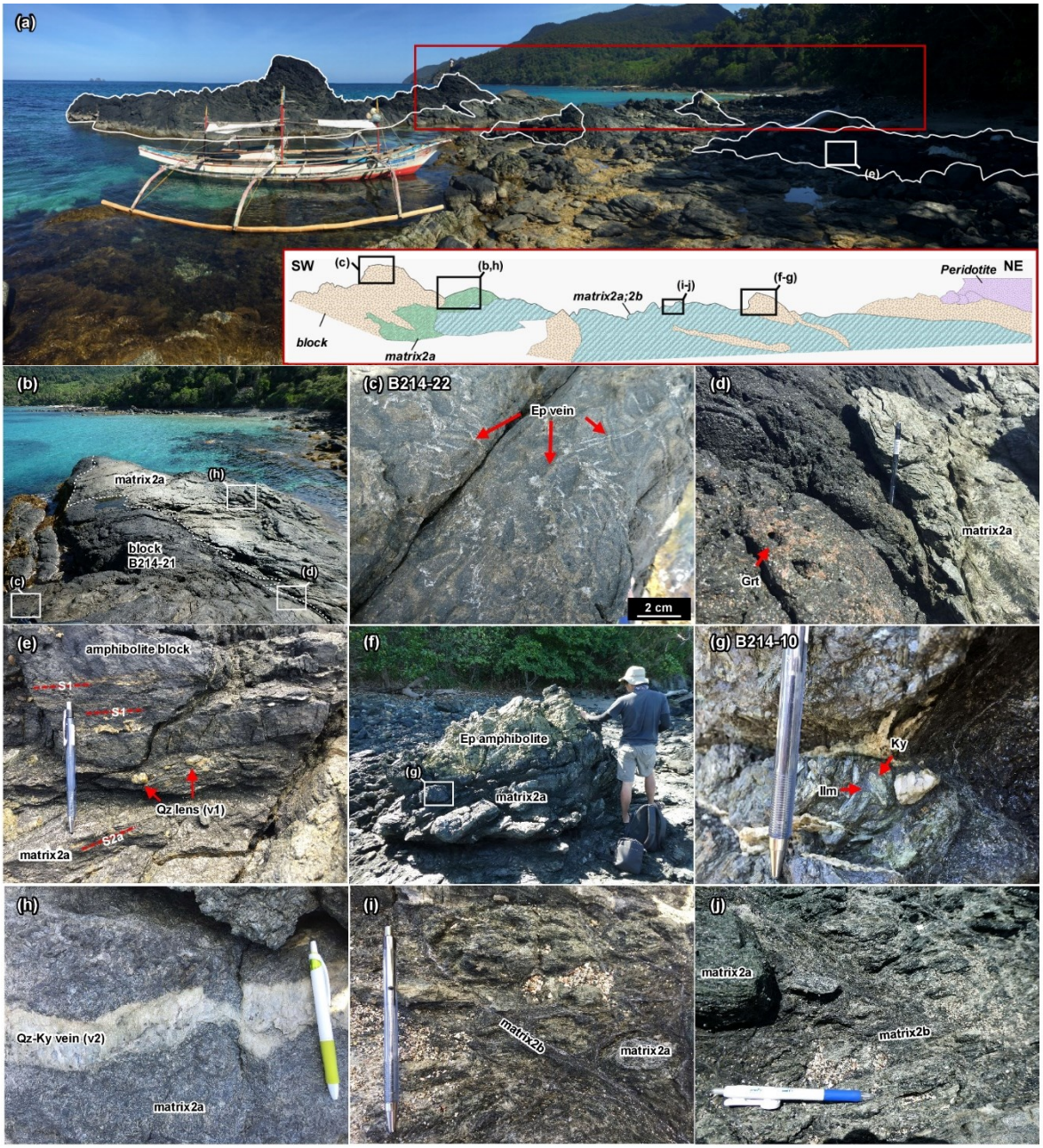

Fig. 1.2. Field photos of the exposure in Botoon point. a) Panoramic photo of the block and matrix sequence. Inset shows a schematic representation of the area enclosed in red box showing the blocks (white solid lines) and the matrix in the low lying portions of the exposure. b–d) Melanocratic metamafic block surrounded by lighter matrix2a and cut by epidote veins. e) Foliation (S1) parallel quartz lenses. f) Matrix2a below the Ep amphibolite block which shows g) Coarse kyanite crystals surrounded by ilmenite. h) Qz-Ky veins in the surrounding matrix2a. i,j) Matrix2a transected by later matrix2b.

In Botoon point (10.1353°N 118.8133°E; Fig. 1.1b), the Dalrymple Amphibolite consists of tabular, angular to subrounded blocks up to 15 m in length (Fig. 1.2a, b). Most blocks are metamafic, with variable amounts of garnet and epidote. Randomly-oriented epidote-veins are locally developed in an amphibolite block but do not continue to the surrounding matrix (Fig. 1.2c, d). Minor metasedimentary blocks are also observed, including metacherts (i.e. Camp-Czo quartzites) and metacarbonates replaced by Ep amphibolite. The foliation in some blocks is marked by the arrangement of elongate minerals (e.g. amphibole) or the interlayers of quartz-rich and mafic domains dipping gently (~30°) to the SE. The foliation in the blocks is denoted as S1 (e.g. Fig. 1.2e).

The blocks in Botoon are surrounded by a sheared matrix material occupying the low-lying portions of the exposure (Fig. 1.2a–d). Two generations of matrix formation defined by the same assemblage (Ky+Camp+Bt+Grt+Ilm) but distinguished by cross-cutting pervasive foliation directions are observed (matrix 2a and 2b in Fig. 1.2). In some parts of the exposure, the foliation of the earlier matrix 2a denoted as S2a (e.g. Fig. 1.2e) are generally subparallel to those of the blocks. Elongate minerals such as kyanite and Ca-amphibole exhibit foliation S2a and a WNW-ESE mineral lineation is observed locally in the kyanite and quartz. In other parts of the exposure, coarse kyanite grains are surrounded by accumulations of ilmenite (Fig. 1.2f, g). Quartz and Qz-Ky-rich domains occur as deformed lenses (Fig. 1.2e) arranged subparallel to the foliation of the matrix2a (S2a) and as veins cross-cutting the matrix (Fig. 1.2h) and the blocks. In some parts of the exposure, the matrix2a is cut by a subsequent melanocratic matrix2b which transformed the earlier formed matrix2a into small autochthonous blocks (Fig. 1.2i, j). The matrix2b in Botoon have the same mineralogy as the earlier matrix2a but elongate minerals (e.g. Ca-amphibole and kyanite) exhibit distinct foliation, denoted as S2b.

Some of the blocks (e.g. metacarbonates) in Botoon are surrounded by rinds (Ep amphibolite) with concentric foliation and separating the blocks from the matrix. In other blocks, a distinct rind is not observed but progressive changes in mineralogy (e.g. increasing garnet in some metamafic blocks) can be noted towards the contact with the matrix (Fig. 1.2d). The overlying interlayers of dunite and harzburgite are exposed in the NE side of the exposure.

The contact between the Dalrymple Amphibolite and the mantle section of the ophiolite is best exposed in Nanad (Figs. 1.1b, 1.3a). Shear-sense indicators suggest a top-to-the-NW sense of movement (Fig. 1.3b). Shearing is also more pervasive in Nanad than Botoon. The blocks in Nanad are smaller and have rounded to subrounded corners compared to those in Botoon (Fig. 1.3c). The matrix2a with Ky+Camp+Bt+Grt assemblage in Botoon is also found as randomly-oriented blocks in this locality (Fig. 1.3d–e). Amphibolite cut by Qz-Ky veins, also observed in Botoon, occur as blocks in Nanad. These veins abruptly end and do not continue towards the surrounding matrix2b (Fig. 1.3f, g). In Botoon matrix2b occurs locally, cross-cutting the predominant matrix2a. In Nanad, matrix2b is the dominant matrix type. This matrix2b (Grt+Ky+Camp+Bt+Qz) surrounds metamafic and matrix2a blocks as well as garnet (0.5–5 mm), peapod-shaped Ca-amphibole (0.5–7 mm) and altered kyanite porphyroclasts. Local S-C fabrics are also exhibited by matrix2b in Nanad.

The metamorphic rocks are most extensively exposed in Dalrymple point (Figs. 1.1b, 1.4a). The exposure can be divided to a block-dominated zone in the northwest which occurs proximal to dunite-harzburgite interlayers and a more homogenous amphibolite zone to the southeast (cf. Encarnacion et al., 1995; Keenan et al., 2016). The NW zone consists of interlayered blocks of garnet amphibolites (Fig. 1.4b, c), metachert quartzite (Fig. 1.4d) and biotite schists (Fig. 1.4e) with schistosity dipping moderately (53°) towards the SE. In the northwestern section of the exposure, a resistant quartzite block sits on top of the surrounding Camp-Ky-dominated matrix2a similar to the exposure in Botoon (Fig. 1.4f). The schistosity of the matrix2a dips gently towards the SE while stretching lineation on S2a (L2 in Fig. 1.4g) defined by hornblende is N-S. Kyanite crystals are also more extensively replaced by pseudomorphic muscovite compared to other localities (Fig. 1.4g–h).

Further southeast of the block-dominated zone is a more homogenous, foliated and folded amphibolite, Ep amphibolite sequence (Fig. 1.4a). The Ep amphibolites are highly sheared (i.e. fine to very fine grained; 0.10–0.25 mm) and generally dip gently towards the SE (Fig. 1.4i–k). Epidote-rich domains appear as subparallel veins rather than distinct, continuous layers (Fig. 1.4j, k). The amphibolites commonly occur as elongated pods surrounded by Ep amphibolite and are coarse-

grained (Fig. 1.4l). The sequence is crosscut by quartz veins that are subparallel and in places crosscut the S1 foliation of the Ep amphibolites (Fig. 1.4j, k). Encarnacion et al. (1995) interpreted the prevalence of Ep amphibolites farther away from the metamorphic-ultramafic contact to signify decreasing metamorphic grade southward although peak *P-T* estimates for the Ep amphibolites are lacking.

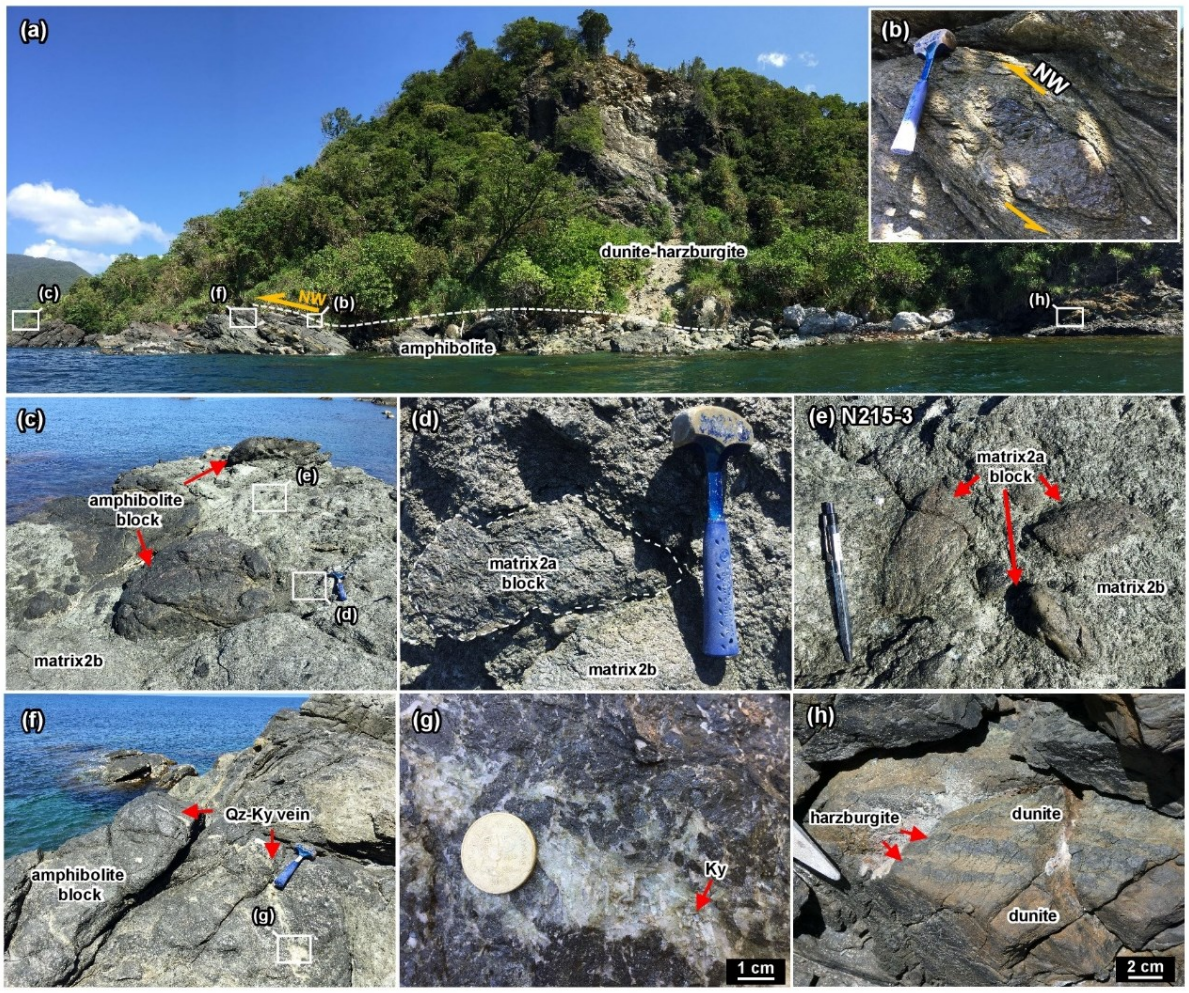

Fig. 1.3. Field photos of the exposure in Nanad. a) Panoramic photo showing the thrust boundary between the metamorphic sole and the overlying peridotites. b) Shear sense indicator suggests a top to NW movement. c) Rounded metamafic blocks surrounded by the lighter-colored and highly sheared matrix2b. d–e) Matrix2a lenses transformed into small rounded blocks. f, g) Metamafic block transected by Qz-Ky vein which terminates in the surrounding matrix2b. h) Dunite-harzburgite interlayers which comprise the hanging wall in Nanad.

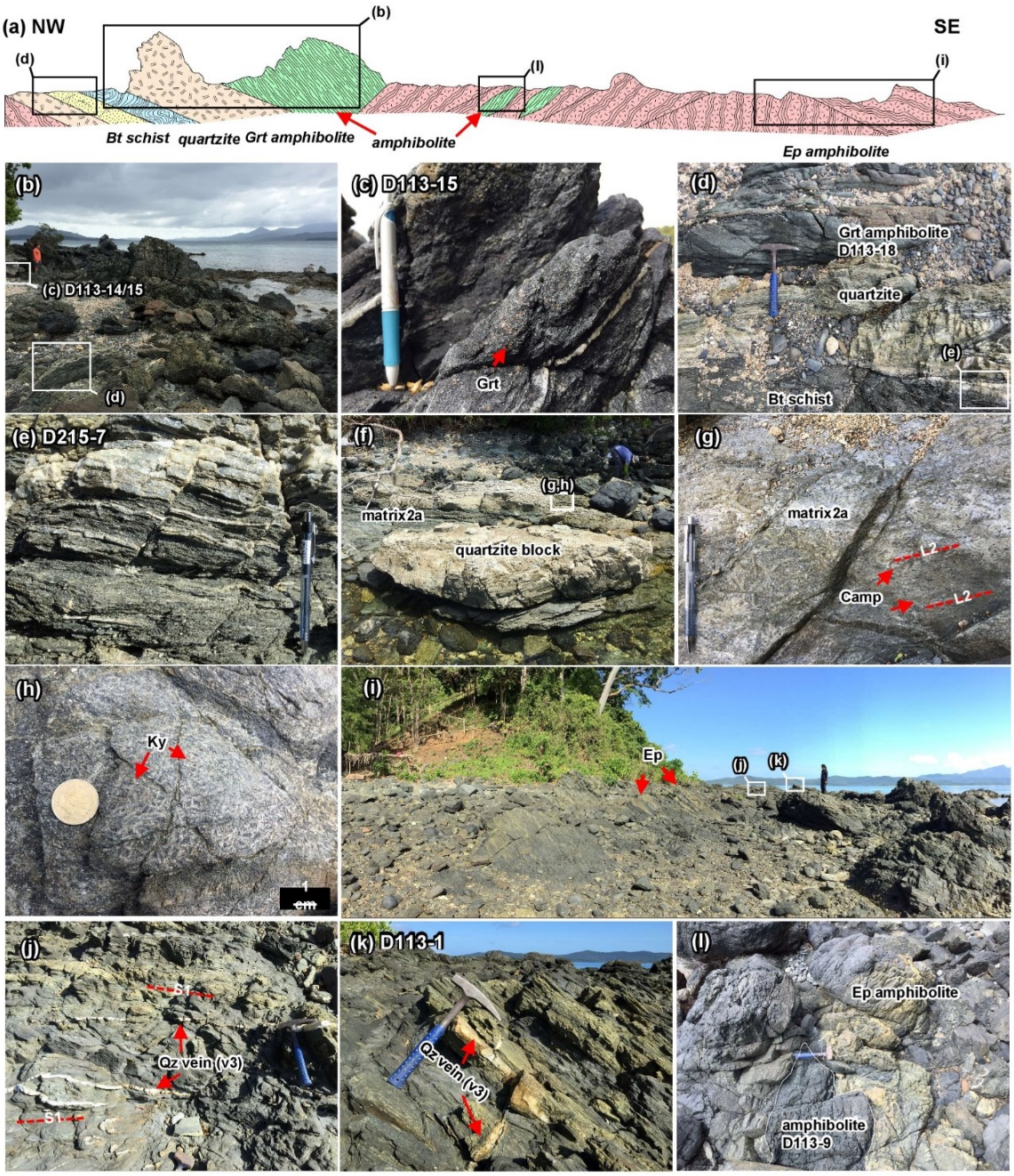

Fig. 1.4. Field photos in Dalrymple point. a) Schematic representation of the exposure showing the block-dominated NW section and the more coherent Ep amphibolite sequence in the SE side. The boxes indicate the relative position of the field photos. b–e) Interlayers of Grt amphibolite, quartzite and Bt schist blocks. f) Quartzite block surrounded by matrix2a. g–h) Kyanite pseudomorphed by muscovite, and Ca-amphibole in matrix2a. i) Relatively coherent Ep amphibolite block cut by later stage j–k) Quartz veins (v3) which transect the foliation of the blocks (S1). In Fig. 1.4 j, k, epidote-rich domains are the yellowish portions while the darker parts are the epidote-poor domains. l) Amphibolite lens surrounded by Ep amphibolite.

Table 1.1 Summary of samples used in Part 1

Sample No.	Locality			Field occurrence	Lithology	Major mineral assemblage [+secondary]	Accessory minerals	EPMA analysis	Notes
	Area	Latitude (N)	Longitude (E)						
B213-8	Botoon	10°8'7.1"	118°48'47.7"	Block	Grt amphibolite	Camp + Grt + Qz + Ep [+Chl +Ep]	Rt + Ilm + Zrn + Ap + Ky	○	
B214-2G	Botoon	10°7'44.2"	118°48'40.2"	Matrix2a	Grt amphibolite	Camp + Grt + Ky + St + Bt [+Chl]	Rt + Ilm + Zrn + Ap + Chl	○	
B214-5	Botoon	10°7'44.8"	118°48'40.6"	Qz-Ky lens in Matrix2a	Ky-Camp-Bt schist	Camp + Ky + St + Bt [+Chl +Ms]	Ilm	○	Stage 3 *P-T* estimation
B214-6	Botoon	10°7'44.8"	118°48'40.4"	Matrix2a	Ky-Grt-Bt schist	Grt + Ky + Ilm + Bt [+Chl +Ms]	Ap	○	
B214-8	Botoon	10°7'44.4"	118°48'40.6"	Matrix2a and 2b	Ky-Camp-Bt schist	Matrix2a: Camp + Oam + Grt + Ilm + Ky + Chl + Bt [+Chl] Matrix2b: Camp + Oam + Ilm + Ky+ Bt [+Ms +Chl]	Both 2a and 2b: Ap	○	
B214-9	Botoon	10°7'44.4"	118°48'40.6"	Matrix2a	Ky-Grt-Bt schist	Grt + Ky + Ilm + Bt [+Ms +Chl]	Ap	○	
B214-10	Botoon	10°7'44.7"	118°48'41"	Matrix2a	Ky-Camp-Bt schist	Camp + Grt + Ky + Ilm + Bt [+Ms +Chl]	Mag + Ap + Tur	○	Pseudosection
B214-14	Botoon	10°7'45.8"	118°48'41"	Matrix2a	Ky-Ep-Grt schist	Ky + Grt + Ep + Ilm + Bt [+Ms +Ep +Chl]	Rt + Ap + Zrn + Chl	○	Geothermobarometry
B214-21	Botoon	10°7'45.0"	118°48'40.1"	Block	Grt amphibolite	Camp + Grt + Ep + Qz [+Act +Ep +Chl]	Ky + Bt + Ap + Rt + Ilm + Zrn	○	Geothermobarometry cut by Qz-Ky vein
B214-29	Botoon	10°7'44.6"	118°48'40.8"	Matrix2a and 2b	Ky-Hbl schist	Matrix2a: Camp + Oam + Qz + Ky + Chl [+Chl +Ms] Matrix2b: Camp + Oam + Qz +Ky [+Ms]	Both 2a and 2b: Ilm	○	
N215-3	Nanad	10°7'24.3"	118°48'26.1"	Matrix2a and 2b	Grt-Hbl-Bt schist	Matrix2a and 2b: Camp + Grt + Ky + Bt + Qz [+Ms +Chl]	Ilm + Rt + Zrn + Ap	○	

Table 1.1 continued

Sample No.	Locality			Field occurrence	Lithology	Major mineral assemblage [+secondary]	Accessory minerals	EPMA analysis	Notes
	Area	Latitude (N)	Longitude (E)						
D113-1	Dalrymple	10°6'39.4"	118°48'41.1"	Block	Ep amphibolite	Camp + Ep + Pl + Qz [+Act +Chl +Ab]	Ttn + Ap	○	cut by Qz vein
D113-2	Dalrymple	10°6'39.4"	118°48'41.1"	Block	Ep amphibolite	Camp + Ep + Pl (An_{8-14}) + Qz [+Act +Ab]	Rt + Zrn + Ttn + Ap + Bt	○	Geothermobarometry
D113-5	Dalrymple	10°6'39.4"	118°48'41.1"	Block	Ep amphibolite	Camp + Ep + Pl (An_{1-14})+ Qz [+Act +Ab]	Rt + Zrn + Ttn + Ap + Bt	○	
D113-8	Dalrymple	10°6'41.6"	118°48'36.7"	Block	Ep amphibolite	Camp + Ep + Pl (An_{16-27}) + Qz [+Act +Ab]	Rt + Zrn + Ttn + Ap + Bt	○	
D113-9	Dalrymple	10°6'41.6"	118°48'36.7"	Block	Amphibolite	Camp + Ep + Pl (An_{8-17}) + Qz [+Act +Chl +Ab]	Rt + Zrn + Ttn	○	Geothermobarometry
D113-10	Dalrymple	10°6'41.6"	118°48'36.7"	Block	Ep amphibolite	Camp + Ep + Pl (An_{1-14}) + Qz [+Chl +Ab]	Rt + Zrn + Ttn + Ap + Bt	○	
D113-11	Dalrymple	10°6'41.6"	118°48'36.7"	Block	Amphibolite	Camp + Ep + Pl (An_{1-11}) + Qz [+Act +Ab]	Rt + Zrn	○	
D113-14	Dalrymple	10°6'42.5"	118°48'36.1"	Block	Grt amphibolite	Camp + Grt + Pl (An_{7-16}) + Qz + Ep [+Act +Chl +Ep]	Rt + Zrn + Ap + Ms	○	Geothermobarometry
D113-15	Dalrymple	10°6'42.5"	118°48'36.1"	Block	Grt amphibolite	Camp + Grt + Pl (An_{15-24}) + Qz + Ep [+Chl +Ep +Ab]	Rt + Ap + Ms + Ccp + Py	○	
D113-18	Dalrymple	10°6'43.3"	118°48'36.3"	Block	Grt amphibolite	Camp + Grt + Pl (An_{8-18}) + Qz + Ep + Bt [+Act +Chl +Ep +Ab]	Rt + Zrn + Ap	○	Geothermobarometry
D215-7	Dalrymple	10°6'43.3"	118°48'36.3"	Block	Ep-Bt-Ms schist	Bt + Ms + Pl + Ep +Qz [+Chl]	Rt + Ilm + Zrn + Ap	○	

Table 1.2. Summary of the mineral paragenesis, their representative mineral chemistry and the deformation (D) and veining (V) stages of the Dalrymple Amphibolite.

Phase	Block (Stage 1)*		Matrix (Stage 2)		Retrograde (Stage 3)
	Stage 1a	Stage 1b	Matrix 2a	Matrix 2b	
	D1 / V1	D1 / V1	D2a / V2	D2b / V2	D3 / V3
Grt	$Alm_{46-51}Prp_{10-19}Grs_{15-20}Sps_{15-25}$	$Alm_{38-41}Prp_{30-35}Grs_{13-15}Sps_{13-17}$	$Alm_{35-36}Prp_{28-32}Grs_{16-19}Sps_{16-19}$		
Amp		Camp1b: Mg# = 0.64-0.80	Oam2a/Camp2a: Mg# = 0.72-0.76	Oam2b/Camp2b: Mg# = 0.72-0.74	Act3: Mg# = 0.45-0.83
Ep	Czo1a: Ps_{20-29}		Czo2a:Ps_{18-29} / Aln2a		Czo3: Ps_{30-39}
Pl		**An_{10-18}			An_{0-10}
Bt			Mg# = 0.80-0.86	Mg# = 0.75-0.81	
Rt	Nb = 175-266 ppm; Zr = 170-466 ppm	Nb = 720-5606 ppm; Zr = 222-562 ppm	Nb = 748-1782 ppm; Zr = 281-533 ppm		
Qz					
Ap					
Ilm					
Ky			Cr_2O_3 = 0.71-2.17 wt.%	Cr_2O_3 = 0.01-0.67 wt.%	
Chl			Mg# = 0.83-0.84		Mg# = 0.38-0.53
Ms					Si = 3.71-3.95 a.p.f.u.
Mag					
St					
Tur					

▬ - abundant —— - accessory mineral ----- - minor minerals with special occurrence (see text for details)

*Mineral paragenesis of the Grt amphibolite block B214-21 used for geothermobarometry

**Pl1b is absent in Grt amphibolite block B214-21 but occurs in other Dalrymple Point blocks; Mineral chemistry data from D113-18

The information on samples used in this study are summarized in Table 1.1 while the deformation stages (D1–D3), veining stages (V1–V3), mineral paragenesis and mineral occurrence based on the field characteristics of the Dalrymple Amphibolite are summarized in Table 1.2. The timing of matrix formation which surround the blocks relative to the *P-T-D* history of the blocks cannot be constrained solely on field characteristics. In the metamorphic sole of the Semail (Oman) Ophiolite for example, shearing which isolated and emplaced high-grade metamafic blocks against lower *P-T* metamorphic rocks, occurred late in its *P-T-D* history (e.g. Soret et al., 2017). In the Catalina schists on the other hand, petrological and field characteristics reveal that matrix formation started early at lower grades and the mélange sequence as a whole was subsequently exposed to higher *P-T* conditions along the subduction channel (e.g. Penniston-Dorland et al., 2014; 2018). In the case of the Dalrymple Amphibolite, constraining the *P-T-D* history of the blocks and the surrounding matrix is needed to elucidate the origin of the block-in-matrix sequence as a whole.

The information for the metamafic and metasedimentary blocks are therefore recorded as Stage 1 while those of the matrix are regarded as Stage 2 in Table 2. In the exposures in Botoon and northwest Dalrymple, the first stage of deformation (D1) is preserved as foliation (S1) in the blocks. Deformation events related to the formation of schistosity (S2a) and stretching lineation (L2) in matrix2a is marked as D2a. In Botoon, the start of a subsequent deformation event (D2b) is hinted by the formation of matrix2b which crosscuts the matrix2a (Fig. 1.2i, j) and follows a distinct foliation direction (S2b). The exposure in Nanad exhibits a more pervasive D2b deformation. Matrix2a occurs exclusively as rounded blocks (Fig. 1.3d, e) along with the blocks of other rock types which preserve the earliest stage (Stage 1, D1). The surrounding matrix2b is finer-grained (~0.05 mm) than matrix2a, highly foliated (S2b) and locally preserves S-C fabric (S2b and C2b).

Lastly, coarser Stage 1 and Stage 2 minerals comprising both the blocks and the matrix respectively, are partially to completely replaced by finer hydrous minerals in most samples, e.g. kyanite to muscovite and ferromagnesian minerals to chlorite, epidote and actinolite. These replacement minerals also occur as veins which cut through the foliation of the blocks and both

matrix2a and 2b. This indicates a final retrograde stage (Stage 3) where the planar veins associated with Stage 3 indicate a late stage deformation event (D3) during Stage 3.

1.4 Analytical methods

All of the analyses in this study except whole-rock geochemical analysis were done at Department of Geology and Mineralogy, Kyoto University. Quantitative analysis of rock-forming minerals and X-ray elemental mapping of thin section samples were conducted using a JEOL JXA-8105 electron probe microanalyzer. Analytical conditions for quantitative analyses were 15.0 kV acceleration voltage, 10 nA beam current, and 3 μm beam diameter. The counting time for the peak and backgrounds were 30 s and 15 s for Cl, 60 s and 30 s for F, and 10 s and 5 s for other elements. Natural and synthetic minerals were used as standards and ZAF correction was applied. Representative mineral analyses are given in Tables 1.3 and 1.4. Estimation of Fe^{3+} in garnet and Ca-amphibole followed Droop (1987) and Schumacher (1991). Analytical conditions for the Zr-in-rutile geothermometry followed that of Zack et al. (2004). Acceleration voltage used was 20.0 kV, 120 nA probe current and a probe diameter of 5 μm to determine both major and trace element concentration of the rutile grains. Elemental mapping was conducted using an acceleration voltage of 15.0 kV, probe current of 60 nA, with either a focused beam or a beam diameter of 3–5 μm. Panchromatic cathodoluminescence (CL) mapping of quartz for Stage 3 was performed at 15.0 kV, 1 nA.

Elastic geobarometry utilizing shifts in the Raman bands of quartz inclusions in garnet host was employed by determining remnant inclusion pressures (P_{inc}). The Raman shifts were obtained using a laser Raman spectroscopy (JASCO NRS 3100). P_{inc} can be calculated using room temperature (20 ±1 °C) measurements of the shift from the 128, 206, and 464 cm^{-1} Raman bands of quartz inclusions ($\Delta\nu_{128}$, $\Delta\nu_{206}$, and $\Delta\nu_{464}$ respectively) and a hydrostatic pressure calibration (Schmidt and Ziemann, 2000; Thomas and Spear, 2018). Spectral interference from the 170–215 cm^{-1} Raman bands of the garnet host can however result in linewidth broadening of the 206 cm^{-1} band while the 128 cm^{-1} band is relatively weak and is not observed in some inclusions (e.g. Thomas and Spear, 2018). The shift of the 464 cm^{-1} band ($\Delta\nu_{464}$) was therefore used to calculate the entrapment isomeke consistent with the method employed in other related studies (e.g. Thomas and

Spear 2018). The isomeke represents the *P-T* curve along which fractional volume changes of the host and inclusion are the same and whose instantaneous slope is determined by the ratio of the difference in volume thermal expansion coefficients and compressibility of quartz and garnet (e.g. Angel et al., 2017a, b). The entrapment isomeke was calculated using the freeware EoSFit-Pinc module (e.g. Angel et al., 2017a) applying the equation of state parameters for the curved α-β quartz phase boundary of Angel et al. (2017b) and the Tait equation of state and parameters for garnet from Holland and Powell (2011).

Fluid inclusion assemblages associated with Stage 3, were identified by petrography and CL-imaging. Microthermometry was performed using a LINKAM, LK-600 heating and cooling stage. The calibration was performed on synthetic fluid inclusion standards, 10 wt% NaCl solution and pure water. Final ice-melting temperature and total homogenization temperature of the two-phase aqueous fluid inclusions were determined by heating and cooling the fluid inclusions respectively at a rate of 1 °C min^{-1} close to the final temperature. Precision of the microthermometric measurements are ±0.1 °C for melting and homogenization temperatures. During our heating experiments, no decrepitation was observed.

Representative matrix sample B214-10 used for thermodynamic modelling was powdered in a tungsten-carbide mill at Kyoto University and whole-rock geochemical analysis was performed at Bureau Veritas, Perth, Australia. Major-element concentrations were obtained by fused glass bead X-Ray fluorescence (XRF) analysis. Analytical precision based on replicate sample is within 1 % for all elements.

Table 1.3 Representative analyses of rock-forming minerals in the blocks

Sample No. (Area)	B214-21 (Botoon)				D113-15 (Dalrymple)				
Lithology	Grt amphibolite				Grt amphibolite				
Mineral	Grt1		Hbl1		Grt1	Hbl1	Pl1	Ms1	Ep1
Occurrence	Matrix	Matrix	Matrix	Matrix	Matrix	Matrix	Matrix	Matrix	Matrix
Core/Mantle/Rim	Core	Rim	Core	Rim	Rim	Rim	Rim		
SiO_2	38.27	38.95	43.46	43.92	38.87	43.02	64.20	47.78	38.36
TiO_2	0.16	0.10	0.52	0.96	0.20	0.33	0.04	0.58	b.d.
Al_2O_3	20.94	21.60	15.13	14.94	21.31	14.80	22.83	30.94	23.62
Cr_2O_3	b.d.	0.03	0.02	0.04	0.02	b.d.	b.d.	b.d.	b.d.
FeO	22.46	19.55	12.03	11.11	26.74	17.47	b.d.	3.29	
Fe_2O_3									12.691
MnO	8.99	7.27	0.60	0.62	3.38	0.22	b.d.	0.04	0.10
MgO	3.17	7.71	12.22	12.44	4.28	8.82	b.d.	1.35	b.d.
CaO	6.53	5.07	10.57	10.92	6.84	10.34	4.36	0.03	23.72
BaO	n.d.	n.d.	0.01	0.09	0.04	0.02	0.04	0.24	b.d.
Na_2O	b.d.	0.07	1.80	1.71	0.06	2.69	9.06	1.33	b.d.
K_2O	0.02	b.d.	0.48	0.46	0.02	0.45	0.08	9.51	b.d.
F	n.d.	n.d.	0.09	0.08	b.d.	0.07	n.d.	b.d.	b.d.
Cl	n.d.	n.d.	b.d.	b.d.	b.d.	b.d.	n.d.	b.d.	b.d.
-O≡F			0.04	0.03		0.03			
-O≡Cl									
Total	100.53	100.36	96.92	97.30	101.75	98.21	100.62	95.10	98.49
Number of O	12	12	23	23	12	23	8	11	12.5
Si	3.02	3.00	6.32	6.37	3.01	6.39	2.82	3.22	3.03
Ti	0.01	0.01	0.06	0.10	0.01	0.04	<0.01	0.03	b.d.
Al	1.95	1.96	2.60	2.55	1.95	2.59	1.18	2.45	2.20
Cr	b.d.	<0.01	<0.01	<0.01	<0.01	<0.01	b.d.	b.d.	b.d.
Fe^{2+}	1.48	1.22	1.46	1.35	1.73	2.10	b.d.	0.19	
Fe^{3+}	<0.01	0.04	0.41	0.24	<0.01	0.07			0.75
Mn	0.60	0.47	0.07	0.08	0.22	0.03	b.d.	<0.01	0.01
Mg	0.37	0.89	2.65	2.69	0.49	1.95	b.d.	0.14	b.d.
Ca	0.55	0.42	1.65	1.70	0.57	1.65	0.21	<0.01	2.01
Ba			<0.01	<0.01	<0.01	<0.01	<0.01	0.01	b.d.
Na	b.d.	0.01	0.51	0.48	<0.01	0.77	0.77	0.17	b.d.
K	<0.01	b.d.	0.09	0.09	<0.01	0.09	<0.01	0.82	b.d.
F			0.04	0.04	b.d.	0.03		b.d.	b.d.
Cl			b.d.	b.d.	b.d.	b.d.		b.d.	b.d.
Total cation	7.99	8.01	15.86	15.69	8.00	15.71	4.98	7.02	7.99
$Mg/(Mg+Fe^{2+})$	0.20	0.42	0.64	0.67	0.22	0.48			
Prp	12.4	29.5			16.4				
Grs	18.4	13.9			18.8				
Sps	20.0	15.8			7.4				
Alm	49.3	40.7			57.4				
An							20.9		
Ps									25.5

b.d.=below detection limit; n.d.=not determined

Table 1.3 continued

Sample No. (area)	D113-9 (Dalrymple)					D113-2 (Dalrymple)		
Lithology	Amphibolite					Ep Amphibolite		
Mineral	Hbl1	Hbl3	Pl1	Ep1	Chl3	Hbl1	Pl1	Ep1
Occurrence	Matrix	Hbl alt	Matrix	Matrix	Hbl alt	Matrix	Matrix	Matrix
Core/Mantle/Rim	Rim	Rim	Rim	Rim		Rim	Rim	Rim
SiO_2	47.68	51.54	64.97	38.62	27.33	45.08	65.03	38.17
TiO_2	0.43	0.07	b.d.	b.d.	0.03	0.82	b.d.	0.17
Al_2O_3	11.91	2.95	22.23	25.58	22.07	11.64	22.14	23.94
Cr_2O_3	0.11	0.05	b.d.	0.05	0.13	0.07	0.01	b.d.
FeO	10.28	20.31	b.d.		12.65	14.28	0.13	
Fe_2O_3				10.355				12.618
MnO	0.37	0.40	b.d.	0.17	0.23	0.21	b.d.	0.10
MgO	13.96	9.22	0.02	0.05	23.17	12.11	0.03	0.06
CaO	11.24	11.94	3.01	23.66	b.d.	10.22	3.05	23.34
BaO	0.03	b.d.	b.d.	0.06	b.d.	0.18	0.06	0.08
Na_2O	1.90	0.52	10.31	b.d.	0.02	2.58	10.34	b.d.
K_2O	0.21	0.28	0.10	b.d.	0.01	1.27	0.09	b.d.
F	b.d.	0.01	n.d.	0.04	0.01	0.14	n.d.	0.01
Cl	0.01	0.01	n.d.	b.d.	0.01	b.d.	n.d.	<0.01
-O≡F		0.00		0.01	0.00	0.06		0.01
-O≡Cl	0.00	0.00			0.00			0.00
Total	98.14	97.28	100.64	98.57	85.65	98.61	100.86	98.50
Number of O	23	23	8	12.5	28	23	8	12.5
Si	6.81	7.75	2.85	3.02	5.50	6.62	2.85	3.01
Ti	0.05	0.01	b.d.	b.d.	<0.01	0.09	b.d.	0.01
Al	2.01	0.52	1.15	2.36	5.23	2.02	1.14	2.23
Cr	0.01	<0.01	b.d.	<0.01	0.01	<0.01	<0.01	b.d.
Fe^{2+}	1.23	2.55	b.d.		2.13	1.75	<0.01	
Fe^{3+}	<0.01	<0.01		0.61		<0.01		0.75
Mn	0.05	0.05	b.d.	0.01	0.04	0.03	b.d.	0.01
Mg	2.97	2.07	<0.01	0.01	6.95	2.65	<0.01	0.01
Ca	1.72	1.92	0.14	1.98	b.d.	1.61	0.14	1.97
Ba	<0.01	b.d.	b.d.	<0.01	b.d.	0.01	<0.01	<0.01
Na	0.53	0.15	0.88	b.d.	0.01	0.74	0.88	b.d.
K	0.04	0.05	0.01	b.d.	<0.01	0.24	<0.01	b.d.
F	b.d.	<0.01		0.01	0.01	0.07		<0.01
Cl	<0.01	<0.01		b.d.	<0.01	b.d.		<0.01
Total cation	15.41	15.08	5.02	8.00	19.87	15.82	5.02	7.99
$Mg/(Mg+Fe^{2+})$	0.71	0.45			0.77	0.60		
Prp								
Grs								
Sps								
Alm								
An			13.8				13.9	
Ps				20.5				25.2

b.d.=below detection limit; n.d.=not determined

Table 1.4 continued

Sample No. (area)	B214-14 (Botoon)			B214-29 (Botoon)					
Lithology	Ky-Ep-Grt schist			Ky-Hbl schist					
Mineral	Grt2a		Ep2a	Hbl2a	Oam2a	Ky2a	Hbl2b	Oam2b	Ky2b
Occurrence	Ky inclusion		Matrix	Matrix	Matrix	Matrix	Matrix	Matrix	Matrix
Core/Mantle/Rim	Core	Rim	Rim	Rim		Rim	Rim		
SiO_2	39.50	39.91	30.38	44.88	47.66	36.85	45.11	48.57	37.10
TiO_2	0.35	0.10	35.23	0.22	b.d.	0.14	0.37	0.11	b.d.
Al_2O_3	21.22	21.79	1.95	13.55	13.98	59.91	14.34	13.06	60.87
Cr_2O_3	b.d.	b.d.	b.d.	0.98	0.64	1.85	0.05	b.d.	0.67
FeO	17.35	16.58		9.59	11.39		8.85	11.73	
Fe_2O_3			1.19			1.98			1.39
MnO	7.34	6.93	0.18	0.62	1.03	0.04	0.56	1.09	0.05
MgO	8.12	8.07	b.d.	14.39	19.86	0.02	14.69	21.38	0.02
CaO	6.26	6.84	28.98	9.95	0.69	0.02	10.12	0.68	b.d.
BaO	n.d.	n.d.	0.08	0.09	b.d.	0.09	b.d.	b.d.	b.d.
Na_2O	n.d.	n.d.	0.05	1.81	1.19	b.d.	2.04	1.37	0.01
K_2O	n.d.	n.d.	0.03	0.27	b.d.	b.d.	0.26	b.d.	0.01
F	n.d.	n.d.	0.03	0.04	0.12	0.03	0.10	b.d.	b.d.
Cl	n.d.	n.d.	b.d.	<0.01	b.d.	b.d.	0.01	b.d.	b.d.
-O≡F			0.01	0.02	0.05	0.01	0.04		
-O≡Cl				0.00			0.00		
Total	100.14	100.21	98.10	96.38	96.55	100.93	96.48	97.99	100.10
Number of O	12	12	12.5	23	23	20	23	23	20
Si	3.03	3.04	2.53	6.49	6.74	4.00	6.47	6.77	4.03
Ti	0.02	0.01	2.21	0.02	<0.01	0.01	0.04	0.01	b.d.
Al	1.92	1.96	0.19	2.31	2.33	7.66	2.42	2.14	7.79
Cr	b.d.	b.d.	b.d.	0.06	0.04	0.08	<0.01	b.d.	0.03
Fe^{2+}	1.11	1.06		1.16	1.35		1.06	1.37	
Fe^{3+}	<0.01	<0.01	0.07	0.36	<0.01	0.16	0.40	<0.01	0.11
Mn	0.48	0.45	0.01	0.08	0.12	<0.01	0.07	0.13	<0.01
Mg	0.93	0.92	b.d.	3.10	4.19	<0.01	3.14	4.44	<0.01
Ca	0.51	0.56	2.59	1.54	0.10	<0.01	1.56	0.10	b.d.
Ba			<0.01	0.01	b.d.	<0.01	b.d.	b.d.	b.d.
Na			0.01	0.51	0.33	b.d.	0.57	0.37	<0.01
K			<0.01	0.05	b.d.	b.d.	0.05	b.d.	<0.01
F			0.01	0.02	0.05	0.01	0.05	b.d.	b.d.
Cl			b.d.	<0.01	b.d.	b.d.	<0.01	b.d.	b.d.
Total cation	7.99	7.98	7.64	15.70	15.24	11.93	15.82	15.33	11.97
$Mg/(Mg+Fe^{2+})$	0.45	0.46		0.73	0.76		0.75	0.76	
Ps			28.0						

b.d.=below detection limit; n.d.=not determined

Table 1.4 Representative analyses of rock-forming minerals in the matrix

Sample No. (area)	N215-3 (Nanad)					
Lithology	Grt-Hbl-Bt schist					
Mineral	Hbl2a	Bt2a	Bt2b	Bt3	Ms3	Chl3
Occurrence	Porphyroclast		Matrix	Matrix	Matrix	Matrix
Core/Mantle/Rim	Rim					
SiO_2	45.96	40.97	40.45	40.55	49.37	28.16
TiO_2	0.30	0.87	1.06	1.03	0.66	0.18
Al_2O_3	13.67	17.51	16.91	16.52	30.40	21.45
Cr_2O_3	0.13	b.d.	0.27	0.13	0.05	0.19
FeO	10.39	9.55	9.74	9.42	3.89	9.77
Fe_2O_3						
MnO	0.63	0.27	0.32	0.36	0.03	0.41
MgO	14.13	17.03	17.04	17.27	2.52	25.44
CaO	9.02	0.10	0.03	0.03	0.03	b.d.
BaO	b.d.	0.14	0.23	0.03	0.19	0.06
Na_2O	3.23	0.38	0.15	0.14	0.73	b.d.
K_2O	0.23	7.85	8.58	8.45	6.07	b.d.
F	b.d.	0.15	b.d.	0.16	0.12	0.01
Cl	b.d.	b.d.	b.d.	0.01	<0.01	0.01
-O≡F		0.06		0.07	0.05	0.00
-O≡Cl				0.00	0.00	0.00
Total	97.68	94.82	94.77	94.10	94.06	85.67
Number of O	23	11	11	11	11	28
Si	6.59	2.94	2.92	2.94	3.29	5.58
Ti	0.03	0.05	0.06	0.06	0.03	0.03
Al	2.31	1.48	1.44	1.41	2.38	5.01
Cr	0.01	<0.01	0.01	<0.01	<0.01	0.01
Fe^{2+}	1.25	0.57	0.59	0.57	0.22	1.62
Fe^{3+}	0.11					
Mn	0.08	0.02	0.02	0.02	<0.01	0.07
Mg	3.02	1.82	1.84	1.87	0.25	7.52
Ca	1.39	0.01	<0.01	<0.01	<0.01	b.d.
Ba	b.d.	<0.01	0.01	<0.01	<0.01	<0.01
Na	0.90	0.05	0.02	0.02	0.09	b.d.
K	0.04	0.72	0.79	0.78	0.52	b.d.
F	b.d.	0.03	b.d.	0.04	0.03	<0.01
Cl	b.d.	b.d.	b.d.	<0.01	<0.01	<0.01
Total cation	15.73	7.69	7.69	7.73	6.82	19.86
$Mg/(Mg+Fe^{2+})$ Ps	0.71	0.76	0.76	0.77		0.82

b.d.=below detection limit; n.d.=not determined

1.5 Results

1.5.1 Petrography and mineral chemistry of blocks

1.5.1.1 Garnet amphibolites

The earliest stage of metamorphism and deformation (Stage 1a in Table 1.2) is preserved in the Grt amphibolite blocks (Fig. 1.5a,b; Botoon: B213-8, B214-21; Dalrymple: D113-14, D113-15, D113-18). The Grt amphibolite blocks consist mainly of Grt+Camp+Ep(Czo)+Qz with accessory minerals Rt+Ilm+Bt (Table 1.1). Plagioclase is absent in Grt amphibolite samples from Botoon while it occurs as a major matrix mineral (Pl1b in Table 1.2) in one block from Dalrymple point (D113-15), and in minor amounts (<5 vol%) in two Dalrymple point samples (D113-14 and D113-18; Table 1). Secondary minerals such as epidote and chlorite occur as veins and along grain boundaries.

The Grt porphyroblasts in these samples exhibit pronounced concentric compositional zoning marked by increasing pyrope content and Mg# [= $Mg/(Mg+Fe^{2+})$] and decreasing spessartine content from core (e.g. B214-21 =$Alm_{46-51}Prp_{10-19}Grs_{15-20}Sps_{15-25}$) to rim (= $Alm_{38-41}Prp_{30-35}Grs_{13-15}Sps_{13-17}$; Fig. 1.5a–d). Stage 1 is therefore subdivided in the garnet core and its inclusion assemblage (Stage 1a) and the garnet rim and matrix assemblage (Stage 1b). Multiphase solid inclusions (MSI) composed of Chl+Ep+Qz+Grt+Rt+Ilm (B213-9; Fig. 1.5d) occur in the Sps-rich, low Mg# core of some garnet porphyroblasts (Grt1a). The Sps-poor, Mg-rich rim of the garnet porphyroblasts (Stage 1b in Table 1.2) exhibit textural equilibrium, i.e. sharp boundaries, with the surrounding Ca-amphibole (Camp1b), epidote (clinozoisite), quartz, rutile and ilmenite.

The Grt amphibolite block B214-21 used for geothermobarometry (Tables 1.1 and 1.2) contains garnet porphyroblasts distributed parallel to the arrangement of the long axis of hornblende in the matrix. This arrangement defines the foliation (S1) in the Grt amphibolite blocks (Fig. 1.5a). S1 foliation is attributed to the deformation (D1) that affected the blocks prior to the block-in-matrix structure formation (Table 1.2). A quartz-kyanite vein (V1) cuts B214-21 and includes garnet and Ca-amphibole derived from the block.

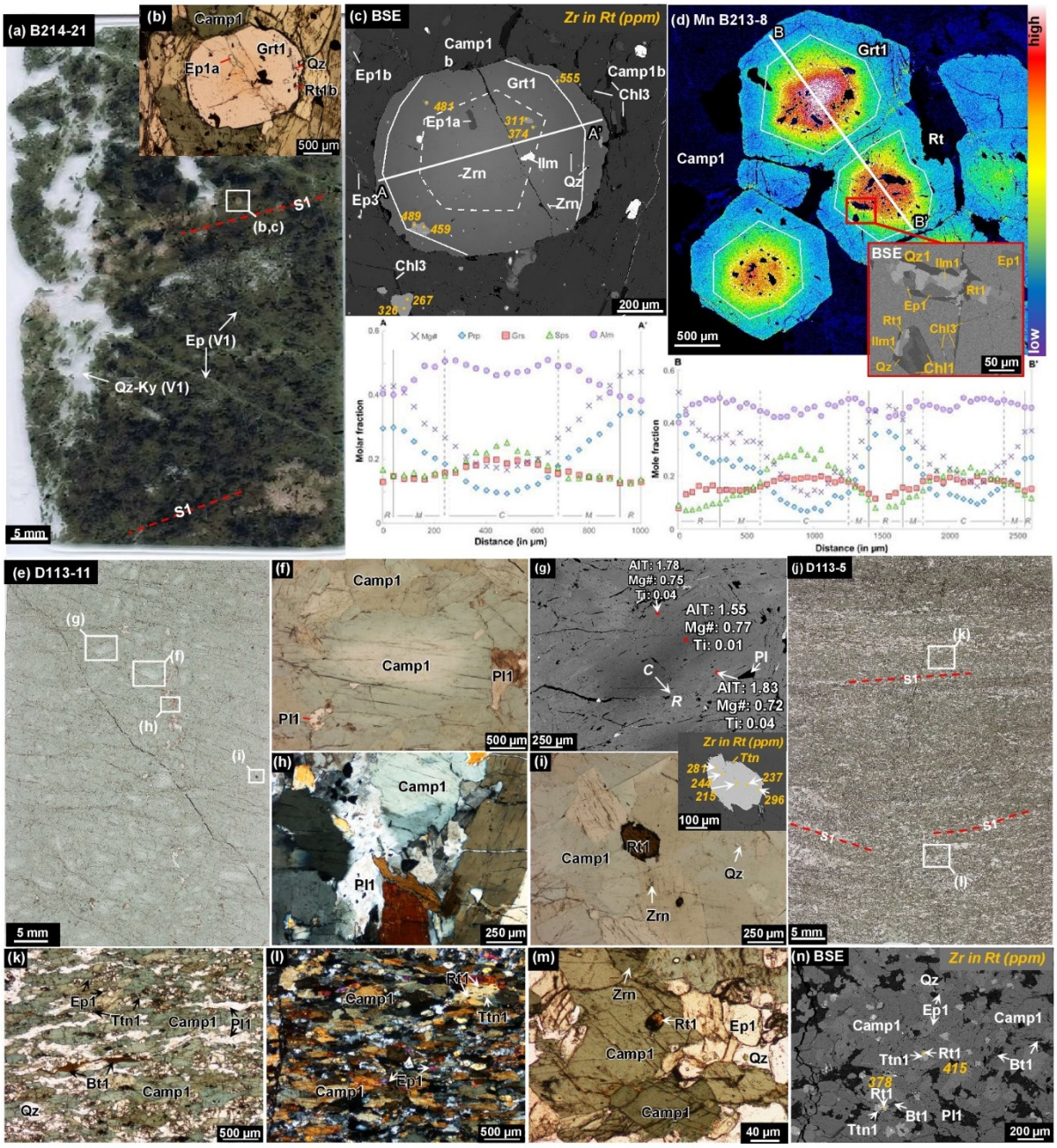

Fig. 1.5. Photomicrographs, BSE images and X-ray elemental map of the blocks. a) Grt amphibolite block showing foliation direction delineated by the linear arrangement of garnet porphyroblasts and long axis direction of Ca-amphibole. An earlier epidote-vein (V1) is transected by a discordant Qz-Ky vein (V1). Garnet porphyroblasts in plane polarized light (PPL; 1.5b) and back-scattered electron image (BSE; 1.5c) showing inclusion assemblage at the core (C), mantle (M) and rim (R) delineated in the line analysis (A-A'). d) X-ray elemental map showing distribution of Mn in the garnet porphyroblast and the multiphase solid inclusion (MSI) composed of Rt+Ilm+Chl+Qz+Ep+Qz at the garnet core identified by line analysis (B-B'). e) PPL; Amphibolite block composed of f) PPL; Coarse Ca-amphibole with optical zonation. g) BSE image of one Ca-amphibole showing difference in Al_T, Mg# and Ti content of the core (C) compared to the rim (R). h) in cross-polarized light (XPL), plagioclase (Pl1) in the amphibolite blocks are mostly interstitial while i) in PPL; Rutile grains are sometimes partially replaced by titanite. j, k) in PPL; l) in XPL; Epidote amphibolite are fine-grained and composed of foliated Camp+Bt+Pl+Ep+Qz+Ttn. m) in PPL; Rt+Zrn+Qz assemblage included in the Ca-amphibole and n) BSE; In the matrix surrounded by titanite.

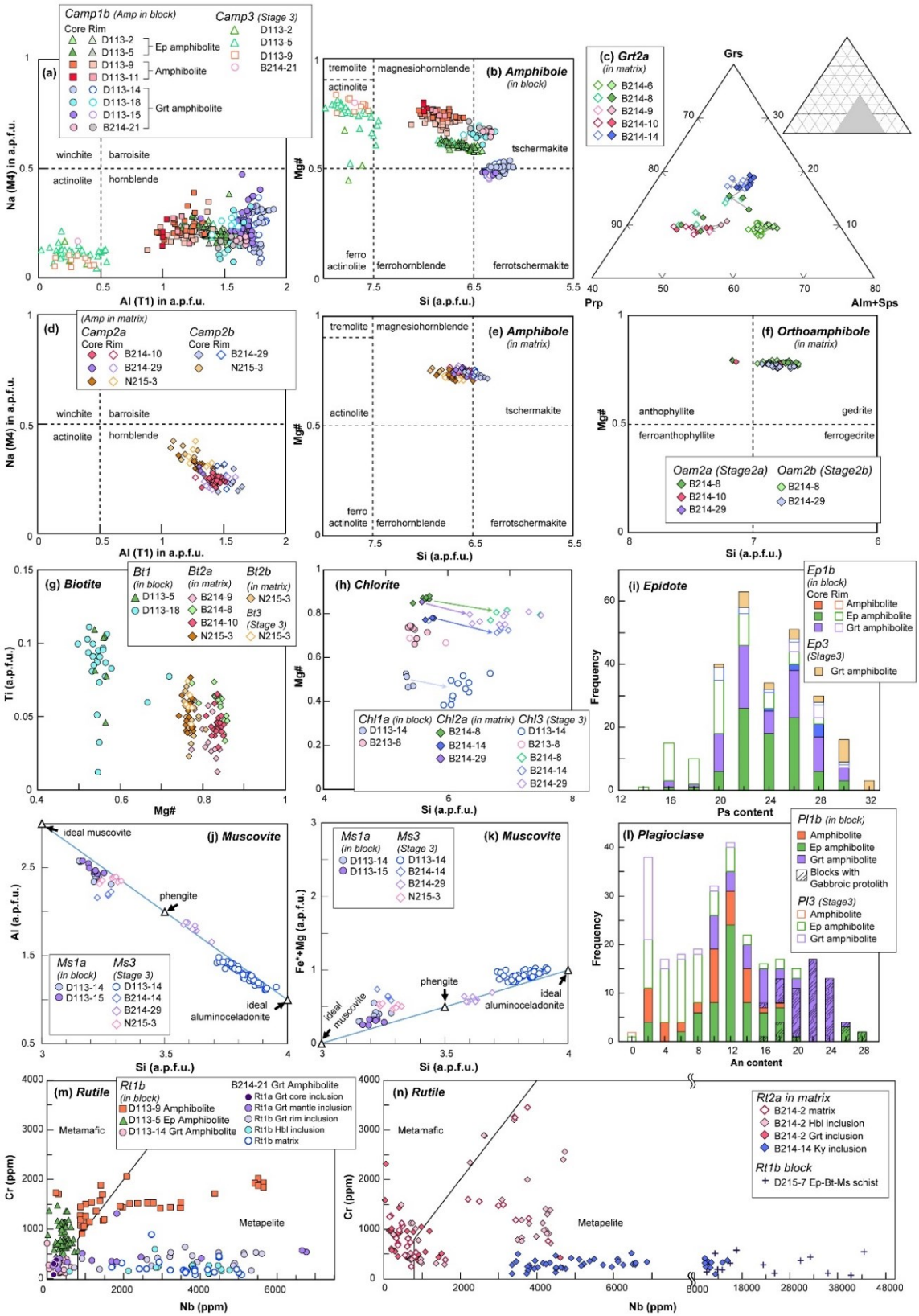

Fig. 1.6. Mineral chemistry of blocks and matrix from the Dalrymple Amphibolites. Legends are the same for a and b, and d and e. a, b) Amphibole in the blocks. c) Garnet composition and d, e) Amphiboles in the matrix2a samples. f) Point analysis of orthoamphiboles in the matrix and g) Biotite and h) Chlorite in the Ep amphibolite (triangle), Grt amphibolite (circles) blocks and matrix samples. i) Histogram showing pistacite content of epidote in the Dalrymple Amphibolites. j, k) Point analysis of muscovite in the Grt amphibolite blocks compared to Stage 3 alteration. l) Histogram of the anorthite content of plagioclases. m, n) Cr vs Nb concentration of rutile grains in the blocks and the matrix. Note the change in scale in Fig. 1.6 m, n to accommodate the high-Nb rutile grains. The metamafic and metapelite fields are from Meinhold et al. (2008).

These minerals incorporated in the vein have the same composition and zoning pattern (in the case of garnet) as those in the block (Fig. 1.5a). There is no reaction zone between the vein and block. Furthermore, local Al-rich domains are observed in this sample where minor amounts of (< 5%) kyanite (Ky1b) and epidote (Czo1b) are in textural equilibrium with the garnet porphyroblasts (Table 1.2).

The Ca-amphibole (Camp1b) in the Grt amphibolite blocks range from ferrotschermakite to tschermakite with minor magnesiohornblende (Fig. 1.6a, b). Some Ca-amphibole in the matrix of these blocks show increasing Si, Al and Mg# from the core to the rim (Fig. 1.6a, b). Other Stage1b Ca-amphibole (Camp1b) grains are replaced along grain boundaries by either actinolite (Camp3) or chlorite (Chl3). Chlorite (Chl1a) inclusions in the garnet core generally have lower Si (= 5.3–5.4 a.p.f.u.) and higher Mg# (= 0.46–0.53) than replacive chlorite (Chl3 in Table 1.2; Si = 5.9–6.7 a.p.f.u., Mg# = 0.38–0.53) and epidote (Ep3 in Table 1.2). These replacive chlorite (Chl3) occurs as veins and as secondary minerals surrounding garnet and Ca-amphibole rims (Fig. 1.5a-c). Muscovite hosted by garnet in the Grt amphibolite blocks (Ms1a; Table 1.2) have moderate phengite component (Ms1; Si = 3.13–3.28 a.p.f.u.) whereas fine mica aggregates (Ms3) are classified as aluminoceladonite (Fig. 1.6j,k). Plagioclase in some Grt amphibolite blocks have low Ca-content (D113-14 = An_{10-16}, D113-18 = $An_{10–18}$) and some are rimmed by albite (Pl3 = $An_{<5}$; Fig. 1.6l). An exception to this is the Grt amphibolite block D113-15 composed mostly of Ca-rich plagioclase ($An_{15–24}$). Whole-rock data reveals a gabbroic protolith for this sample (cf. Part 2).

Rutile grains in the Grt amphibolite block D113-14 have low Nb and Cr content while those in B214-21 exhibit systematic variability in their chemistry. Rutile grains included in the garnet core (Rt1a in Table 1.2) of B214-21 have low Zr (Fig. 1.7) and Nb contents (175–266 ppm; Fig. 1.6 m). Those enclosed in the garnet mantle and rim have higher Nb concentration, 161–6664 ppm and 720–5606 ppm, respectively (Fig. 1.6 m). These values are comparable to the Nb content of rutile in the matrix (1692-5082 ppm) and those included in Camp1b (587–4760 ppm). These high Nb rutile grains are grouped as Rt1b in Table 1.2.

1.5.1.2 Amphibolites

The amphibolite lenses (D113-9; D113-11) hosted in Ep amphibolites in Dalrymple point are composed almost exclusively (~90 %) of coarse Ca-amphibole along with minor amounts of Ep+Pl+Qz+Rt+Ttn (Table 1.1; Fig. 1.5e, f). The absence of garnet porphyroblasts in the amphibolite blocks limits the use of mode of occurrence in discriminating between garnet inclusion assemblage (Stage 1a) and the matrix assemblage (Stage 1b). Some of the Ca-amphiboles (Camp1b) in the amphibolites show optical zonation (Fig. 1.5f) and have dark (low Al_T = 1.55 a.p.f.u., high Mg# = 0.77) cores and brighter (high Al_T = 1.78–1.83 a.p.f.u., low Mg# = 0.72–0.75) rims in BSE images (Fig. 1.5g). Compared to Camp1b in the Grt amphibolites, the amphiboles in amphibolites are mostly magnesiohornblende and have lower total Al content (Al_T) and higher Si and Mg# (Fig. 1.6a, b). Actinolite (Camp3 in Table 1.2) replacing Camp1b is also more common in the amphibolite blocks (Fig. 1.6a, b). The plagioclase (Pl1b) in the amphibolite blocks are $An_{2\text{-}17}$ in composition, while epidote (Ep1b) are clinozoisite (= $Ps_{20–22}$). Rutile (Rt1b in Table 1.2) occurs in small quantities in the amphibolites and is sometimes partially surrounded by titanite (Fig 1.5i inset). Some rutile grains in the matrix show increasing Zr content towards the rim (Fig. 1.5i). Rutile in these blocks generally have low Nb content (748–1782 ppm) although some grains in D113-9 have higher Nb concentration (Fig. 1.6 m).

1.5.1.3 Epidote amphibolites

The Ep amphibolites in Dalrymple point (D113-2, D113-5; Fig. 1.5j–n) are fine-grained (~0.2 mm) and consist mainly of Camp1b, Pl1b, Qz1b, and Ep1b (Czo; core = $Ps_{20–29}$; rim = $Ps_{22–27}$) with Rt+Ttn+Bt as accessory minerals (Table 1.1). Like the Grt amphibolite in Botoon point, the Ep amphibolite blocks in Dalrymple are highly foliated. The foliation (S1), marked by the arrangement of Ca-amphibole (Camp1b), epidote (Ep1b) and biotite (Bt1b) (Fig. 1.5j–l), is associated to the deformation of the blocks (D1). The Ca-amphibole are mostly tschermarkite-magnesiohornblende and show similar chemical zonation pattern as those in the amphibolite blocks. Ca-amphibole has higher Mg# and lower Al content at the core than the rim (Fig. 1.6a). Replacement of Camp1b by

actinolite (Camp3) is more common in the Ep amphibolites compared to the Grt amphibolites (Fig. 1.6a-b). The growth of actinolite in some Ep amphibolite samples are linked to late stage quartz veins (V3). In the sample D113-1, replacement of hornblende (Camp1b) by actinolite (Camp3) is more pervasive closer to a V3 Qz-vein (Act zone) which crosscuts its foliation (cf. Section 1.5.3.3). Plagioclase (Pl1) in the Ep amphibolite have low An content (e.g. D113-2 = $An_{7–15}$, D113-5 = $An_{1–12}$) although those in D113-8 are more anorthitic ($An_{16–27}$, Fig. 1.6l). Similar to the Grt amphibolite sample D113-15, whole-rock data also show a gabbroic protolith for this Ep amphibolite block with An-rich plagioclase (cf. Part 2). Minor biotite (Bt1 in Table 1.2) in the Ep amphibolites occurs as anhedral interstitial grains (Fig. 1.5k–l). The Mg# (0.53–0.56) and Ti (0.05–0.11 a.p.f.u.) of Bt1b in the Ep amphibolites are comparable to those in the Grt amphibolite block D113-18 (Mg# = 0.50–0.58; Ti = 0.01–0.11 a.p.f.u.; Fig. 1.6g). Titanite is also more common in this lithology. Rutile (Rt1b) in the Ep amphibolite records the lowest Nb concentration (<958 ppm; Fig. 1.6m). Lastly, rutile in the Ep-Bt-Ms schist block sample 215-7 have the highest Nb concentrations ranging from 1.5-6.2 wt.% (Fig. 1.6m, n).

1.5.2 Petrography and mineral chemistry of matrix2a and matrix2b

Stage 2 in Table 1.2 is assigned to the two generations of matrix (2a and 2b) surrounding the blocks of the Dalrymple Amphibolite. The mineral assemblage of matrix2a is highly variable but always includes kyanite (Ky2a) and ilmenite (Ilm2a; Fig. 1.8a–d). Hornblende (Camp2a), biotite (Bt2a), quartz (Qtz2a) and garnet (Grt2a) are present in most matrix samples but are sometimes absent in other samples (Table 1.1). Minor chlorite (Chl2a) occurs as local inclusions in kyanite and Ca-amphibole in B214-8 and B214-2G (Table 1.2). Orthoamphibole is also present in some matrix2a samples (e.g. Oam2a in B214-29; Table 1.1) coexisting with Ca-amphibole (Camp2a). Accessory minerals include Ap+Rt while secondary minerals, muscovite (Ms3), chlorite (Chl3) and epidote (Ep3), are similar to those in the blocks (Fig. 1.8).

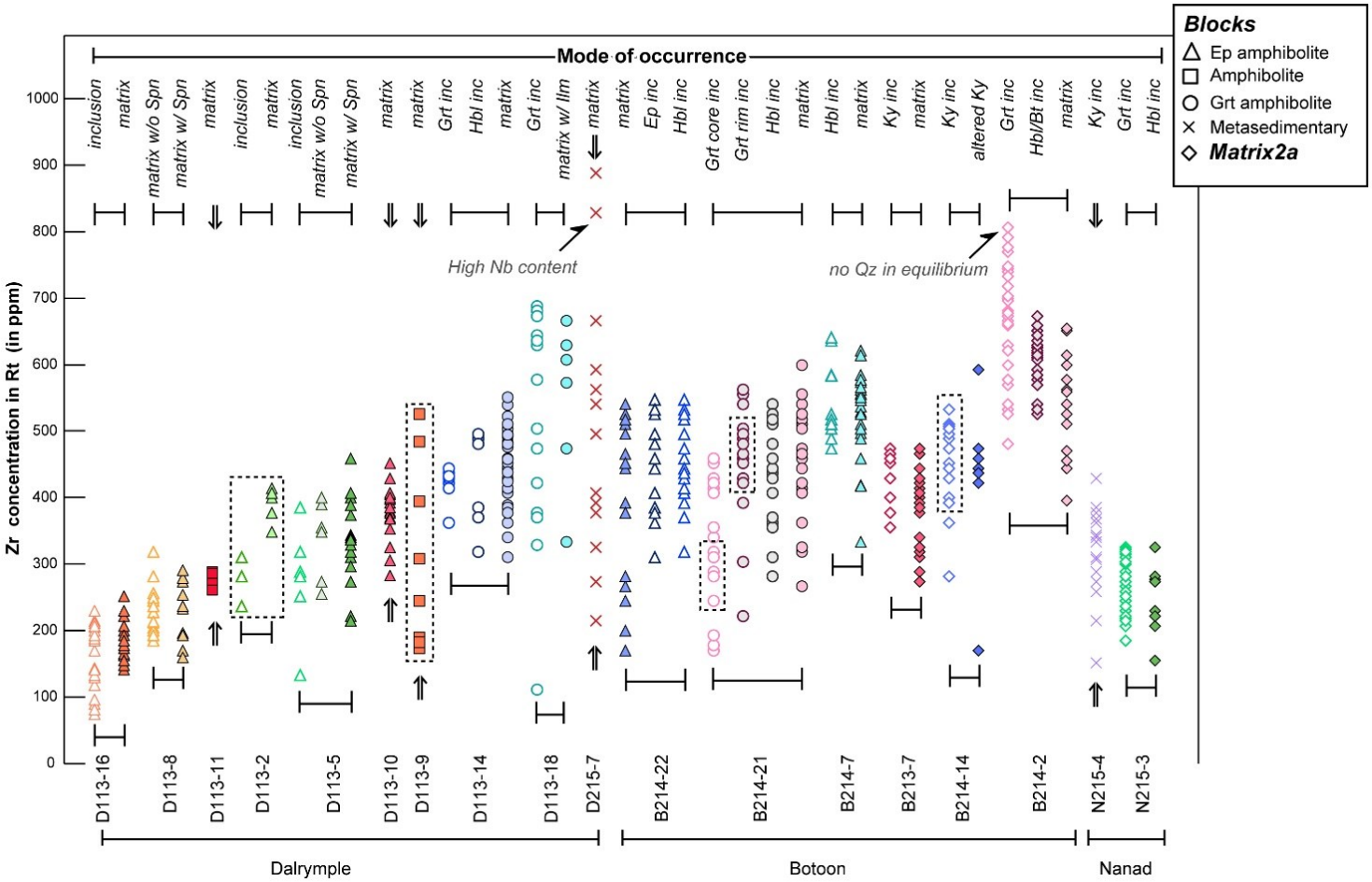

Fig. 1.7. Zr content of rutile grains in blocks and matrix2a samples of Dalrymple Amphibolite and their modes of occurrence. Several factors may result to lower Zr concentration in rutile which may cause the underestimation of peak *T* conditions. These range from primary processes (e.g. timing of formation relative to *P-T* path) to secondary processes such as retrograde growth and diffusive loss during cooling (Penniston-Dorland et al., 2018). In contrast, conditions such as the absence of quartz in equilibrium with rutile observed in B214-2G garnet inclusions could result to higher Zr concentration in rutile (Tomkins et al., 2007). Penniston-Dorland et al. (2018) suggested the use of "Mean Maximum Zr-in-rutile" along with textural constraints in interpreting and estimating peak metamorphic conditions. This method was adopted in this study in selecting rutile analysis used for geothermometry. The rutile grains used for geothermobarmetry in Fig. 1.9 are bordered by rectangles with dashed borders. The rutile grains in the metasedimentary sample D215-7 have very high Nb content (>17,000 ppm) which may have possibly affected its crystal structure (Zack et al., 2004). The Zr content of these rutile grains were therefore not used to estimate *P-T* conditions.

The foliation trend of the matrix2a (S2a) is typically identifiable from the arrangement of elongate minerals Ky2a and Camp2a as well as Bt2a when present (e.g. B214-2G; Fig. 1.8e, j). Garnets in matrix2a are typically euhedral, fine-grained (Grt2a, < 50 μm) and are often included in larger matrix2a minerals (e.g. Ky2a in B214-14; Fig. 1.8h, i). The matrix2a sample B214-2G from Botoon preserves a unique mineral assemblage of coarser Grt2a (~5 mm), staurolite (St2a), kyanite (Ky2a), Ca-amphibole (Camp2a) and biotite (Bt2a) (Fig. 1.8j, k). The foliation (S2a) marked by the elongate minerals in this sample is a clear evidence of the D2a deformation that affected the matrix2a.

Matrix2b in Botoon point is associated with thin shear zones that cut earlier matrix2a (e.g. Fig. 1.8a–c). In this locality they consist of the same minerals (Ky2b, Camp2b, Oam2b in Table 1.2) as the matrix2a that they transect but follow a distinct foliation direction (S2b). Their cross-cutting relationship and the different foliation trend of matrix2b corresponds to a later deformation event (D2b) during Stage 2. In Nanad point, matrix2b is more dominant and D2b is apparently more pervasive. Matrix2b is largely composed of biotite (Bt2b) and quartz which surround garnet (Grt2a) and hornblende (Camp2a) porphyroclasts. Thin overgrowths of Ca-amphibole (Camp2b) and garnet (Grt2b) surround the margins of some Camp2a and Grt2a porphyroclasts, respectively (Fig. 1.8o, p; Table 1.2).

S-C fabrics are observed in this sample (Fig. 1.8l). The S-plane (S2b) is marked by the arrangement of Ca-amphibole (Camp2a) and kyanite (Ky2a) porphyroclasts and the surrounding biotite (Bt2b in Fig. 1.8m–p). The C-plane (C2b, Fig. 1.8l–n), which still contains minor biotite, is largely composed of replacive chlorite (Chl3) and muscovite (Ms3; Fig. 1.8n). Some of the Chl3 and Ms3 in the C-plane (C2b) are arranged parallel to its direction while others are oriented randomly. Both chlorite and muscovite also replaces the Bt2b in the S-plane in matrix2b (Fig. 1.8 m, n).

Garnet (Grt2a in Table 1.2) in the matrix2a (Fig. 1.6c) lack the pronounced chemical zonation observed in the garnet porphyroblasts in the blocks (Fig. 1.5c, d). The Grt2a that do exhibit subtle zonation, preserve increasing Prp and Mg# (e.g. B214-6) from the core ($Alm_{36}Prp_{28}Grs_{17}Sps_{19}$; Mg#

= 0.44) to the rim ($Alm_{36}Prp_{32}Grs_{16}Sps_{16}$; Mg# = 0.47). The Grt2a garnet grains also generally record higher Mg# (e.g. B214-2G, Mg# = 0.44–0.47) and slightly lower Ca content (e.g. B214-2G = $Grs_{16–19}$) compared to the garnet porphyroblasts in the Grt amphibolite blocks (e.g. Grt1a-b in D113-18, Mg# = 0.30–0.38; $Grs_{18–23}$). An exemption to this general distinction between garnet in the blocks (Grt1) and in matrix2a (Grt2a) is the rim stage (Grt1b) of the Grt amphibolite blocks in Botoon. These Grt1b in Botoon blocks (e.g. B214-21) also record comparably high Mg# (Grt1b in B214-21, Mg# = ~0.41; Grt1b in B213-8, Mg# = 0.40–0.47) and low Ca content (Grt1b in B214-21, $Grs_{13–15}$; Grt1b in B213-8 = $Grs_{8–16}$) as the Grt2a.

Calcic amphibole in matrix2a (Camp2a in Table 1.2) is classified as tschermakite to magnesiohornblende (Fig. 1.6d, e). Ca-amphibole (Camp2a) exhibits a generally narrow range of Mg# (0.72–0.78) which is comparably higher than Ca-amphibole in the blocks (Camp1) at a given Si content. Amphibole in samples with two matrix generations, i.e. matrix2a and matrix2b such as B214-29 (Fig. 1.8a–c) and N215-3 (Fig. 1.8l–n), exhibit comparable compositions in terms of Al_T, Mg# and Si (Fig. 1.6d, e). In sample B214-29, the hornblendes (Camp2a) are relatively Cr-rich (matrix2a = 0.12–1.3 wt.% Cr_2O_3; matrix2b = 0.12–0.37 wt.% Cr_2O_3) compared to those in blocks (Camp1 < 0.1% wt.% Cr_2O_3). Orthoamphibole is found exclusively in the matrix surrounding the blocks and mostly ranges from gedrite to anthophyllite (Leake et al., 1997). Like the Ca-amphiboles, the orthoamphiboles in matrix 2a and 2b have the same composition (Mg# and Si; Fig. 1.6f).

Kyanite (Ky2) in the matrix sample B214-29 is also relatively Cr-rich (matrix2a = 0.710 – 2.17 wt.% Cr_2O_3; matrix2b = 0.01–0.67 wt.% Cr_2O_3) compared to other samples. The matrix2a sample B214-5 contains kyanite (Ky2a) grains which are surrounded by fine-grained muscovite (Ms3) connected by radially oriented healed fractures. These fluid-inclusion bearing fractures will be utilized to estimate the *P-T* conditions for the growth of replacive minerals (i.e. Ms3) during Stage 3 as discussed in Section 1.5.3.3. Biotite (Bt2a, b; Fig. 1.6g) and chlorite (Chl2a; Fig. 1.6h) in the matrix are also generally more Mg-rich compared to the blocks.

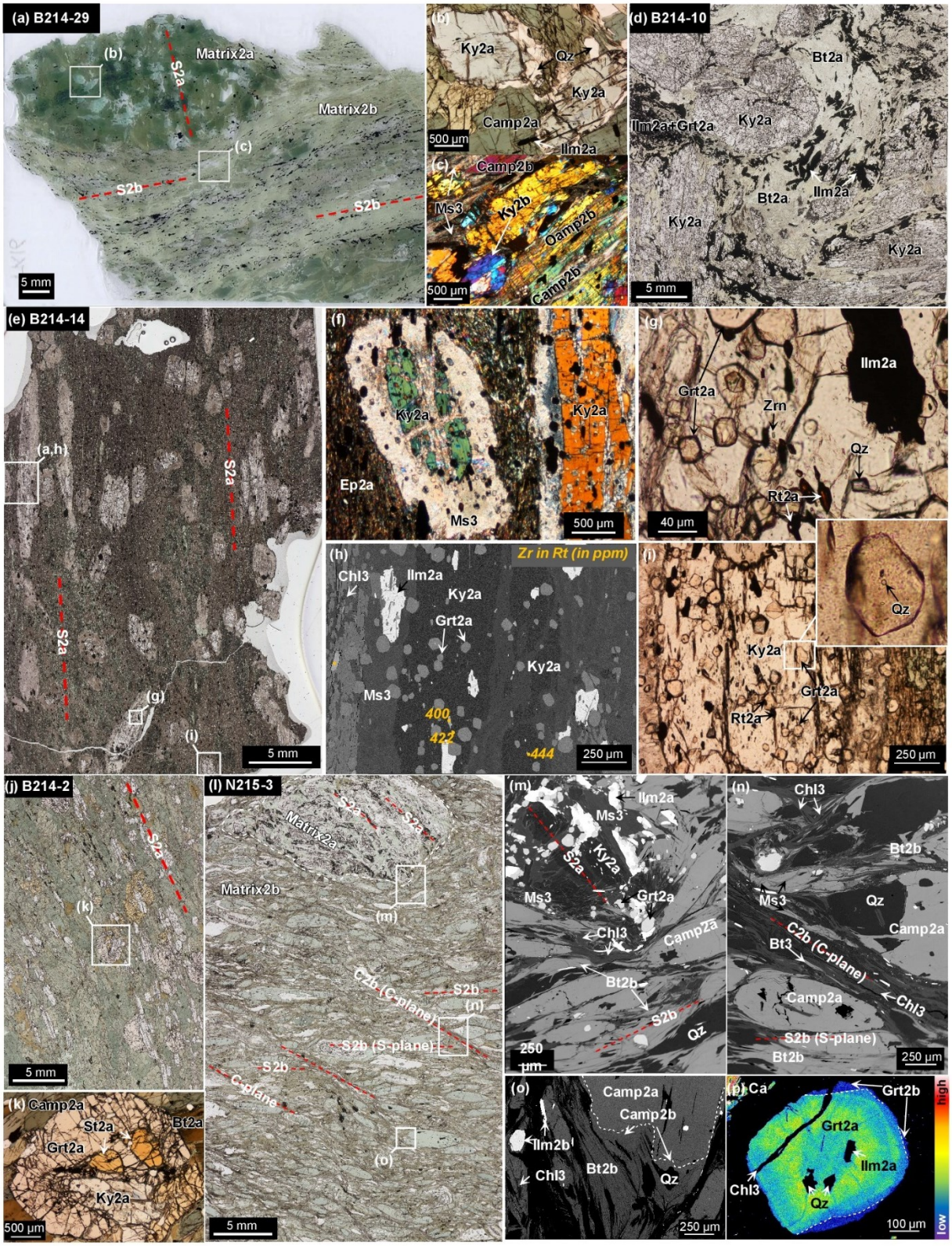
(a) B214-29
(b)
Matrix2a
S2a
Matrix2b
(c)
S2b
S2b
5 mm
(b)
Ky2a
Qz
Ky2a
Camp2a
Ilm2a
500 μm
(c)
Camp2b
Ms3
Ky2b
Oamp2b
Camp2b
500 μm
(d) B214-10
Bt2a
Ilm2a+Grt2a
Ky2a
Bt2a
Ilm2a
Ky2a
Ky2a
5 mm
(e) B214-14
(a,h)
S2a
S2a
(g)
(i)
5 mm
(f)
Ky2a
Ky2a
Ep2a
Ms3
500 μm
(g)
Ilm2a
Grt2a
Zrn
Qz
Rt2a
40 μm
(h)
Zr in Rt (in ppm)
Chl3
Ilm2a
Ky2a
Grt2a
Ky2a
Ms3
400
422
444
250 μm
(i)
Qz
Ky2a
Grt2a
Rt2a
250 μm
(j) B214-2
S2a
(k)
5 mm
(k) Camp2a
St2a
Bt2a
Grt2a
Ky2a
500 μm
(l) N215-3
S2a
S2a
Matrix2a
Matrix2b
(m)
C2b (C-plane)
S2b
(n)
S2b (S-plane)
S2b
C-plane
(o)
5 mm
(m)
Ilm2a
Ms3
S2a
Ky2a
Ms3
Grt2a
Chl3
Camp2a
Bt2b
S2b
Qz
250 μm
(n)
Chl3
Bt2b
Ms3
Qz
Camp2a
Bt3
C2b (C-plane)
Camp2a
Chl3
S2b (S-plane)
Bt2b
250 μm
(o)
Camp2a
Camp2b
Ilm2b
Chl3
Bt2b
Qz
250 μm
(p) Ca
Grt2b
Grt2a
Ilm2a
Chl3
Qz
100 μm
high
low

Fig. 1.8. Photomicrographs (in XPL and PPL) and BSE images of matrix samples. a) in PPL; Matrix2a block with foliation (S2a) surrounded by matrix2b which exhibit a distinct foliation (S2b). b) in PPL; The matrix2a has the same mineralogy as c) Matrix2b (in XPL). d) in PPL; Ilm2a accumulations surrounding coarse Ky2a grains. e, f) in PPL; Matrix2a sample B214-14. g) in PPL; Kyanite porphyroblasts include Zrn-Rt-Qz assemblage used for h) Zr-in-rutile geothermometry (BSE). i) in PPL; Quartz inclusion in garnet (Grt2a) in turn hosted by kyanite used for elastic geobarometry. j, k) in PPL; Grt+St+Bt+Camp+Ky bearing matrix2a. l) in PPL; Matrix2a block surrounded by matrix2b showing crenulations and multiple deformation stages marked by different foliation planes. m, n) BSE images of the matrix2a clast and the matrix2b. o) BSE image of Camp2a porphyroclast with the thin overgrowth of Camp2b equilibrated with Bt2b. p) X-ray elemental map showing distribution of Ca in Grt2a porphyroclast which is also surrounded in some parts by a thin overgrowth of Grt2b.

1.5.3 Geothermobarometry

1.5.3.1 *P-T* estimate for Stage 1

The Zr-in-rutile geothermometry which utilizes rutile grains coexisting with quartz and zircon (Tomkins et al., 2007) was employed on the metamafic blocks of the Dalrymple Amphibolite and the surrounding Ky+Camp+Bt+Ep+Grt matrix2a. Rutile grains included along with zircon and quartz in the core (Stage 1a) and rim (Stage 1b) of garnet porphyroblasts in sample B214-21 (Fig. 1.5a–c) were used to estimate *T* condition preserved in the Grt amphibolite blocks (Fig. 1.9) (e.g. Suzuki and Kawakami, 2019). Rutile grains in the garnet core (Stage 1a) have lower Zr concentrations (170–266 ppm) compared to inclusions in the garnet rim (422–540 ppm Zr; Stage 2b; Fig. 1.5c). Those included in Ca-amphibole (281–540 ppm Zr) and in the matrix (266–540 ppm Zr) exhibit the same maximum Zr concentrations as the rutile grains included in the garnet rim. Rutile grains in the Grt amphibolite blocks from Dalrymple point (D113-14 = 311–551 ppm Zr, D113-18 = 329–689 ppm Zr) record a similar range of Zr concentration (Fig. 1.7).

Several factors may result to lower Zr concentration in rutile which may cause the underestimation of peak *T* conditions. These range from primary processes (e.g. timing of rutile formation relative to *P-T* path) to secondary processes such as retrograde rutile growth and diffusive loss of Zr from rutile during cooling (Penniston-Dorland et al., 2018). In contrast, conditions such as absence of quartz in equilibrium with rutile observed in B214-2G garnet inclusions could result to higher Zr concentration in rutile (Tomkins et al., 2007). Penniston-Dorland et al. (2018) suggested the use of “Mean Maximum Zr-in-rutile” along with textural constraints in interpreting and estimating peak metamorphic conditions. This method was adopted in this study in selecting rutile

analysis used for geothermometry. The rutile grains in the metasedimentary sample D215-7 have very high Nb content (>17,000 ppm) which may have possibly affected its crystal structure (Zack et al., 2004). The Zr content of these rutile grains were therefore not used to estimate *T* conditions.

In the Dalrymple Amphibolite blocks, rutile grains in the matrix (e.g. D113-5 = 348–415 ppm) show maximum Zr concentrations similar to or slightly higher than those which occur as inclusions (e.g. D113-5 = 237–311 ppm). There is no significant difference in the Zr concentration between rutile surrounded by titanite and those without titanite (e.g. D113-8; D113-5). Rutile grains in the Ep amphibolites and amphibolites in Dalrymple show slightly lower Zr concentration than those in the Grt amphibolites but the corresponding difference in peak *T* are small (< 25 °C). The Ep amphibolites in Botoon also have the same Zr concentration as the Grt amphibolites, indicating the stability of epidote at peak *P-T* conditions.

The three Raman bands of quartz inclusions in garnet, i.e. 128, 206 and 464 cm^{-1}, are all shifted towards higher wavenumbers compared to the quartz crystal standard. Replicate analysis showed that the broad 206 cm^{-1} Raman band ($\Delta\nu_{206}$) has the highest variation (n = 84; 2σ = 8 cm^{-1}) while readings of the shifted 464 cm^{-1} ($\Delta\nu_{464}$) band are more precise (n = 84; 2σ = 1.8 cm^{-1}). Quartz inclusions are more abundant at the garnet core (Stage 1a) compared to the rim (Stage 1b). Those at the core have $\Delta\nu_{464}$ = 2.94 ± 0.58 cm^{-1} (n = 16; P_{inc}= 3.29 ± 0.7 kbar using Schmidt and Ziemann, 2000) while the 464 cm^{-1} band of the quartz inclusions at the rim are shifted $\Delta\nu_{464}$ = 2.8 ± 0.65 (n = 8; P_{inc} = 3.14 ± 0.7 kbar using Schmidt and Ziemann, 2000). Other quartz inclusions are either near fractures resulting to lower Raman shifts or are adjacent to other inclusions.

The combined results of Zr-in-rutile geothermometer (Tomkins et al., 2007) and quartz-in-garnet geobarometer (Schmidt and Ziemann, 2000; Angel et al., 2017a, b) applied to inclusions in the garnet porphyroblasts constrain the *P-T* conditions preserved at the garnet core (Stage 1a: ~625 ± 25 °C, 11.5 ± 1.0 kbar) and the garnet rim (Stage 1b: ~700 ± 13 °C, 13 ± 0.5 kbar) of the Grt amphibolite block B214-21 (Fig. 1.9).

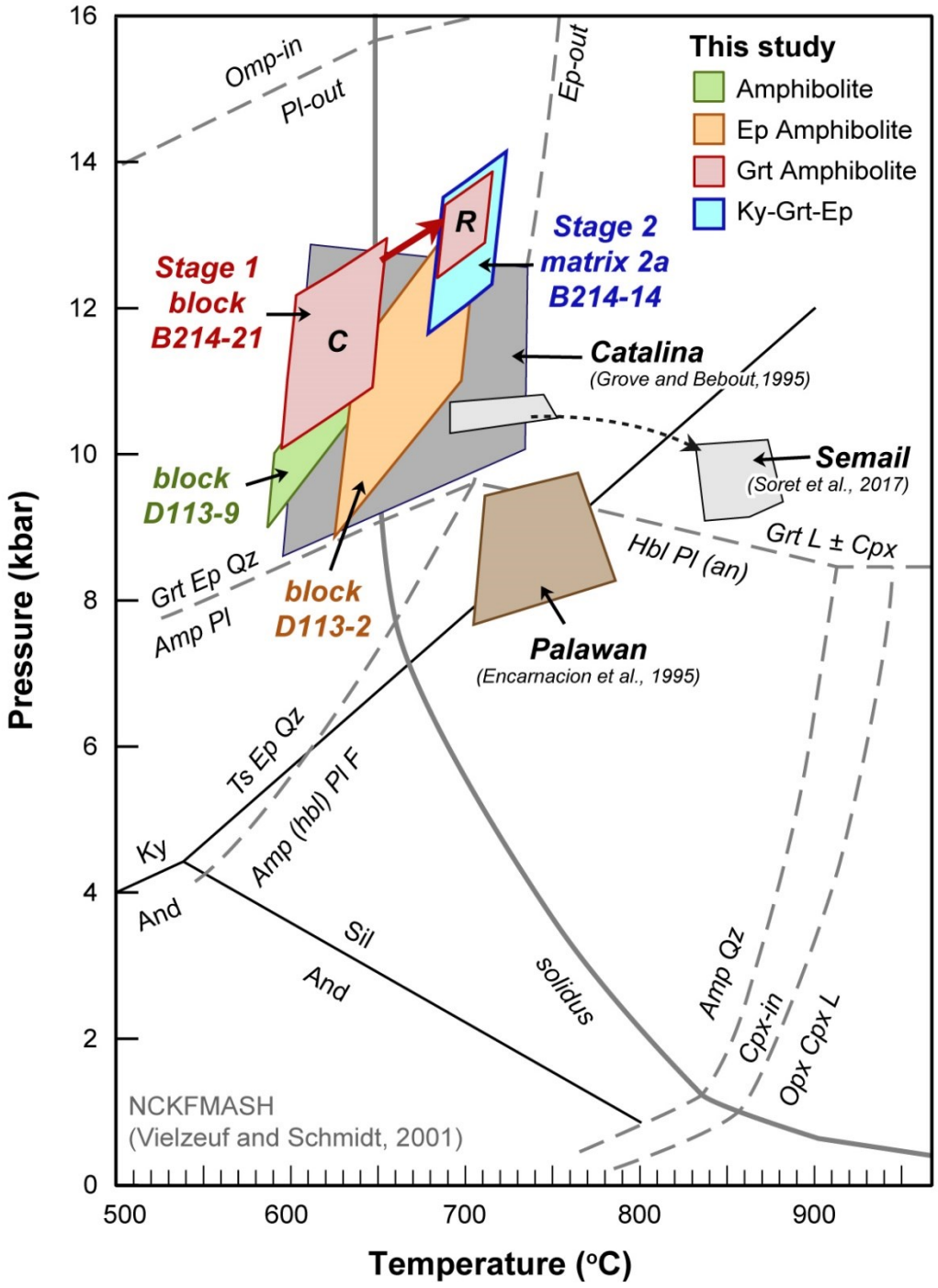

Fig. 1.9. *P-T* estimates for the blocks and matrix2a samples of the Dalrymple Amphibolite. The prograde *P-T* path for the Grt amphibolite block B214-21 was obtained using the inclusion assemblage (Zr-in-rutile geothermometry and quartz-in-garnet geobarometry) at the core (C) and rim (R) of garnet. The estimates for the amphibolite D113-9 and Ep amphibolite blocks D113-2 were determined using Zr-in-rutile geothermometry and the TZARS equilibria. *P-T* conditions of the matrix2a sample B214-14 utilized the same technique as in B214-21. See text for details. The peak *P-T* estimates for the Catalina Schist (Grove and Bebout, 1995) and the Semail Ophiolite (Soret et al., 2017) are also indicated. The petrogenetic grid for metabasalts in the NCKFMASH system (Vielzeuf and Schmidt, 2001) is also shown.

The peak *P-T* conditions of other Grt amphibolite blocks from Dalrymple point were constrained by applying the Grt+Camp+Pl+Qz geobarometer (Kohn and Spear, 1990) using the garnet rim and matrix assemblage (Grt1b+Camp1b+Pl1b+Qz1b) coupled with Zr-in-rutile geothermometry of rutile grains in the matrix (Rt1b) and included in Ca-amphibole (Camp1b) and garnet rim (Grt1b). The obtained *P-T* condition of ~700 ± 45 °C at 13.2 ± 0.9 kbar (D113-14) and 710 ± 40 °C at 11.9 ± 1.3 kbar (D113-18) are comparable to the Stage 1b of B214-21. Note that the *P* obtained for the Grt amphibolite block D113-14 are slightly above the pressure range (2.8–13 kbar) to which the geobarometer of Kohn and Spear (1990) are calibrated.

Zr-in-rutile geothermometer was also applied to rutile grains in the matrix and included in Ca-amphibole in representative Ep amphibolite (D113-2) and amphibolite blocks (D113-9). The Zr concentration of these rutile grains, 237–415 ppm for D113-2 and 174–525 ppm for D113-9, are comparable to the range of values in the Grt amphibolites. There are also no systematic differences in the Zr concentration of rutile grains of different texture, i.e. matrix vs inclusion and with or without titanite envelop (Fig. 1.7) although some coarse rutile grains show increasing Zr concentration towards the rim (Fig. 1.5i). Peak *P* was estimated for the Ep amphibolites and amphibolites by calculating the position of the equilibria: 3 An+ 2 Czo + Rt + Qz = 3 An + Ttn + H_2O (TZARS; Kapp et al., 2009) using the prograde rim of the corresponding minerals, i.e. albitic rims of plagioclase were not considered. The aH_2O was assumed to be high (= 0.95) based on the absence of calcite in the samples which contain Pl+Czo+Ttn and on the results of previous works (Kapp et al., 2009; Picazo et al., 2019). If the actual aH_2O is less than assumed, the calculated position of TZARS equilibria represent the minimum pressure value for these samples. A decrease in the aH_2O of 0.1 (= 0.85) for example increases the *P* by 0.15 kbar whereas a value of aH_2O = 1 lowers the calculated *P* by 0.07 kbar. The constrained *P-T* conditions for the Ep amphibolite (D113-2: ~660 ± 42 °C at 11.4 ± 1.1 kbar) and amphibolite (D113-9: ~616 ± 29 °C at 10.4 ± 0.9 kbar) blocks are within the range of those obtained for the Grt amphibolite blocks albeit slightly lower with respect to *T* and *P* (Fig. 1.9).

1.5.3.2 *P-T* estimate for Stage 2

Zr-in-rutile geothermometer and quartz-in-garnet geobarometer were also applied to the matrix2a sample B214-14. Rutile inclusions in kyanite (Ky2a), and quartz hosted in garnet (Grt2a) which are in turn included in Ky2a were used (Fig. 1.8e–i). The Grt2a (= $Alm_{35–36}Prp_{28–32}Grs_{16–19}Sps_{16–19}$) in this sample are fine-grained and do not preserve clear zonation (Figs. 1.6c; 1.8i). The rutile grains have high Zr concentrations (400–614 ppm). The 464 cm^{-1} Raman band of quartz inclusions in the garnet are also shifted $\Delta\nu_{464}$ = 3.04 ± 0.53 (n=12; P_{inc} = 3.41 ± 0.6 kbar). Using these values, the *P-T* condition preserved in this matrix2a sample (= ~700 ± 16°C, 13 ± 0.9 kbar) are obtained, which is comparable to the rim stage of the metamafic blocks (Fig. 1.9).

1.5.3.3 Microthermometry of secondary fluid inclusions and *P-T* estimate for Stage 3

Low-*T* retrograde overprint is observed in blocks and matrix samples of the Dalrymple Amphibolite. In the matrix2a in sample B214-5, kyanite (Ky2a) grains surrounded by fine-grained muscovite (Ms3) are connected by radially oriented healed fractures (Fig. 1.10a–c). These fractures appear as thin nonluminescent lines compared to the host quartz in CL maps (Fig. 1.10c). The healed fractures contain two-phase aqueous fluid inclusions apparently related to the formation of the fine-grained muscovite pseudomorphing kyanite (Fig. 1.10b). Variation in the homogenization temperatures of the retrograde, secondary fluid inclusions are relatively narrow (T_H = 151.8 ± 17 °C; Fig. 1.10d). The salinity of these fluid inclusions range from 1.82–6.95 wt.% NaCl equivalent using the formula of Bodnar (1993). Bulk density (= 0.94–0.96 g/cm^3) was calculated for these H_2O-NaCl fluid inclusions following Steele-MacInnis et al. (2012). These earlier fractures are transected by later stage fractures which appear as thin subparallel non-luminescent features in the CL maps (Fig. 1.10c).

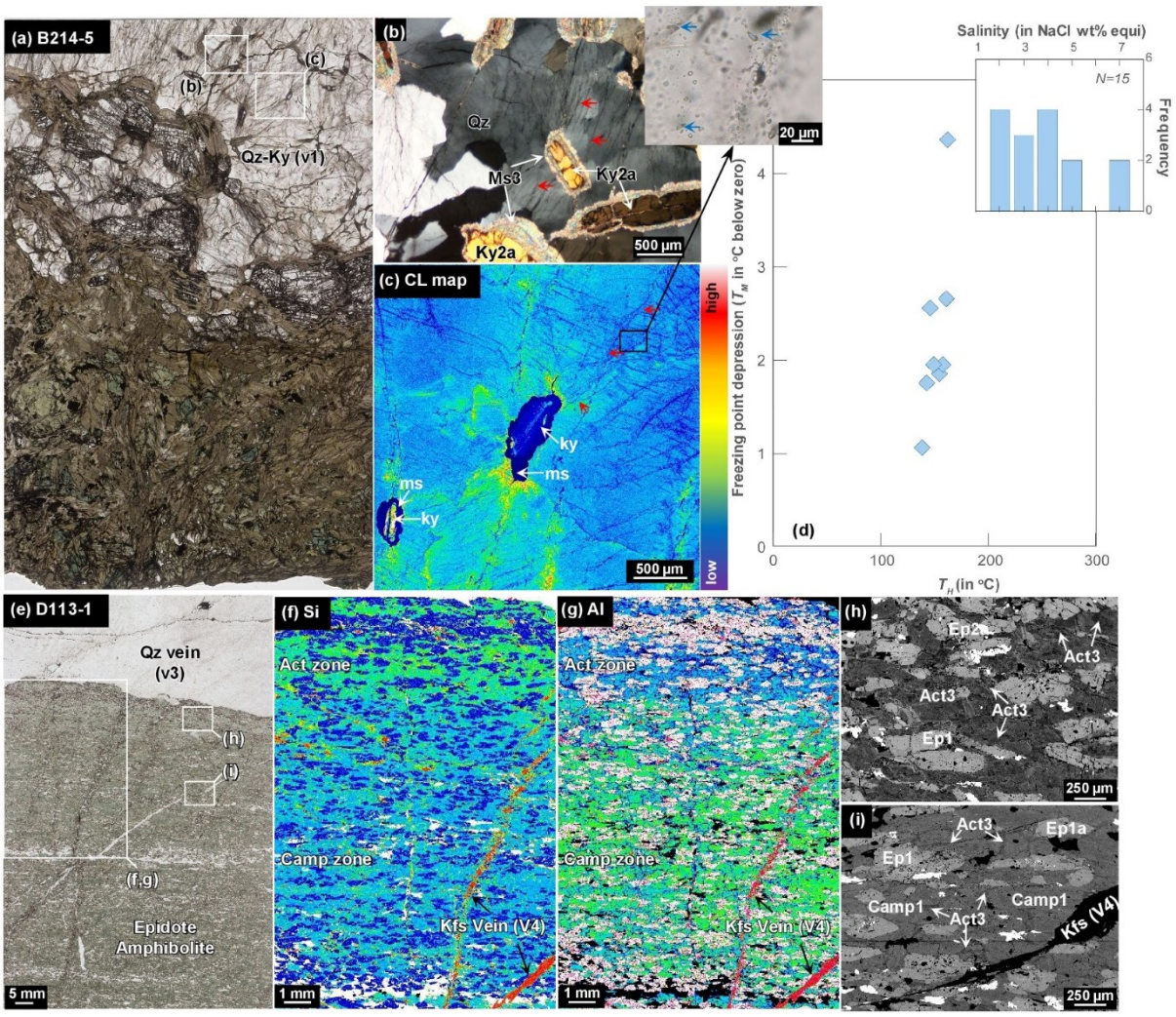

Fig. 1.10. a, b) Photomicrographs of Qz-Ky (B214-5) lens in matrix2a. The Ky2a grains replaced by Ms3 are interconnected by radial fractures (red arrows) that contain fluid inclusion (blue arrows). c) SEM-CL map of Qz-Ky lens. The fractures interconnecting the altered kyanite appear as thin nonluminescent lines marked by red arrows. Inset shows the fluid inclusions contained in these healed fractures. d) Homogenization (T_H) and melting (T_M) temperatures of the fluid inclusions. Histogram shows the salinity of these fluid inclusions calculated using Bodnar (1993). e) Scanned thin section of the Ep amphibolite sample in Dalrymple cut by a Stage 3 (v3) quartz vein. X-ray elemental maps reveal increasing f) Si and decreasing g) Al in the amphiboles towards the vein. BSE images show h) pervasive replacement of Camp1 (hornblende) by actinolite closer to the vein while replacement is limited i) Along grain boundaries farther from the vein.

The subparallel quartz-veins cutting the Ep amphibolite exposure in Dalrymple point (Fig. 1.4f, g) appear related to hornblende replacement by actinolite (Act3 in Table 1.2). In sample D113-1, compositional maps reveal progressively increasing Si, Ca, Mg# and decreasing Na, K and Al towards the quartz vein, i.e. increasing actinolite component (Fig. 1.10f, g). Hornblende grains closest to the veins (0–10 mm; Act zone in Fig. 1.10f–g) are completely to almost completely replaced by actinolite (Fig. 1.10h) whereas farther from the vein (Camp zone in Fig. 1.10f, g), actinolite occur only along grain boundaries forming irregular networks (Fig. 1.10i). Later discordant potassium feldspar-veins transect both Act and Camp zones.

1.5.4 Pseudosection modeling

The pseudosection modeling for matrix2a (B214-10; Fig. 1.11) was done in the Na_2O-MnO-CaO-K_2O-FeO-MgO-Al_2O_3-SiO_2-H_2O-TiO_2 (NMnCKFMASHTO) system using Theriak-Domino (ver 4.2.2017; de Capitani and Brown, 1987, de Capitani and Petrakakis, 2010). The sample shows low degree of Stage 3-related metamorphism, and the peak metamorphism assemblage is largely preserved. The updated database of Holland and Powell (2011) and the activity-composition (*a-x*) relations of Green et al. (2016) for metamafic rocks were used following Jørgensen et al. (2019). H_2O-fluid was included in all assemblages.

The pseudosection for the matrix2a sample B214-10 (Fig. 1.11) well reproduced the observed Stage 2a mineral assemblage (Camp+Grt+Ky+Ilm+Bt+Mag) within the red *P-T* field (Table 1.1): Absence of chlorite is predicted over ~650 °C, which constrains the lower *T* limit of the observed stage 2a mineral assemblage. Hornblende is predicted to be stable from ~550–750 °C coexisting with garnet and kyanite among others. Absence of evidence for partial melting in B214-10 constrains the higher-*T* limit. Kyanite limits the minimum *P* recorded in this matrix2a sample. The peak *P-T* conditions modelled through pseudosection is comparable to that obtained using geothermobarometric techniques (Fig. 1.9).

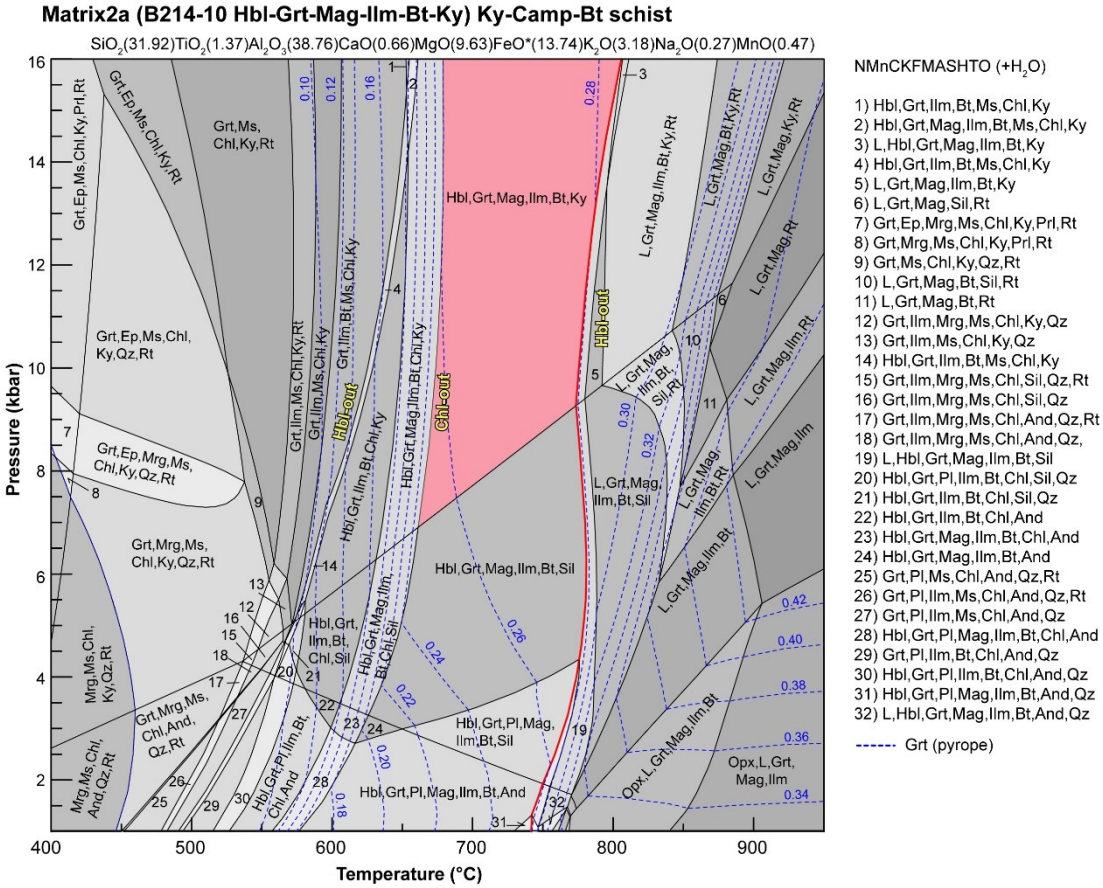

Fig. 1.11. Pseudosection calculated for the representative matrix2a sample B214-10 in the NMnCKFMASHTO system using Theriak-Domino (de Capitani and Brown, 1987; de Capitani and Petrakakis, 2010). Bulk rock composition used for the calculation is in molar percentages (%). Red field corresponds to the peak *P-T* assemblage observed in the samples while the solid red line is the calculated solidus. Isopleths of pyrope content (XPrp) of garnet are shown as blue dash lines.

1.6 Discussion

1.6.1 *P-T-D* history of the Dalrymple Amphibolite

Application of Zr-in-rutile geothermometer (Tomkins et al., 2007) and quartz-in-garnet Raman geobarometer (Schmidt and Ziemann, 2000; Angel et al., 2017a, b) to the Grt amphibolite block, B214-21, successfully determined the prograde *P-T* path (~625°C, 11.5 kbar to ~700°C, 13 kbar) that the blocks experienced (Fig. 1.9). This prograde path is consistent with the garnet zonation, i.e. increasing pyrope and decreasing spessartine content (Fig. 1.5c, d). The Chl+Ep+Qz+Ms MSI preserved in the core of some garnet porphyroblasts in the blocks (Fig. 1.5d) also reflect the transition from Ep amphibolite facies to high-pressure amphibolite facies. Considering the high

variance of these lithologies, the use of trace element geothermometry and elastic geobarometry as successful ways of constraining *P-T* conditions is highlighted in this study.

The net-transfer reaction geobarometer, TZARS equilibria (Kapp et al., 2009), provided additional *P-T* constraints on the Ep amphibolites (Fig. 1.9). This revealed comparable peak metamorphic conditions with the Grt amphibolites in contrast to previous hypothesis (Fig. 1.9; cf. Encarnacion et al., 1995). Earlier works inferred a mid-oceanic ridge basalt (MORB) protolith for much of the metamafic blocks of Dalrymple point (Keenan et al., 2016). Considering the same MORB protolith and since the peak *P-T* conditions are similar for the Grt amphibolites and Ep amphibolite, the prevalence of epidote in the latter type can possibly be attributed to earlier modification of the basaltic protolith (i.e. Ca metasomatism) relative to typical MORB (Wei and Duan, 2018). The randomly-oriented epidote veins cutting the amphibolite block in Botoon (Fig. 1.2c) and Dalrymple further support Ca metasomatism of some metamafic blocks. Modifications in the chemistry of basaltic rocks formed in spreading centers, especially in terms of Ca, Na and Mg, is prevalent during hydrothermal alteration (e.g. Seyfried et al. 1988). Whole-rock data also reveal the CaO content of Ep amphibolites to be higher at a given FeO/MgO ratio than the Palawan Ophiolite basalts (Part 2). The same scenario has been documented in other ophiolites (e.g. epidosites in Semail; Gilgen et al., 2016) and greenstone belts (Starr and Pattison, 2019). The pre-D1 modification of the Ep amphibolites is suggested by the similar fine-grained texture and foliation trend shared by the epidote-rich and epidote-poor domains of the amphibolites in Dalrymple (Fig. 1.4j-k). The random orientation of epidote veins cutting the metamafic blocks in Botoon furthermore suggest that Ca-metasomatism of the metamafic blocks persisted during prograde metamorphism, i.e. subduction of the slab (Fig. 1.2c).

Compared to Grt amphibolite blocks, garnet in the matrix2a (Grt2a) does not exhibit pronounced zonation. The single *P-T* condition constrained on matrix2a (~700°C, 13 kbar) is essentially the same as the peak conditions preserved in the blocks. This indicate that the matrix-forming deformation (Stage 2, D2a) likely started *en route* towards peak *P-T* conditions at depths of around ~45 km using the density values of Jagoutz and Behn (2013). Pseudosection modelling

further supports that the dominant mineral assemblage which comprise the matrix2a, i.e. Ca-amphibole, garnet, biotite, kyanite, and ilmenite, were stable at relatively high *P-T* conditions (Fig. 1.11) comparable to the peak metamorphic conditions of the blocks determined by geothermobarometry (Fig. 1.9). This suggests that the unique bulk composition of the matrix2a was largely fixed prior to reaching peak metamorphic conditions. Consequently, the deformation of the blocks (D1) and matrix2a (D2a; Table 1.2) may have occurred continuously as the whole mélange complex was being transported towards greater depths (i.e. prograde path in Fig. 1.9). In the Catalina Schist, California, the formation of the block-in-matrix structure is considered to have also started at lower *P-T* (i.e. blueschist facies) and the block-in-matrix complex was metamorphosed together towards higher grades, i.e. amphibolite facies (e.g. Penniston-Dorland et al., 2014; 2018).

Subsequent deformations (D2b) possibly took place in the mechanically-weak shear zone. Although the specific *P-T* conditions of D2b stage cannot be constrained, matrix2b has similar mineralogy as matrix2a (Camp + Ky + Oam + Bt) in Botoon where development of matrix2b is still weak. Hornblende in matrix 2a and 2b are also chemically identical including in Al_T, Mg# and Ti content which are often used as proxies for *P* and *T* (Fig. 1.6d-e; Garcia-Casco et al., 2008). Therefore, it is likely that D2b started at similar *P-T* condition as D2a. In Nanad matrix2b is more dominant and consist of finer-grained matrix assemblage of Bt-Qz and thin overgrowths surrounding some garnet and Ca-amphibole porphyroclasts (Fig. 1.8l–p). Both the matrix2a and 2b are further replaced by chlorite (Chl3) and muscovite (Ms3) assemblage with some grains oriented parallel to the C-plane (C2b) in sample N215-3 (Fig. 1.8l–p). The prevalence of Ms3, Chl3 and albite (Pl3) during Stage 3 suggests that these replacive minerals grew at lower *P-T* conditions within the Ms+Qz stability field, compared to the other stages (Stages 1, 2) and is likely promoted by fluid migration as the sequence was being exhumed towards lower *P-T* conditions (Figs. 1.10, 1.12). These fluids possibly utilized pre-existing foliations (S2b and C2b) as their pathways.

The *P-T* conditions constrained for the Stage 3 retrograde metamorphism (~600 °C, 8 kbar) using fluid inclusion microthermometry is the final step in the *P-T-D* history of the Dalrymple Amphibolite. Considering that the Ms+Qz-in curve of the matrix2a sample is used, its intersection

with the isochore of the fluid inclusions correspond to the maximum *P-T* of Stage 3 (Fig. 1.12a). The growth of hydrous replacement minerals may have happened at lower *T* within the Ms+Qz stability field and along the isochore line depending on the timing of the infiltration of saline fluids. Nonetheless, the location of the calculated isochore with its low d*P*/d*T* slope clearly support a clockwise *P-T* path for the Dalrymple Amphibolite (Fig. 1.12). This is consistent with the observation that actinolite, not glaucophane, replaced the hornblende both in the blocks (Camp1) and in the matrix (Camp2). The veins associated with Stage 3 (V3; Fig. 1.10e–i) suggest that this low *P* and *T* retrograde metamorphism and deformation event (Stage 3, D3) postdating peak metamorphic conditions are likely related to the exhumation of the metamorphic sole together with the ophiolite. Similar clockwise *P-T* path and deformation sequences have been reported from the Semail ophiolite (e.g. Soret et al., 2017).

1.6.2 The Dalrymple Amphibolite: slab-mantle wedge interface of an infant arc

Different models have been invoked to explain the higher *T/P* gradients in the slab-mantle wedge interface during incipient subduction compared to mature arcs. These warmer conditions are typically recorded in metamorphic soles with their inverted thermal gradients. Current models to explain these characteristics of metamorphic soles are as follows: 1. Sequential underplating of rocks metamorphosed at different grades and different times being juxtaposed together to result in an apparent inverted temperature gradient (e.g. Wakabayashi, 2017); 2. Post metamorphic flattening and lateral attenuation resulting to a condensed metamorphic gradient (e.g. Cowan et al., 2014); 3. Shear heating producing high-grade tectonites in major shear zones documented in the Tsiknias Ophiolite, Greece (Lamont et al., 2020); 4. Flow of hotter asthenospheric mantle during forearc rifting; and 5. The thermal conduction between a warm overriding mantle and the uppermost section of the subducting slab (e.g. Hacker 1990; Agard et al., 2018).

Radiometric dating of plagiogranites associated with the Palawan Ophiolite reveals an Early Oligocene (~34.1 Ma; Encarnacion et al., 1995) to Late Eocene age (~40.01 Ma; Dycoco et al., 2021). This is similar to the reported cooling age of the Dalrymple Amphibolite from Ar-Ar dating of amphibole and mica separates (~34.2 Ma; Encarnacion et al., 1995). The synchronous age of the

ophiolite and Dalrymple Amphibolite, the comparable peak *P-T* conditions preserved in different blocks and matrix units, and its block-in-matrix occurrence are distinct from typical metamorphic soles which generally consist of relatively intact sheets recording inverted thermal gradient (van Hinsbergen et al., 2015). Such distinct characteristics rule out sequential underplating of diachronously metamorphosed units and post-metamorphic flattening and lateral attenuation for the Dalrymple Amphibolite. Shear heating has been invoked to explain the high *T/P* preserved in the metamorphic sole of the Tsiknias Ophiolite whose cooling age is ~90 Myr younger than the overlying ophiolite (Lamont et al., 2020). In contrast to the Tsiknias Ophiolite, the similar age of the Palawan Ophiolite and Dalrymple Amphibolite supports a spreading center-turned-subduction zone model similar to the Semail Ophiolite (e.g. Rioux et al., 2016). The extensive block-in-matrix structure of the Dalrymple Amphibolite furthermore indicates that deformation was likely not restricted in a single shear zone between the subducting slab and the hanging wall as in the Tsiknias Ophiolite (Lamont et al., 2020). The thermal conduction model wherein the heat from the young and hot overlying mantle, possibly coupled by upwelling asthesnospheric mantle during forearc rifting, may have caused the metamorphism of the slab-mantle wedge interface now preserved as the Dalrymple Amphibolite.

Compared to a developed subduction zone, the residual heat of the overlying mantle peridotites during early subduction is significantly warmer (Hacker, 1990; Agard et al., 2018). This heat bakes the crustal lithologies of the subducting slab and prevent the stabilization of serpentine in the overlying mantle. Deformation in incipient subduction is accommodated by weaker lithologies, i.e. sediments (e.g. Agard et al., 2016). Unlike most metamorphic soles however, the *P-T-D* history of the Dalrymple Amphibolite reflects the petrological characteristics of a cooler slab-mantle wedge interface (Fig. 1.12a). Due to its close association with the ultramafic section of the Palawan Ophiolite and its limited exposure, the Dalrymple Amphibolite has been regarded as a typical metamorphic sole formed during the first million year of subduction initiation (Encarnacion et al., 1995; Keenan et al., 2016). The comprehensive investigation on the *P-T-D* history of its lithologies in this study suggest key differences with typical metamorphic soles.

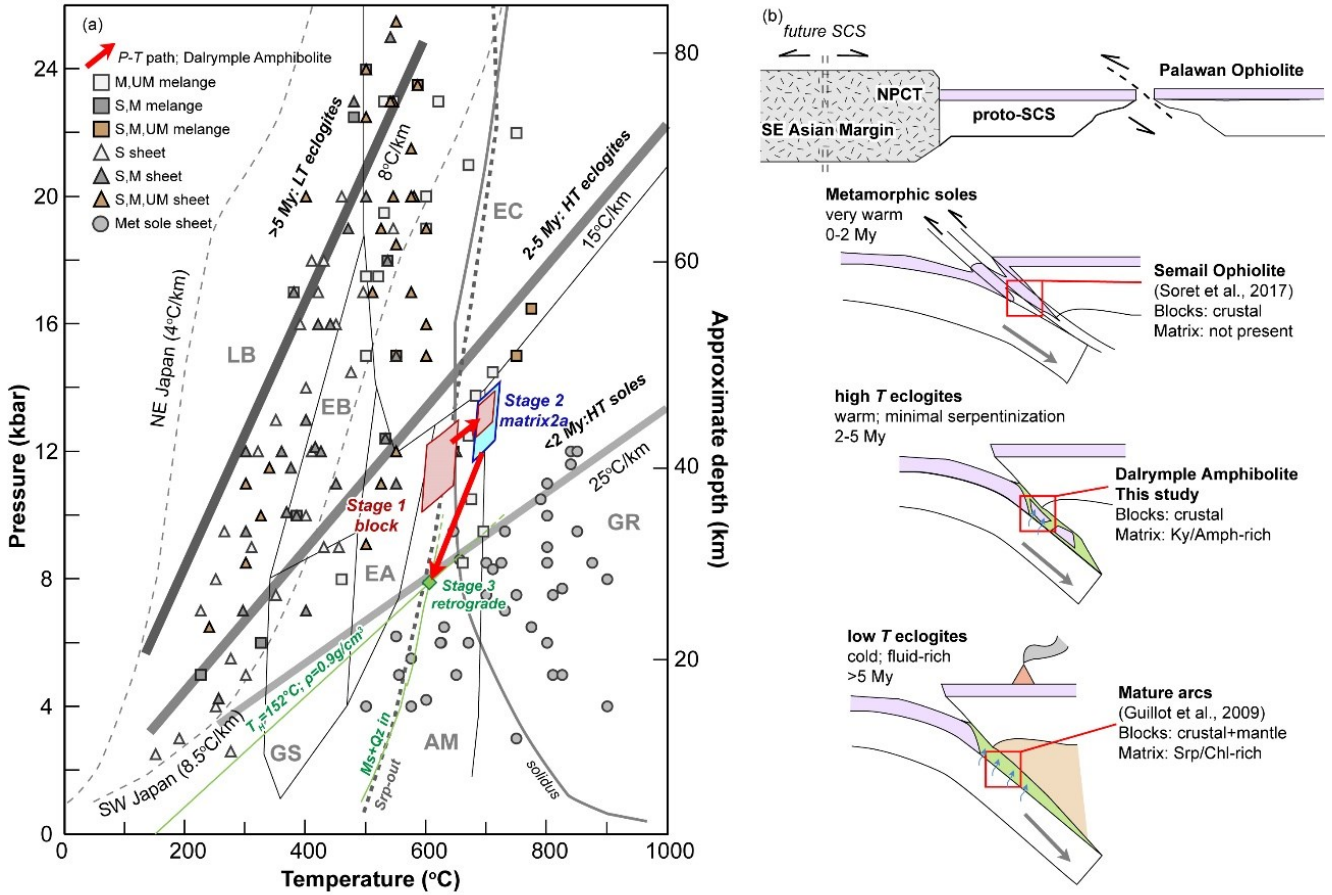

Fig. 1.12. a) *P-T* estimates for the Grt amphibolite block (Stage 1) and matrix2a (Stage2). The green diamond corresponds to the intersection of the isochore of the Stage 3 fluid inclusions and the calculated Ms+Qz-in curve for the matrix2a. Geothermal gradients of hot (SW Japan) and cold (NE Japan) subduction zones are from Peacock and Wang (1999). Metamorphic facies are from Guillot et al. (2009): LB-lawsonite blueschist, EB-epidote blueschist, EC-eclogite, GS-greenschist, EA-epidote amphibolite, AM-amphibolite, GR-granulite. Srp-out curve is from Ulmer and Trommsdorff (1995). Compilation of *P-T* conditions of metamorphic soles (met sole sheet) are from Agard et al. (2016) and other slab-mantle wedge interface lithologies (sheets and mélanges) are from Agard et al. (2018). The rock types that comprise each deposit are labelled M-mafic, UM-ultramafic, S-sedimentary. b) Schematic representation of the subduction initiation of the proto-South China Sea (SCS) promoted by the rifting of the North Palawan Continental Terrane (NPCT) from the southeast (SE) Asian Margin in the Eocene. The cooler paleogeothermal gradient preserved in the Dalrymple Amphibolite and its mélange occurrence resemble the transitional stage of subduction zones compared to metamorphic soles (e.g. Semail; Soret et al., 2017) and mature arcs (e.g. Guillot et al., 2009) as discussed in Agard et al. (2018). Blue arrows correspond to fluids released from the slab.

The peak *T* obtained for the block and matrix by Zr-in-rutile geothermometery are generally comparable to that obtained by conventional geothermometers for the Dalrymple Amphibolite (cf. Encarnacion et al., 1995). These values are lower than the peak *T* of other ophiolites (e.g. Semail ophiolite; Soret et al., 2017). The peak *P* values are however significantly higher than other metamorphic soles (e.g. Semail ophiolite; Figs.1.9; 1.12a). The paleogeothermal gradient preserved in the Dalrymple Amphibolite (~16 °C/km) and its block-in-matrix structure are atypical of metamorphic soles but are also warmer than a developed subduction channel underlying a mature arc (Fig. 1.12a). This intermediate gradient preserved in the Dalrymple Amphibolite and its block-in-matrix occurrence are more comparable to early subduction high *T* mélanges or the high *T* eclogites of Agard et al. (2018). This suggest that the Dalrymple Amphibolite may correspond to the slab-mantle wedge interface of a young subduction complex already transitioning from the much warmer conditions when subduction was first initiated. Compared to metamorphic soles which are interpreted to have formed within 2 Myr from subduction initiation (e.g. Soret et al., 2017), the cooler conditions of this transitional period may be reached within 2–5 Myr (Agard et al., 2018). We can therefore use the characteristics of this mélange complex, that is the Dalrymple Amphibolite, to investigate the petrological characteristics of the slab-mantle wedge interface in transition from its incipient stages into a mature subduction zone. Other intraoceanic arc settings with similar geothermal gradients (e.g. hot subduction zones) may also exhibit similar petrological characteristics.

1.6.3 Insights on the nature of the slab-mantle wedge interface of arcs with intermediate *P/T* gradient

The slab-mantle wedge interface of a cold mature subduction zone is typically composed of juxtaposed blocks which preserve highly variable peak metamorphic *P-T* conditions, i.e. blueschists and eclogites (Fig. 1.12a; Guillot et al., 2009). These are attributed to the flow of blocks from different depths along the subduction channel (e.g. Gerya et al., 2002; Guillot et al., 2009). This flow is thought to be enabled by the soft and mechanically weak matrix surrounding the blocks typically dominated by phyllosilicates (e.g. chlorite and serpentine). One notable characteristic of the matrix surrounding the Dalrymple Amphibolite blocks is the predominance of Ca-amphibole and kyanite

(e.g. Fig. 1.8). The strength of these minerals are thought to increase the mechanical strength of the matrix and to impede flow of materials along the subduction channel (Penniston-Dorland et al., 2018). Considering that the weaker matrix started forming before the complex reached peak metamorphic conditions, the relatively narrow range of peak *P-T* conditions preserved in the blocks (~600–720 °C; 10–13 kbar) supports this limited flow and the viscous nature of this matrix. Thermodynamic modelling also predicts the prevalence of Ca-amphibole over weaker minerals (e.g. chlorite) in the Stage 2 matrix beyond ~550 °C (Fig. 1.10c).

Processes that lead to the hybrid composition of the matrix in slab-mantle wedge interface mélanges subsequently control the chemistry of arc magmas (e.g. Marschall and Schumacher, 2012). Although the petrogenesis of the matrix in the Dalrymple Amphibolite is investigated in more detail using whole-rock data in Part 2, the chemistry of constituent minerals already provides insights into processes that are possibly at work in this slab-mantle wedge interface. Rutile, a sink for trace elements in the subducting slab, can be used to distinguish the mafic (Cr-rich) and pelitic (Nb-rich) character of a metamorphic rock's protolith (e.g. Meinhold et al., 2008). Rutile in the metamafic blocks from Dalrymple generally fall in the metamafic field (Fig. 1.6m) while the very high Nb content of those in the Ep-Bt-Ms schist block sample 215-7 fall well into the metapelite field (Fig. 1.6n). The metamafic block B214-21 from Botoon exhibits interesting Nb content variability tied to its mode of occurrence. Rutile grains in the garnet core have low Nb content (Rt1a = 175–266 ppm) and fall into the metamafic field (Fig. 1.6). In contrast, those included in garnet mantle and rim and rutile grains in the matrix and included in Camp (Rt1b) have significantly higher Nb content and falls in the metapelite field along with the matrix2a samples (Fig. 1.6n, B214-2G and B214-14).

Nb and Cr contents of rutile do not show any correlation with increasing Zr concentration (i.e. increasing *T*). We interpret the variations in the Nb-Cr contents of rutile in the blocks and matrix (Fig. 1.6m, n) as reflective of the mixing (in a broad sense) of crustal components, i.e. mafic basalts and sediments, during the development of this mélange complex. More detailed investigation of the geochemical characteristics of the matrix is needed to discriminate between the processes which may have controlled its bulk composition, i.e. mechanical mixing, fluid/melt induced advective mixing

and diffusion (Marschall and Schumacher, 2012). We therefore only argue that the Nb-Cr variations in the rutile grains indicate the variable involvement of the mafic basalt and sedimentary components. More importantly, the chemical change in rutile inclusions at the garnet mantle and rim with respect to those at the garnet core suggests that such processes started prior to the blocks reaching peak metamorphic conditions (Fig. 1.6m). This is consistent with the *P-T-D* history of the surrounding matrix 2a outlined in the previous section.

The involvement of mantle-derived components during this mixing process is less apparent in the Dalrymple Amphibolite. The high *T* condition maintained during the deformation history of the block-in-matrix complex is beyond the serpentine-stability field (Fig. 1.12a) and the scarce fluid supply at greater depths during incipient subduction due to early devolatilization at shallower regions (e.g. Agard et al., 2018) likely prevented the formation of serpentine. Orthoamphibole-rich blocks in Botoon and the chemical characteristics of some constituent minerals in the matrix2a sample B214-29 however suggest the involvement of mantle components. Kyanite (Cr_2O_3 = 0.71–2.17 wt.%) in B214-29 are relatively Cr-rich while Ca-amphibole grains are both Mg- and Cr-rich (Mg# = 0.72–0.78; Cr_2O_3 = 0.12–1.3 wt.%). Some rutile grains N215-3 also has high Cr_2O_3 content (= 0.16–1.93 wt.%).

The presence of fluids in this shear zone throughout its history is also apparent from the multiple generation of veins cross-cutting the block-in-matrix complex. The earlier stage fluids appear to be in equilibrium with the blocks (i.e. internally sourced; cf. Locatelli et al., 2019) as suggested by the absence of any reaction zone between the vein and the block (e.g. Qz-Ky vein, Figs. 1.2h, 1.5a). Monomineralic epidote veins possibly represent Ca-rich fluids. The Qz-Ky veins in particular are interesting since they suggest either a change in the behavior of some immobile elements like Al in this environment similar to what has been described for orogenic belts (e.g. Alpe Sponda, Central Alps; Beitter et al., 2008), or the extreme leaching of the other components which left behind relatively immobile elements. The latter is apparently favored by the occurrence of ilmenite-kyanite accumulations in some sections of matrix2a in Botoon (B214-10; Fig. 1.8d).

Evidence for migration of externally-derived fluids is also preserved in the latest stage (Stage 3). Microthermometry of fluid inclusions related to the replacement of kyanite by muscovite reveals the involvement of saline fluids (1.8–6.9 wt.% NaCl equivalent; Fig. 1.10d). Such aqueous fluids with relatively low salinity dominate the shallow regions (< 80 km) of the subduction zone (e.g. Kawamoto et al., 2013; Manning and Frezzotti, 2020). In D113-1, the quartz vein is linked to the replacement of hornblende by actinolite. Compositional maps and line analysis reveal replacive actinolite with progressively higher Si, Ca and Mg# and lower Al, Na and K towards the vein (Fig. 1.10f, g). The degree of hornblende replacement by actinolite also increases towards the vein. Farther from the vein, actinolite formation is limited along grain boundaries which maps out the pathway of the percolating fluids (Fig. 1.10h, i). These greenschist-facies fluids were likely derived from the lower-grade lithologies underthrusted below the ophiolite during its exhumation. These observations in the Dalrymple Amphibolite highlight the importance of fluids in element mobility and material transfer through the slab-mantle wedge interface from initiation to its exhumation. Future studies on the chemical signatures of these different generations of fluids may provide further insights on the nature of fluids and fluid-rock interaction along the slab-mantle wedge interface.

1.6.4 Tectonic implications on the NPCT

The Late Eocene Palawan Ophiolite exposed in central Palawan is argued to have formed as a back-arc basin hosted within the Cretaceous proto-South China Sea (SCS) Plate (Labis et al., 2020; Dycoco et al., 2021). In the Eocene, rifting in the Southeast Asian margin was initiated and the NPCT started drifting toward the southeast (e.g. Yumul et al., 2003; Cao et al., 2020). The shift from a tensional regime to compressional, forced the initiation of subduction at/or near the spreading center of this Eocene proto-SCS (Fig. 1.12b; Keenan et al., 2016). This convergence resulted in an intraoceanic arc. Slivers of this arc were then emplaced during its collision with the NPCT as the Palawan Ophiolite.

The degree to which subduction proceeded in this intraoceanic arc before the underplating of the NPCT and subsequently the emplacement of the ophiolite is largely unknown. The volcanic section of the ophiolite only records its mid-oceanic ridge history (e.g. Keenan et al., 2016; Gibaga

et al., 2020) and products of arc magmatism is undetected. Earlier models linked a small volume of calc-alkaline lavas (~17 Ma) in the Cagayan de Sulu ridge to the Eocene subduction initiation (Encarnacion et al., 1995) but the connection remain contentious (e.g. Dycoco et al., 2021).

The *P-T-D* evolution of the Dalrymple Amphibolite outlined here however, suggests that subduction along this plate interface did progress, enough to shift its *P-T* gradients towards cooler conditions (Fig. 1.12a; cf. Agard et al., 2020). Based on the compilation study of Agard et al. (2018), such conditions (~16 °C/km) are usually reached around 2–5 Myr since subduction is initiated (Fig. 1.12b). In contrast, the hot thermal gradients of metamorphic soles are thought to dominate the first ~2 Ma since subduction is first initiated. Radiometric dating of the peak metamorphism of the metamafic blocks and the surrounding matrix in the future can further constrain the duration of subduction in the Palawan Ophiolite. Exhumation of the ophiolite with the Dalrymple amphibolite at its base is linked with the complete consumption of the oceanic lithosphere at the leading edge of the NPCT and continental material underplating beneath the arc.

References

Agard, P., Prigent, C., Soret, M., Dubacq, B., Guillot, S., Deldicque, D., 2020. Slabitization: mechanism controlling subduction development and viscous coupling. Earth-Science Reviews 28, 1–28.

Agard, P., Plunder, A., Angiboust, S., Bonnet, G., Ruh, J., 2018. The subduction plate interface: rock record and mechanical coupling (from long to short timescales). Lithos 320–321, 537–566.

Agard, P., Yamato, P., Soret, M., Pringent, C., Guillot, S., Plunder, A., Dubacq, B., Chauvet, A., Monie, P., 2016. Plate interface rheological switches during subduction infancy: Control on slab penetration and metamorphic sole formation. Earth and Planetary Science Letters 451, 208–220.

Angel, R.J., Mazzuccheli, M.L., Alvaro, M., Nestola, F., 2017a. EoSFit-Pinc: A simple GUI for host-inclusion elastic thermobarometry. American Mineralogist 102, 1957–1960.

Angel, R.J., Alvaro, M., Miletich, R., Nestola, F., 2017b. A simple and generalized *P-T-V* EoS for continuous phase transitions, implemented in EosFit and applied to quartz. Contributions to Mineralogy and Petrology 29, 1–15.

Aurelio, M.A., Forbes, M., Taguibao, K.J.L., Savella, R., Bacud, J., Franke, D., Pubellier, M., Savva, D., Meresse, F., Steuer, S., Carranza, C.D., 2014. Middle to Late Cenozoic tectonic events in south and central Palawan (Philippines) and their implications to the evolution of the southeastern margin of South China Sea: Evidence from onshore structural and offshore seismic data. Marine and Petroleum Geology 58, 658–673.

Bebout, G.E., 2013. Metasomatism in subduction zones of subduction zones of subducted oceanic slabs, mantle wedges, and the slab-mantle interface *In*: Harlov, D.E., Austrheim, H. Metasomatism (eds.) Metasomatism and the chemical transformation of rock. Lecture notes in Earth system sciences, Springer-Verlag Berlin Heidelberg, 289–349.

Bebout, G.E., Barton, M.D., 2002. Tectonic and metasomatic mixing in a High-*T*, subduction-zone melange – insights into the geochemical evolution of the slab-mantle interface. Chemical Geology 187, 79–106.

Bebout, G.E., Penniston-Dorland, S.C., 2016. Fluid and mass transfer at subduction interfaces-The field metamorphic record. Lithos 240–243, 228–258.

Beitter, T., Wagner, T., Marki, G., 2008. Formation of kyanite-quartz veins of the Alpe Sponda, Central Alps, Switzerland: Implications for Al transport during regional metamorphism. Contributions to Mineralogy and Petrology 156, 689–707.

Bodnar, R.J., 1993. Revised equation and table for determining the freezing point depression of H_2O-NaCl solutions. Geochimica et Cosmochimica Acta 57, 683–684.

Cao, L., Shao, L., Qiao, P., Cui, Y., Zhang, G., Zhang, X., 2020. Formation and paleogeographic evolution of the Palawan continental terrane along the Southeast Asian margin revealed by detrital fingerprints. The Geological Society of America Bulletin 133, 1167–1193.

Codillo, E.A., Le Roux, V., Marschall, H.R., 2018. Arc-like magmas generated by melange-peridotite interaction in the mantle wedge. Nature Communications 9, 1–11.

Cowan, R.J., Searle, M.P., Waters, D.J., 2014. Structure of the metamorphic sole to the Oman Ophiolite, Sumeini Window and Wadi Tayyin; Implications for ophiolite obduction processes. Geological Society, London, Special Publications 392, 155–175.

De Capitani, C., Brown, T.H., 1987. The computation of chemical equilibrium in complex systems containing non-ideal solutions. Geochimica et Cosmochimica Acta 51, 2639–2652.

De Capitani, C., Petrakakis, K., 2010. The computation of equilibrium assemblage diagrams with Theriak/Domino software. American Mineralogist 95, 1006–1016.

Dilek, Y., Furnes, H., 2014. Ophiolites and their origins. Elements 10, 93–100.

Dycoco, J.M.A., Payot, B.D., Valera, G.T.V., Labis, F.A.C., Pasco, J.A., Perez, A.d.C., Tani, K., 2021. Juxtaposition of Cenozoic and Mesozoic ophiolites in Palawan island, Philippines: New insights on the evolution of the Proto-South China Sea. Tectonophysics 819. 229085.

Droop, G.T.R., 1987. A general equation for estimating Fe^{3+} concentrations in ferromagnesian silicates and oxides from microprobe analyses, using stoichiometric criteria. Mineralogical Magazine 51, 431–435.

Encarnacion, J.P., Essene, E.J., Mukasa, S.B., Hall, C.H., 1995. High-pressure and -temperature subophiolitic kyanite-garnet amphibolites generated during initiation of Mid-Tertiary subduction, Palawan, Philippines. Journal of Petrology 36, 1481–1503.

Garcia-Casco, A., Lazaro, C., Rojas-Agramonte, Y., Kröner, A., Res-Roldan, R.L.T., Nuñez, K., Neubauer, F., Millan, G., Blanco-Quintero, I., 2008. Partial melting and counterclockwise *P-T* path of subducted oceanic crust (Sierra del Colvento Mélange, Cuba). Journal of Petrology 49, 129–161.

Gerya T., Stöckhert, B., Perchuk, A.L., 2002. Exhumation of high-presure metamorphic rocks in a subduction channel: A numerical simulation. Tectonics 21, 1–15.

Gibaga, C.R.L., Arcilla, C.A., Hoang, N., 2020. Volcanic rocks from the Central and Southern Palawan Ophiolites, Philippines: Tectonic and mantle heterogeneity constraints. Journal of Asian Earth Sciences: X, 1–17. DOI: 10.1016/j.jaesx.2020.100038.

Gilgen, S., Diamond, L.W., Mercolli, I., 2016. Sub-seafloor epidosite alteration: Timing, depth and stratigraphic distribution in the Semail Ophiolite, Oman. Lithos 260, 191–210.

Green, E.C.R., White, R.W., Diener, J.F.A., Powell, R., Holland, T.J.B., Palin, R.M., 2016. Activity-composition relations for the calculation of partial melting equilibria in metabasic rocks. Journal of Metamorphic Geology 34, 845–869.

Grove, M., Bebout, G.E., 1995. Cretaceous tectonic evolution of coastal southern California: Insights from the Catalina Schist, Tectonics 14, 1290–1308.

Guillot, S., Hattori, K., Agard, P., Schwartz, S., Vidal, O., 2009. Exhumation processes in oceanic and continental subduction contexts: A review *In*: Lallemand, S., Funiciello, F. (eds.) Subduction zone geodynamics. Springer-Verlag Berlin Heidelberg, 175–205.

Hacker, B.R., 1990. Simulation of the metamorphic and deformational history of the metamorphic sole of the Oman ophiolite. Journal of Geophysical Research 95, 4895–4907.

Holland, T.J.B., Powell, R., 2011. An improved and extended internally consistent thermodynamic dataset for phases of petrological interest, involving a new equation of state for solids. Journal of Metamorphic Geology 29, 333–383.

Jagoutz, O., Behn, M.D., 2013. Foundering of lower island-arc crust as an explanation for the origin of the continental Moho. Nature 504, 131–134.

Jørgensen, T.R.C., Tinkham, D.K., Lesher, C.M., 2019. Low-*P* and high-*T* metamorphism of basalts: Insights from the Sudbury impact melt sheet aureole and thermodynamic modelling. Journal of Metamorphic Geology 37, 271–313.

Kapp, P., Manning, C.E., Tropper, P., 2009. Phase-equilibrium constraints on titanite and rutile activities in mafic epidote amphibolites and geobarometry using titanite-rutile equilibria. Journal of Metamorphic Geology 27, 509–521.

Kawamoto, T., Yoshikawa, M., Kumagai, Y., Mirabueno, H.T., Okuno, M., Kobayashi, T., 2013. Mantle wedge infiltrated with saline fluids from dehydration and decarbonation of subducting slab. Proceedings of the National Academy of Sciences 110, 9663–9668.

Keenan, T.E., Encarnacion, J., Buchwaldt, R., Fernandez, D., Mattinson, J., Rasoazanamparany, C., Leutkemeyer, P.B., 2016. Rapid conversion of an oceanic spreading center to a subduction zone inferred from high-precision geochronology. Proceedings of the National Academy of Sciences 113, E7359–E7366.

Kohn, M.J., Spear, F.S., 1990. Two new geobarometers for garnet amphibolites, with applications to southeastern Vermont. American Mineralogist 75, 89–96.

Labis, F.A.C., Payot, B.D., Valera, G.T.V., Pasco, J.A., Dycoco, J.M.A., Tamura, A., Morishita, T., Arai, S., 2020. Melt-rock interaction in the subarc mantle: records from the plagioclase peridotites of the southern Palawan Ophiolite, Philippines. International Geology Review 63, 1067–1089.

Lamont, T.N., Roberts, N.M.W., Searle, M.P., Gopon, P., Waters, D.J., Millar, I., 2020. The age, origin and emplacement of the Tsiknias Ophiolite, Tinos, Greece, Tectonics, 39, 1–45.

Leake, B.E., Woolley, A.R., Arps, C.E.S., Birch, W.D., Gilbert, M.C., Grice, J.D., Hawthorne, F.C., Kato, A., Kisch, H.J., Krivovichev, V., Linthout, K., Laird, J., Mandarino, J.A., Maresch, W.V., Nickel, E.H., Rock, N.M.S., Schumacher, J.C., Smith, D.C., Stephenson, N.C.N., Ungaretti, L., Whittaker, E.J.W., Youzhi, G., 1997. Nomenclature of amphiboles: Report of the subcommittee on amphiboles of the international mineralogical association, commission on new minerals and mineral names. The Canadian Mineralogist 35, 219–246.

Locatelli, M., Verlaguet, A., Agard, P., Pettke, T., Federico, L., 2019. Fluid pulses during stepwise brecciation at intermediate subduction depths (Monviso Eclogites, W. Alps): First internally then externally sourced. Geochemistry, Geophysics, Geosystems 20, 5285–5318.

Manning, C.E., Frezzotti, M.L., 2020. Subduction-zone fluids. Elements 16, 395–400.

Marschall, H.R., Schumacher, J.C., 2012. Arc magmas sourced from melange diapirs in subduction zones. Nature Geoscience 5, 862–867.

Meinhold, G., Anders, B., Kostopoulos, D., Reischmann, T., 2008. Rutile chemistry and thermometry as provenance indicator: An example from Chios Island, Greece. Sedimentary Geology 203, 98–111.

Muller, C., 1991. Biostratigraphy and geological evolution of the Sulu sea and surrounding area. *In*: Silver, E.A., Rangin, C., von Breymann, M.T. et al. Proceedings of the Ocean Drilling Program Scientific Results 124, College Station, Texas, 121–131.

Padrones, J.T., Tani, K., Tsutsumi, Y., Imai, A., 2017. Imprints of Late Mesozoic tectono-magmatic events on Palawan Continental Block in northern Palawan, Philippines. Journal of Asian Earth Sciences 142, 56–76.

Peacock, S., Wang, K., 1999. Seismic consequences of warm versus cool subduction metamorphism: Examples from Southwest and Northeast Japan. Science 286, 937–939.

Penniston-Dorland, S.C., Kohn, M.J., Piccoli, P.M., 2018. A melange of subduction temperatures: Evidence from Zr-in-rutile thermometry for strengthening of the subduction interface. Earth and Planetary Science Letters 482, 525–535.

Picazo, S.N., Ewing, T.A., Müntener, O., 2019. Paleocene metamorphism along the Pennine-Austroalpine suture constrained by U-Pb dating of titanite and rutile (Malenco, Alps). Swiss Journal of Geosciences 112, 517–542.

Rangin, C., Silver, E.A., 1991. Neogene tectonic evolution of the Celebes-Sulu basins: New insights from Leg 124 Drilling. Proceedings of the Ocean Drilling Program. Scientific Results 124, 51–63.

Raschka, H., Nacario, E., Rammlair, D., Samonte, C., Steiner, L., 1985. Geology of the ophiolite of central Palawan island, Philippines. Ofioliti 10, 375–390.

Rioux, M., Garber, J., Bauer, A., Bowring, S., Searle, M., Kelemen, P., Hacker, B., 2016. Synchronous formation of the metamorphic sole and igneous crust of the Semail ophiolite: New constraints on the tectonic evolution during ophiolite formation from high-precision U-Pb zircon geochronology. Earth and Planetary Science Letters 451, 185–195.

Schmidt, C., Ziemann, M.A., 2000. In-situ Raman spectroscopy of quartz: A pressure sensor for hydrothermal diamond-anvil cell experiments at elevated temperatures. American Mineralogist 85, 1725–1734.

Schumacher, J.C., 1991. Empirical ferric iron corrections: necessity, assumptions and effects on selected geothermobarometers. Mineralogical Magazine 55, 3–18.

Seyfried, W.E., Berndt, M.E., Seewald, J.S., 1988. Hydrothermal alteration processes at mid-ocean ridges: Constraints from diabase alteration experiments, hot-spring fluids and composition of the oceanic crust. Canadian Mineralogist 26, 787–804.

Soret, M., Agard, P., Dubacq, B., Plunder, A., Yamato, P., 2017. Petrological evidence for stepwise accretion of metamorphic soles during subduction infancy (Semail ophiolite, Oman and UAE). Journal of Metamorphic Geology 35, 1051–1080.

Starr, P.G., Pattison, D.R.M., 2019. Metamorphic devolatilization of basalts across the greenschist-amphibolite facies transition zone: Insights from isograd mapping, petrography and thermodynamic modelling. Lithos 342–343, 295–314.

Steele-MacInnis, M., Lecumberri-Sanchez, P., Bodnar, R.J., 2012. HOKIEFLINCS_H2O-NACL: A Microsoft Excel spreadsheet for interpreting microthermometric data from fluid inclusions based on the PVTX properties of H_2O-NaCl. Computers & Geosciences 49, 334–337.

Suzuki, K., Kawakami, T., 2019. Metamorphic pressure-temperature conditions of the Lützow-Holm Complex of East Antarctica deduced from Zr-in-rutile geothermometer and Al_2SiO_5 minerals enclosed in garnet. Journal of Mineralogical and Petrological Sciences 114, 267–279.

Thomas, J.B., Spear, F.S., 2018. Experimental study of quartz inclusions in garnet at pressures up to 3.0 GPa: evaluating validity of the quartz-in-garnet inclusion elastic thermobarometer. Contributions to Mineralogy and Petrology 42, 1–14.

Tomkins, H. S., Powell, R., Ellis, D. J., 2007. The pressure dependence of the zirconium-in-rutile thermometer. Journal of Metamorphic Geology 25, 703–713.

Ulmer, P., Trommsdorff, V., 1995. Serpentine stability to mantle depths and subduction-related magmatism. Science 268, 858–861.

van Hinsbergen, D.J.J, Peters, K., Maffione, M., Spakman, W., Guilmette, C., Thieulot, C., Plümper, O., Gürer, D., Brouwer, F.M., Aldanmaz, E., Kaymackci, N., 2015. Dynamics of intraoceanic subduction initiation: 2. Suprasubduction zone ophiolite formation and metamorphic sole exhumation in context of absolute plate motions. Geochemistry, Geophysics, Geosystems 16, 1771–1785.

Vielzeuf, D., Schmidt, M.W., 2001. Melting relations in hydrous systems revisited: Application to metapelites, metagreywackes and metabasalts. Contributions to Mineralogy and Petrology 141, 251–267.

Wakabayashi, J., 2017. Structural context and variation of ocean plate stratigraphy, Franciscan Complex, California: Insight into mélange origins and subduction-accretion processes. Progress in Earth and Planetary Science 4, 1–23.

Wei, C.J., Duan, Z.Z., 2018. Phase relations in metabasic rocks: Constraints from the results of experiments, phase modelling and ACF analysis. *In*: Zhang, L.F., Zhang, Z., Schertl, H.-P., Wei, C. (eds.) HP-UHP Metamorphism and tectonic evolution of orogenic belts. Geological Society, London, Special Publications 474, 1–21.

Whitney, D.L., Evans, B.W., 2010. Abbreviations for names of rock-forming minerals. American Mineralogist 95, 185–187.

Yumul, G.P.Jr., Dimalanta, C.B., Tamayo, R.A.Jr., Maury, R.C., 2003. Collision, subduction and accretion events in the Philippines: A synthesis. The Island Arc 12, 77–91.

Zack, T., Moraes, R., Kronz, A., 2004. Temperature dependence of Zr in rutile: Empirical calibration of a rutile thermometer. Contributions to Mineralogy and Petrology 148, 471–488.

Part 2. Mixing, fluid Infiltration, Leaching and Deformation (MILD) proesses along the slab-mantle wedge interface at high *T* and *P* conditions: Records from the Dalrymple Amphibolite, Philippines

2.1 Introduction

The slab-mantle wedge interface separates the subducting oceanic lithosphere from the overlying mantle wedge in subduction zones. This region, also referred to as the subduction channel (e.g. Guillot et al., 2009; Bebout and Penniston-Dorland, 2016) or subduction plate interface (e.g. Agard et al., 2018), serves as the locus of interaction between crustal and mantle lithologies, and where mafic and sedimentary components from the subducting slab are recycled for utilization in the subduction factory (e.g. Tatsumi, 2005). Thought to represent paleo slab-mantle wedge interfaces, high-pressure mélange zones provide a picture of fluid-rich shear zones of tens to hundred meters-wide, composed of metamafic, metasedimentary, and metaultramafic blocks surrounded by a matrix of hybridized composition (e.g. Bebout and Penniston-Dorland, 2016). These deformation zones also serve as pathways for migrating fluids derived from the dehydrating slab. Whole-rock geochemical data from arc lavas and experimental analyses suggest the important role that this interface plays in controlling the overall arc magma chemistry (e.g. Nielsen and Marschall, 2017; Codillo et al., 2018).

The complex interplay between deformation, mechanical mixing of end-member components (sediments, mafic crust and mantle materials), and fluid advection are reflected in the highly variable phase assemblage and whole-rock composition of the matrix material surrounding the blocks in different slab-mantle wedge interface exposures and even within a single locality (e.g. Dalrymple Amphibolite; Table 2.1). The juxtaposition of rocks with disparate composition for extended periods can further lead to diffusive material transfer at centimeter to meter scales among blocks and between block-matrix pairs (e.g. Bebout and Barton, 2002). Most studies on the petrological evolution of the slab-mantle wedge interface are focused on the pressure-temperature-deformation (*P-T-D*) evolution and petrogenesis of the blocks in these terranes primarily due to the relatively poorer preservation state of the softer matrix material in most localities and/or the extensive fluid flux passing through these sheared domains causing either leaching and/or retrograde overprint

(Marschall and Schumacher, 2012). The change in paleogeothermal gradient of this interface as subduction progresses is another consideration when studying these terranes (Agard et al., 2018). The petrological characteristics of the lithologies comprising the slab-mantle wedge interface during subduction initiation and in mature arcs have largely been constrained through studies of metamorphic soles beneath ophiolites and exhumed high-*P/T* type metamorphic terranes, respectively. Localities preserving the petrological characteristics of both blocks and matrix, as well as prograde to peak *P-T* conditions comparable to the slab-mantle wedge interface as it transitions from a young and hot margin to a mature arc are equally important albeit less common. One such locality with an intermediate paleogeothermal gradient is the Dalrymple Amphibolite in Palawan Island, Philippines (Valera et al., 2021; Fig. 2.1a, b).

In this study, whole-rock geochemical data of metamafic-metasedimentary blocks and sheared matrix samples are used to determine the petrogenesis of the Dalrymple Amphibolite. Major oxide and trace element contents of the metamafic blocks revealed their mid-oceanic ridge basalt (MORB) origin and genetic relation with the mafic oceanic crust of the central Palawan Ophiolite (CPO). The petrogenesis of the matrix, on the other hand, records the combined effects of mechanical mixing and multiple stages of fluid infiltration. In addition to conventional binary plots and trace element spidergrams, the compounding effects of mechanical and fluid-related processes on the matrix are distinguished by employing geostatistics (i.e. correlation coefficient) and isocon analysis. Mineral chemistry data are also utilized in this work although a more complete assessment is available in Valera et al. (2021) which used the same samples. Mineral abbreviations are after Whitney and Evans (2010) except for Ca-amphibole (Camp).

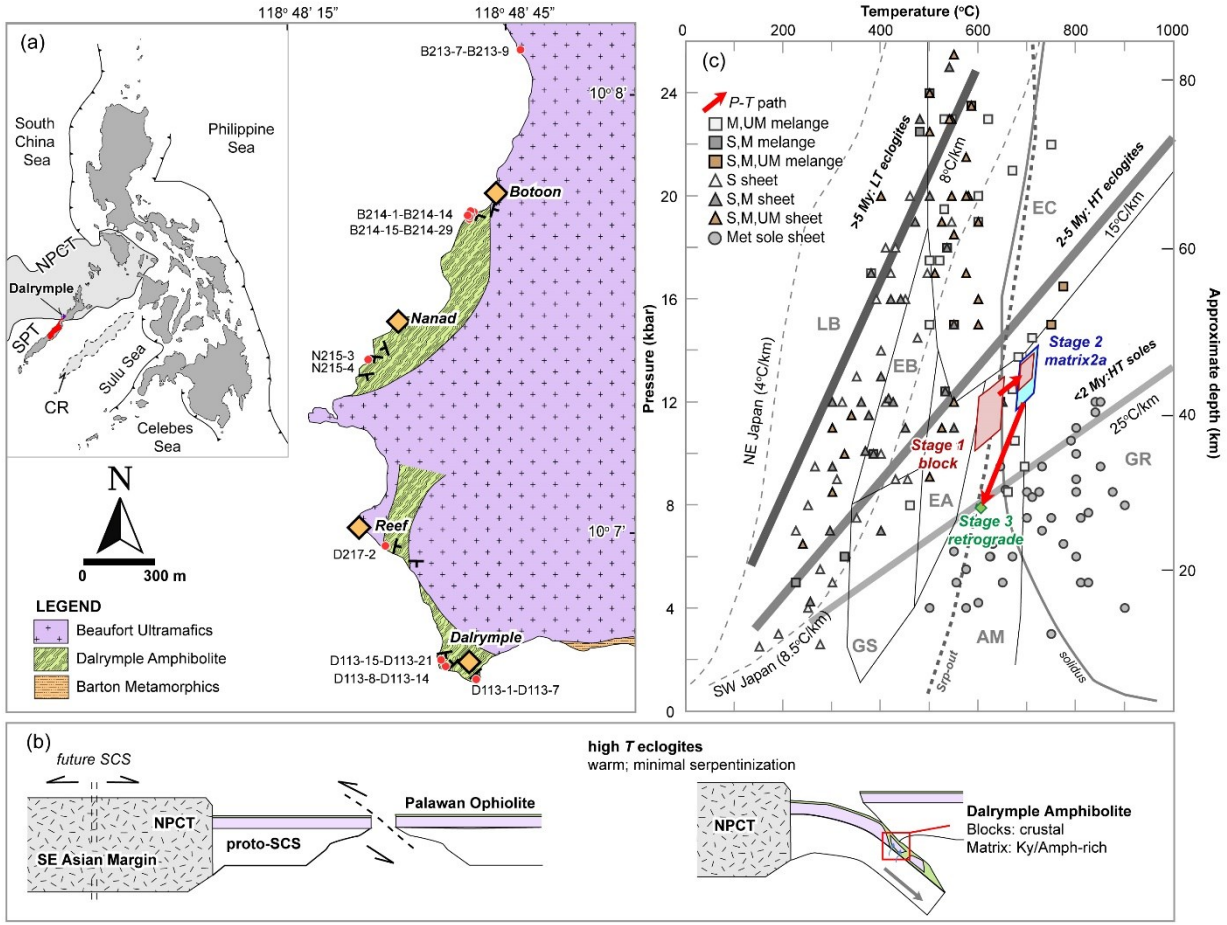

Fig. 2.1. a) Map showing the distribution of the Dalrymple Amphibolite of the central Palawan Ophiolite (red fill in inset map) in Ulugan Bay. Inset map shows tectonic map of the Philippines, the surrounding marginal basins and trenches. NPCT-North Palawan Continental Terrane, SPT-South Palawan Terrane, CR-Cagayan de Sulu Ridge. Modified from Labis et al. (2020); b) Schematic representation of the subduction initiation of the proto-South China Sea (SCS) during the opening of the South China Sea (future SCS). c) *P-T* estimates for the Grt amphibolite block (Stage 1), matrix 2a (Stage 2) and retrograde metamorphism (Stage 3) of the Dalrymple Amphibolite adopted from Valera et al. (2021). Also shown are *P-T* conditions of metamorphic soles (Met sole sheet) and other slab-mantle wedge interfaces (sheets and melanges) compiled from Agard et al. (2016) and Agard et al. (2018). M-mafic, UM-ultramafic, S-sedimentary. Metamorphic facies and solidus curve (Guillot et al., 2009): LB-lawsonite blueschist, EB-epidote blueschist, EC-eclogite, GS-greenschist, EA-epidote amphibolite, AM-amphibolite, GR-granulite. Srp-out curve is from Ulmer and Trommsdorff (1995). Geothermal gradients of hot (SW Japan) and cold (NE Japan) subduction zones are from Peacock and Wang (1999).

2.2 Geological setting

Palawan Island in western Philippines consist of tectonically juxtaposed continental and oceanic terranes. The northern segment of the island, referred to as the North Palawan Continental Terrane (NPCT), is composed of Paleozoic to Eocene flysch-type turbiditic deposits (Fig. 2.1a). This microcontinental block drifted from the Southeast Asian continental margin during the Eocene to Oligocene which led to the opening of the South China Sea (SCS) basin in its northwestern margin (Fig. 2.1b). The tectonic shortening is then thought to have induced subduction along a preexisting spreading center of the marginal basin in its southeastern margin typically referred to as the proto-South China Sea (e.g. Encarnacion et al., 1995; Yumul et al., 2020; Dycoco et al., 2021). Closing of the proto-SCS subsequently led to the collision between the NPCT and the nascent arc now exposed as the Palawan Ophiolite (Fig. 2.1b).

The Palawan Ophiolite is a Tethyan-type ophiolite exposed in central and southern segments of Palawan Island. Slivers of this fossil oceanic lithosphere comprise the South Palawan Terrane (SPT) and are thrusted on top of the NPCT lithologies. Based on systematic differences in petrological signatures and tectonic setting of formation, recent works distinguish the Late Eocene to Early Oligocene central Palawan Ophiolite (CPO) and the Cretaceous southern Palawan Ophiolite (SPO; Labis et al., 2020; Dycoco et al., 2021). The Dalrymple Amphibolite is only found at the base of the hanging wall, below the residual peridotites of the CPO (Fig. 2.1b, c).

The Dalrymple Amphibolite is a high-grade metamorphic sequence with block-in-matrix fabric. It is predominantly composed of metamafic blocks and minor metasedimentary blocks surrounded by a sheared matrix. The matrix exhibits variable mineralogy with some samples consisting of a mafic phase assemblage (e.g. Ca-amphibole + garnet + kyanite + ilmenite) and others derived from a metasedimentary protolith and are composed of kyanite + biotite + ilmenite ± garnet. Both the block and matrix record an intermediate paleogeothermal gradient with similar peak *P-T* conditions of ~700 °C and 13 kbar (Part1; Valera et al., 2021). Its block-in-matrix occurrence and cooler paleogeothermal gradients contrast with typical metamorphic soles which consist of relatively

coherent sheets with inverted thermal gradients of >20 °C/km (e.g. Soret et al., 2017). The predominance of Ca-amphibole and kyanite in the matrix of the Dalrymple Amphibolite is also distinct from other localities with cooler paleogeothermal gradients (4–10 °C/km) which are dominated by phyllosilicates such as talc, serpentine and chlorite (Fig. 2.1b; e.g. Bebout, 2013).

The mafic crust of the central Palawan Ophiolite (CPO) consists of basaltic pillow lavas, isotropic and layered gabbros and ultramafic cumulates. Petrological investigation of the mafic lavas and intrusives revealed a MORB (Gibaga et al., 2020) to transitional island arc basalt affinity (e.g. Keenan et al., 2016; Dycoco et al., 2021). Exposures of the mantle section of the ophiolite are found thrusted on top of the Dalrymple Amphibolite in Ulugan Bay (Valera et al., 2021). It is predominantly composed of moderately serpentinized interlayers of harzburgite and dunite. Late stage mafic dikes with distinct bake-and-chill margins crosscut the ophiolite sequence, from the metamorphic sole to the crustal section. The dikes exhibit similar tholeiitic basalt geochemical signature as the mafic crust of the ophiolite (Dycoco et al., 2021).

2.3 *P-T-D* history of the Dalrymple Amphibolite

The Dalrymple Amphibolite is a thin mélange complex exposed primarily in Ulugan Bay in the localities of Botoon (Fig. 2.2a–f), Nanad (Fig. 2.2g–k) and Dalrymple points. Earlier works on the Dalrymple Amphibolite considered it as a typical metamorphic sole related to the Palawan Ophiolite based on its proximity and limited occurrence. Encarnacion et al. (1995) constrained peak *T* conditions of 700–760 °C at a minimum *P* of 9 kbar and attributed the mélange-like appearance to a later, 'cold' deformation event although *P-T* estimation for this deformation event is lacking. Valera et al. (2021) reevaluated the *P-T-D* history for the Dalrymple Amphibolite by constraining the *P-T* conditions for the metamafic blocks and the surrounding matrix. This *P-T-D* history (Fig. 2.1b) is adopted here and summarized below based on Valera et al. (2021).

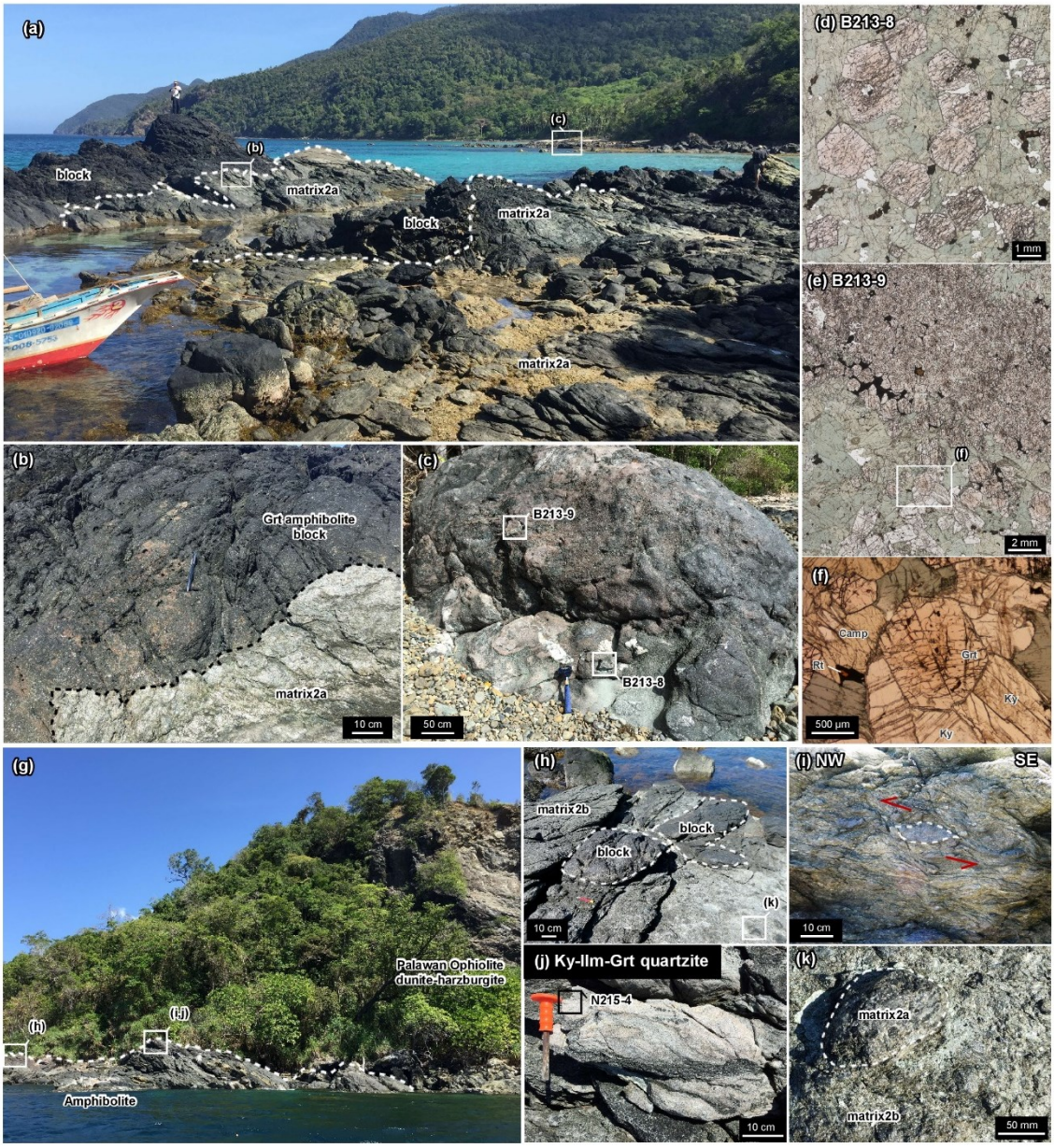

Fig. 2.2. a–f) Field photos of the exposures in Botoon and g–k) Nanad. a, b) Photos of the block-in-matrix sequence. The boundaries between the block and matrix are outlined by the dashed line. c) Block in Botoon with d) Kyanite-free core portion (B213-8) and e, f) Kyanite-bearing sample (B213-9) at the edge of the block. Photomicrographs in d-f are in plane-polarized light. g) Interlayers of dunite and harzburgite thrusted on top of the Dalrymple Amphibolite. h) The exposure in Nanad exhibits the same block-in-matrix fabric observed in Botoon but have smaller blocks with more rounded edges. i) Deformed amphibolite block indicating a top to the NW sense of shear. j) The blocks in Nanad also include earlier formed matrix2a (Fig. 2.2k) surrounded by a highly sheared matrix2b.

The Dalrymple Amphibolite is composed of metamafic and minor metasedimentary blocks surrounded by a highly sheared matrix (Fig. 2.2). The metamafic blocks are amphibolite with variable amounts of garnet (i.e. Grt amphibolite; Fig. 2.2b–f) and epidote (i.e. Ep amphibolite). Deformed metamafic blocks in Nanad indicate a top to the NW sense of shear indicating the thrusting of the ultramafic section of the ophiolite on top of the amphibolite mélange sequence (Fig. 2.2i; Valera et al., 2021). A brief description of the petrographic and mineral chemical characteristics of the blocks and matrix samples are given in the sample description section. Since the samples used in this work are the same as those described in Valera et al. (2021), the reader is referred to the previous study for a more detailed description on the petrography and mineral chemistry of the metamafic blocks and the matrix samples. The paragenesis of the block and matrix of the Dalrymple Amphibolite is summarized in Fig. 2.3 while Table 2.1 lists the phase assemblage and mode of occurrence of the samples used (Valera et al., 2021). Earlier studies on the geochemical characteristics of the metamafic blocks suggest a mid-oceanic ridge basalt protolith similar to the mafic crust of the CPO (e.g. Keenan et al., 2016; Fig. 2.1 c, d). This evidence supports the recent tectonic model of spreading center-turned-subduction zone for the CPO (e.g. Dycoco et al., 2021). According to this model, the Dalrymple Amphibolite represent the subducted equivalent of the same oceanic lithosphere now emplaced as the CPO (Fig. 2.1c, d). Compared to the metamafic blocks, no studies have been conducted on the petrogenesis of the metasedimentary blocks and the sheared matrix of the sequence. The metasedimentary blocks sampled in this study include Ep-Bt-Ms schist (D215-7), Camp-Ky-Qz schist (B214-26), Ky-Ilm-Grt quartzite (N215-4) and a metacarbonate (B214-7C).

As discussed in Part 1, the *P-T-D* history of the Dalrymple Amphibolite was subdivided into the *P-T* conditions preserved in the block (Stage 1) and the matrix (Stage 2; Fig. 2.3). The growth of replacement minerals affecting both block and matrix samples are assigned Stage 3. The Zr-in-rutile geothermometry (Tomkins et al., 2007) and quartz-in-garnet Raman geobarometry (e.g. Angel et al., 2017) applied to respective inclusions in the core and rim of garnet porphyroblasts of a Grt amphibolite block (B214-21) revealed the conditions for the prograde metamorphism of the

metamafic blocks. The earliest stage of metamorphism (Stage 1) was subdivided as the garnet core assemblage (Stage 1a = ~625 °C, 11.5 kbar) and the garnet rim and matrix assemblage (Stage 1b = 700 °C, 13 kbar; Figs. 2.1c and 2.3; Valera et al., 2021). In Valera et al. (2021), the Ep amphibolite and amphibolite blocks preserve comparable peak metamorphic conditions constrained by Zr-in-rutile geothermometry (Tomkins et al., 2007) and the TZARS geobarometer based on the reaction 3 An + 2 Czo + Rt + Qz = 3 An + Ttn + H_2O (Kapp et al., 2009).

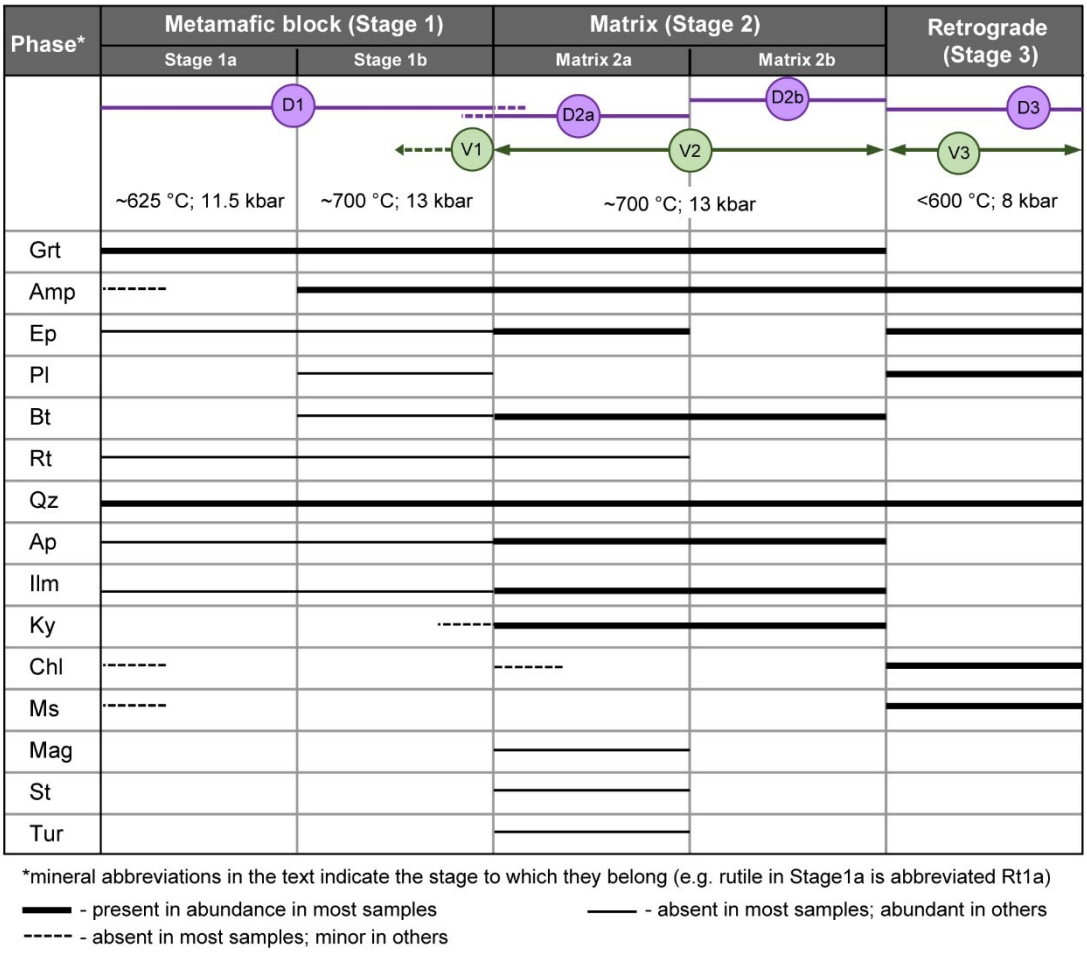

Fig. 2.3. Summary of the mineral paragenesis comprising the block (Stage 1), matrix (Stage 2), and replacement minerals (Stage 3) adopted from Valera et al. (2021). The deformation (D) and veining (V) stages of the Dalrymple Amphibolite are also indicated. The *P-T* conditions for each stage are also shown.

Table 2.1. Summary of samples used in this study

Sample number	Locality			Field occurrence	Lithology	Major mineral assemblage [+secondary]	Accessory minerals	Whole-rock chemistry
	Area	Latitude	Longitude					
B213-4	Botoon	10°8'7.1"N	118°48'47.7"E	Block	Amphibolite	Camp + Pl [+Ab]	Ilm	○
B213-7	Botoon	10°8'7.1"N	118°48'47.7"E	Matrix2a	Ky-Grt schist	Ky + Grt + Ilm [+Ms +Chl]	Rt + Qz + Zrn + Ap	○
B213-8	Botoon	10°8'7.1"N	118°48'47.7"E	Block	Grt amphibolite	Camp + Grt + Qz + Ep [+Chl +Ep]	Rt + Ilm + Zrn + Ap	○
B213-9	Botoon	10°8'7.1"N	118°48'47.7"E	Block	Grt amphibolite	Camp + Grt + Qz + Ep + Ky [+Chl +Ep]	Rt + Ilm + Zrn + Ap	○
B214-1	Botoon	10°7'44.2"N	118°48'40.2"E	Matrix2a and 2b	Ky-Camp schist	Camp + Ky + Bt + Ilm [+Ms +Chl]	Ap + Tur	○
B214-2G	Botoon	10°7'44.2"N	118°48'40.2"E	Matrix2a	Ky-Grt-Bt-Camp schist	Camp + Grt + Ky + St + Bt [+Chl]	Rt + Ilm + Zrn + Ap + Chl	○
B214-2H	Botoon	10°7'44.2"N	118°48'40.2"E	Block	Amphibolite	Camp + Qz [+Chl]	Rt + Ilm + Zrn + Ep	○
B214-7E	Botoon	10°7'44.0"N	118°48'40.4"E	Block	Ep amphibolite	Camp + Ep + Qz	Rt + Zrn + Ilm + Ttn	○
B214-7C	Botoon	10°7'44.0"N	118°48'40.4"E	Block	Metacarbonate	Cb + Ep + Camp + Rt	Ilm + Ttn + Chl	○
B214-8	Botoon	10°7'44.4"N	118°48'40.6"E	Matrix2a and 2b	Ky-Camp-Bt schist	Matrix2a and 2b: Camp + Oam + Ky + Ilm + Bt [+Ms +Chl]	Grt + Ap	○
B214-10	Botoon	10°7'44.7"N	118°48'41"E	Matrix2a	Ky-Camp-Bt schist	Ky + Ilm + Bt [+Ms +Chl]	Mag + Ap + Tur + Oam + Camp + Grt	○
B214-13	Botoon	10°7'44.7"N	118°48'41"E	Block	Amphibolite	Ky + Grt + Ilm [+Ms +Chl]	Rt + Qz + Zrn + Ap	○
B214-14	Botoon	10°7'45.8"N	118°48'41"E	Matrix2a	Ky-Ep-Grt schist	Ky + Grt + Ep + Ilm + Bt [+Ms +Ep +Chl]	Rt + Ap + Zrn + Chl	
B214-15	Botoon	10°7'45.8"N	118°48'40.4"E	Matrix 2a	Ky-Camp schist	Camp + Grt + Qz + Ky [+Ms +Chl]	Ilm + Bt + Ap	○
B214-16	Botoon	10°7'45.8"N	118°48'40.4"E	Matrix 2a	Ky schist	Ky + Ilm + Qz [+Ms +Chl]	Ap	○
B214-21	Botoon	10°7'45.0"N	118°48'40.1"E	Block	Grt amphibolite	Camp + Grt + Ep + Qz [+Act +Ep +Chl]	Ky + Bt + Ap + Rt + Ilm + Zrn	○

Table 2.1. continued

Sample number	Locality			Field occurrence	Lithology	Major mineral assemblage [+secondary]	Accessory minerals	Whole-rock chemistry
	Area	Latitude	Longitude					
B214-22	Botoon	10°7'45.0"N	118°48'40.1"E	Block	Ep amphibolite	Camp + Ep + Qz	Rt + Zrn + Ttn + Ap + Ilm	○
B214-25	Botoon	10°7'44.6"N	118°48'41.0"E	Matrix 2a	Ky-Grt-Camp schist	Camp + Grt + Ky + Ep + Qz + Ilm [+Ms + Chl]	Rt + Zrn + Ap	○
B214-26	Botoon	10°7'44.6"N	118°48'41.0"E	Block	Camp-Ky-quartzite	Camp + Ky + Ilm [+Ms +Chl]	Ap	○
B214-29	Botoon	10°7'44.6"N	118°48'40.8"E	Matrix2a and 2b	Ky-Hbl-Qz schist	Matrix2a: Camp + Oam + Qz + Ky + Chl [+Chl +Ms] Matrix2b: Camp + Oam + Qz + Ky [+Ms]	Both 2a and 2b: Ilm	○
N215-3	Nanad	10°7'24.3"N	118°48'26.1"E	Matrix2a and 2b	Grt-Hbl-Bt schist	Matrix2a and 2b: Camp + Grt + Ky + Bt + Qz [+Ms +Chl]	Ilm + Rt + Zrn + Ap	○
N215-4	Nanad	10°7'24.3"N	118°48'26.1"E	Block	Ky-Ilm-Grt quartzite	Ky + Ilm + Grt + Qz [+Ms +Chl]	Rt + Ap + Tur	○
N215-11	Nanad	10°7'23.8"N	118°48'25.8"E	Block	Ep amphibolite	Camp + Ep + Qz	Ky + Pl + Ap	○
D113-5	Dalrymple	10°6'39.4"N	118°48'41.1"E	Block	Ep amphibolite	Camp + Ep + Pl + Qz [+Act +Ab]	Rt + Zrn + Ttn + Ap + Bt	○
D113-9	Dalrymple	10°6'41.6"N	118°48'36.7"E	Block	Amphibolite	Camp + Ep + Pl + Qz [+Act +Chl +Ab]	Rt + Zrn + Ttn	○
D113-10	Dalrymple	10°6'41.6"N	118°48'36.7"E	Block	Ep amphibolite	Camp + Ep + Pl + Qz [+Chl +Ab]	Rt + Zrn + Ttn + Ap + Bt	○
D113-11	Dalrymple	10°6'41.6"N	118°48'36.7"E	Block	Amphibolite	Camp + Ep + Pl + Qz [+Act +Ab]	Rt + Zrn	○
D113-13	Dalrymple	10°6'41.6"N	118°48'36.7"E	Block	Ep amphibolite	Camp + Ep + Pl + Qz [+Chl +Ab]	Rt + Zrn + Ttn + Ap	○
D113-14A	Dalrymple	10°6'42.5"N	118°48'36.1"E	Block	Amphibolite	Camp + Pl + Qz + Ep [+Act +Chl +Ep]	Rt + Zrn + Ap + Ms	○
D113-14G	Dalrymple	10°6'42.5"N	118°48'36.1"E	Block	Grt amphibolite	Camp + Grt + Pl + Qz + Ep [+Act +Chl +Ep]	Rt + Zrn + Ap + Ms	○

Table 2.1. continued

Sample number	Locality			Field occurrence	Lithology	Major mineral assemblage [+secondary]	Accessory minerals	Whole-rock chemistry
	Area	Latitude	Longitude					
N215-11	Nanad	10°7'23.8"N	118°48'25.8"E	Block	Ep amphibolite	Camp + Ep + Qz	Ky + Pl + Ap	○
D113-5	Dalrymple	10°6'39.4"N	118°48'41.1"E	Block	Ep amphibolite	Camp + Ep + Pl + Qz [+Act +Ab]	Rt + Zrn + Ttn + Ap + Bt	○
D113-9	Dalrymple	10°6'41.6"N	118°48'36.7"E	Block	Amphibolite	Camp + Ep + Pl + Qz [+Act +Chl +Ab]	Rt + Zrn + Ttn	○
D113-10	Dalrymple	10°6'41.6"N	118°48'36.7"E	Block	Ep amphibolite	Camp + Ep + Pl + Qz [+Chl +Ab]	Rt + Zrn + Ttn + Ap + Bt	○
D113-11	Dalrymple	10°6'41.6"N	118°48'36.7"E	Block	Amphibolite	Camp + Ep + Pl + Qz [+Act +Ab]	Rt + Zrn	○
D113-13	Dalrymple	10°6'41.6"N	118°48'36.7"E	Block	Ep amphibolite	Camp + Ep + Pl + Qz [+Chl +Ab]	Rt + Zrn + Ttn + Ap	○
D113-14A	Dalrymple	10°6'42.5"N	118°48'36.1"E	Block	Amphibolite	Camp + Pl + Qz + Ep [+Act +Chl +Ep]	Rt + Zrn + Ap + Ms	○
D113-14G	Dalrymple	10°6'42.5"N	118°48'36.1"E	Block	Grt amphibolite	Camp + Grt + Pl + Qz + Ep [+Act +Chl +Ep]	Rt + Zrn + Ap + Ms	○
D113-15	Dalrymple	10°6'42.5"N	118°48'36.1"E	Block	Grt amphibolite	Camp + Grt + Pl + Qz + Ep [+Chl +Ep +Ab]	Rt + Ap + Ms + Ccp + Py	○
D113-16	Dalrymple	10°6'43.3"N	118°48'36.3"E	Block	Ep amphibolite	Camp + Ep + Pl + Qz [+Chl +Ab]	Rt + Zrn + Ttn + Ap	○
D113-18	Dalrymple	10°6'43.3"N	118°48'36.3"E	Block	Grt amphibolite	Camp + Grt + Pl + Qz + Ep + Bt [+Act +Chl +Ep +Ab]	Rt + Zrn + Ap	○
D113-21	Dalrymple	10°6'42.5"N	118°48'36.1"E	Block	Ky-Camp schist	Camp + Qz + Bt + Ky(?) [+Ms +Chl]	Ap + Ilm	○
D215-7	Dalrymple	10°6'43.3"N	118°48'36.3"E	Block	Ep-Bt-Ms schist	Bt + Ms + Pl + Ep +Qz [+Chl]	Rt + Ilm + Zrn + Ap	○
D217-2	Dalrymple	10°6'43.3"N	118°48'36.3"E	Block	Ky-Camp-Bt schist	Bt + Camp + Ky + Ilm + Qz [+Ms +Chl]	Ap	○

The matrix (Stage 2) surrounding the blocks are typically highly-sheared and exhibit variable mineralogy but always include ilmenite and kyanite, with some samples containing variable amounts of hornblende, biotite, quartz, and garnet (Table 2.1). The *P-T* history of the matrix and the deformation events related to the transformation of the slab-mantle wedge interface into a mélange complex is grouped as Stage 2 (Valera et al., 2021). In Botoon and Nanad, two generations of matrix formation (matrix2a and 2b) are identified (Figs. 2.2, 2.3). Both matrix2a and 2b are defined by the same mineral assemblage but distinguished by cross-cutting pervasive foliation directions and by lenses of matrix2a found in matrix2b (Valera et al., 2021).

Geothermobarometry of a matrix2a sample (B214-14) constrained similar peak metamorphic conditions (~700 °C, 13 kbar) as the metamafic blocks (Valera et al., 2021). This similarity in peak *P-T* conditions was confirmed by pseudosection modelling and suggests that matrix-forming processes (i.e. deformation, mixing, and fluid-infiltration) occurred as the whole mélange sequence was being subducted at depth (Valera et al., 2021). Several generations of quartz, quartz-kyanite, and epidote veins cross-cut the block and the matrix of the sequence implying extensive fluid activity throughout its *P-T-D* history.

Based on its block-in-matrix occurrence and the cooler paleogeothermal gradient (~16 °C/km) preserved in the Dalrymple Amphibolite, the mélange is suggested to correspond to the slab-mantle wedge interface of a young subduction complex already transitioning from the much warmer conditions of subduction initiation (Valera et al., 2021). The blocks and surrounding matrix were then affected by migrating fluids during its retrograde metamorphism with maximum *T* and *P* conditions of ~600 °C, 8 kbar. This event led to the formation of replacement minerals such as chlorite (Chl3), biotite (Bt3), actinolite (Camp3) and epidote (Ep3) at the expense of earlier formed minerals in the blocks and matrix samples such as garnet (Grt1/Grt2), amphibole (Camp1/Camp2) and biotite (Bt1/Bt2; Valera et al., 2021). The matrix samples used in this study have variable degrees of Stage 3 imprint. This allowed us to determine the progressive effect of fluid-related mass-transfer even as the metamorphic sequence was being exhumed.

2.4 Methodology

Mineral chemistry analysis of rock-forming minerals and X-ray elemental mapping were conducted using a JEOL JXA-8105 electron probe microanalyzer. Analytical conditions for quantitative analyses were 15.0 kV acceleration voltage, 10 nA beam current, and 3 μm beam diameter. The counting time for the peak and backgrounds were 30 s and 15 s for Cl, 60 s and 30 s for F, and 10 s and 5 s for other elements. Natural and synthetic minerals were used as standards and ZAF correction was applied. Estimating Fe^{3+} in garnet and Ca-amphibole is after Droop (1987) and Schumacher (1991). Analytical conditions for determining trace element (Nb, Zr, and Cr) concentration of rutile followed that of Zack et al. (2004). Acceleration voltage used was 20.0 kV, 120 nA probe current and a probe diameter of 5 μm to determine both major and trace element concentration of the rutile grains. Elemental mapping was conducted using an acceleration voltage of 15.0 kV, probe current of 600-800 nA and a dwell time of 60-80 msec, with a beam diameter of 3–5 μm. These analyses were done at the Department of Geology and Mineralogy, Kyoto University.

Nineteen (19) metamafic blocks, four (4) metasedimentary blocks, and twelve (12) matrix samples, four of which contain both matrix2a and 2b were analyzed for whole-rock major and trace element concentration (Table 2.1). Major and trace element data for blocks and matrix samples are given in Tables 2.2 and 2.3, respectively. The samples were selected to represent the variable mineralogy and degree of Stage 3 imprint on the blocks and the matrix. The samples were powdered in a tungsten-carbide mill at Kyoto University. Whole-rock geochemical analyses were performed at Bureau Veritas, Perth, Australia. Major-element concentrations were obtained by fused glass bead X-ray fluorescence (XRF) analysis while trace element data was obtained by laser ablation inductively coupled mass spectrometry (LA-ICPMS) of the same glass beads. Loss on ignition for the metamafic blocks are low (0.4–2.6%) while those of the matrix (1.38–4.72%) and metasedimentary blocks (1.1–13.49%) are generally higher. Analytical precision, i.e. relative standard deviation (RSD), based on replicate sample analysis done after every batch of ten samples, was within 1% for major oxides and 10% for trace elements. Accuracy based on standards is within

0.5% for major oxides except K_2O (1.89%) and within 7% for trace elements. Accuracy computation was done based on the reference materials EuroNorm 782-1 for major oxides and NSC DC 86308 Zirconium Ore for trace elements. The secondary standard SDSYB was also analyzed together with the samples. Comparing our results with those of Nakashima et al. (2000) and Shimoda et al. (2004) yielded RSD values of within 1% for most major elements except MgO (3.97%) and K_2O (5.88%), and better than 5% for most trace elements except Rb (17.71%), Pb (14.29%), Nd (23.53%) and Yb (14.37%). High RSD values for Pb, Nd, Yb (>10 ppm) and Rb (~30 ppm) are ascribed to low concentration of these elements in SDSYB. Recalculation of major oxides to anhydrous basis was done before plotting the data. FeO* in the plots was obtained by dividing the Fe_2O_3* values by 1.11.

2.5 Sample description

Detailed description of the petrographic and mineral chemistry of the metamafic block samples used in this study are available in Valera et al. (2021) such that only a general description follows. The metamafic blocks are amphibolites composed of Camp+Qz with varying amounts of garnet, epidote (clinozoisite) and plagioclase. Accessory minerals in the metamafic blocks are biotite, rutile, ilmenite, and zircon. The garnet porphyroblasts in the Grt amphibolite blocks preserve prograde zonation (cf. Valera et al., 2021). At the core of some garnet porphyroblasts are multiphase solid inclusions which consist of lower-*T* assemblage (Chl+Ep+Qz+Grt+Rt+Ilm). The rim of the garnet porphyroblasts are in textural equilibrium with the surrounding matrix of Ca-amphibole and epidote (Fig. 2.2d–f; Valera et al., 2021).

Ca-amphibole in the amphibolites are classified as hornblende (Leake et al., 1997). They range from ferrotschermakite to tschermakite with minor magnesiohornblende in the Grt amphibolite blocks. Those in the amphibolites and Ep amphibolites range from tschermakite to magnesiohornblende with slightly lower total Al content and higher Si and Mg# than the Grt amphibolite. Epidote in the metamafic blocks are more common in the amphibolite and Ep amphibolite. Plagioclase are found only in the metamafic blocks in Dalrymple point. Most plagioclases are Ca-poor: $An_{1\text{-}15}$ in Ep amphibolites, $An_{2\text{-}17}$ in amphibolites and $An_{10–18}$ in Grt

amphibolites. Some Ep amphibolite (D113-8 = $An_{16–27}$) and Grt amphibolite (D113-15 = $An_{15–24}$) blocks however have higher anorthite content (Valera et al., 2021). These blocks represent a gabbroic protolith as discussed below. Rutile in the metamafic blocks generally have low Nb content (<2000 ppm). Rutile grains included in the rim of the garnet porphyroblasts and in the matrix of the Grt amphibolite blocks B214-21 however shows a ten-fold increase in Nb concentration (720–5606 ppm) compared to those at the garnet core (175–266 ppm). The drastic increase was interpreted to be related to the progressive mixture of mafic and sedimentary components during prograde metamorphism of the sequence (Valera et al., 2021).

Some metamafic blocks exhibit similar high-Nb rutile (e.g. B214-13; Nb = 336–5,327 ppm) as well. These metamafic blocks also record enrichments in whole-rock, light rare earth elements (LREEs) and Th as discussed below. In the field, these blocks are found either to contain relict metasedimentary domain (B214-7E), is adjacent to the matrix (B214-13), or is at the outermost edge of a metamafic block (B213-9 Grt+Camp+Ky; Fig. 2.2c). In the case of the Grt amphibolite B213-9 (Fig. 2.2e), the core portion of the block is kyanite-free (B213-8; Fig. 2.2d) and the whole-rock chemistry is comparable to other Grt amphibolite blocks, i.e. flat REE pattern and no enrichment in Th relative to Ba (see below). Matrix (B213-7; Grt+Ky) material is observed surrounding another metamafic block nearby and was sampled in this study.

In the localities of Botoon and Nanad, two generations of matrix are identified based on their cross-cutting relationships (Valera et al., 2021). The earlier-formed matrix2a is cross-cut by matrix2b in Botoon matrix2a is completely transformed into blocks in Nanad (Fig. 2.2k). Both matrix2a and 2b consist of the same mineral assemblage (Botoon: Oam+Camp+Ky+Ilm; Nanad: Grt+Bt+Ilm+Ky+Camp) (Valera et al., 2021). The matrix samples exhibit variable phase assemblage but always include kyanite and ilmenite (Table 2.1). The phase assemblage of matrix samples such as B214-25 (Fig. 2.4a–c) and B214-2G (Fig. 2.4d,e) for example is similar to the Grt amphibolite blocks (Camp+Grt+Ep) except for the presence of aluminosilicates such as kyanite (and staurolite in

the case of B214-2G) in these matrix samples. Others either completely lack Ca-amphibole (e.g. B213-7; Fig. 2.4f,g and B214-16) or have them as an accessory phase (B214-10).

The amount of garnet in the matrix samples is also variable. Some samples such as B214-1 and B214-29 (Fig. 2.4h,i) completely lack garnet whereas in other samples, garnet occurs abundantly either as fine euhedral grains (B213-7; Fig. 2.4f,g) and/or coarse porphyroclasts (N215-3; Fig. 2.4j-k). Replacement by Stage 3 minerals occurs in variable degree depending on the samples. The aluminosilicates in B214-2G (kyanite and staurolite; Fig. 2.4d,e) and B214-10 (kyanite; Fig. 2.4l,m) for example, are almost free of muscovite alteration (Ms3). In sample D113-21, on the other hand, Stage 2 kyanite (Ky2a) are completely lost and only fine grains of pseudomorphic muscovite (Ms3) remain (Fig. 2.4n,o).

The garnet grains in the matrix (matrix2a and 2b) either do not exhibit zonation or preserve a subtle zonation (e.g. Fig. 2.4a,b) in contrast to the garnet porphyroblasts of the blocks (Valera et al., 2021). They also have higher Mg# and lower grossular component (e.g. B214-2G Mg# = 0.44–0.47; Grs_{16-19}) than those in the blocks (e.g. D113-18 Mg# = 0.30–0.38; $Grs_{18–23}$; Valera et al., 2021). Ca-amphibole in the matrix are also hornblende ranging from tschermakite to magnesiohornblende. Their Mg# (= 0.72–0.78) are higher than the blocks and more uniform across all samples (Valera et al., 2021).

Rutile grains are less common in the matrix samples compared to the blocks. In samples where they occur, the rutile grains preserve variable Cr-Nb concentration. Samples either have rutile with low Cr, high Nb (e.g. 213-7, Cr 89–698 ppm; Nb = 5, 215–29,695 ppm) contents or high Cr and Nb concentrations (e.g. B214-2G, Cr = 376–2,319 ppm; Nb = 35–4,607 ppm) (Fig. 2.4p). The Cr-Nb contents of rutile in the matrix do not vary with their Zr content although rutile in some samples such as B213-7 (= 450 ppm) have lower mean maximum Zr content (cf. Penniston-Dorland et al., 2018) than other samples such as B214-2G (= 645 ppm).

Table 2.2 Major and trace element data of blocks in Dalrymple Amphibolite

Lithology	Ep amphibolite						
Locality	Dalrymple				Botoon		Nanad
Sample	D113-5	D113-10	D113-13	D113-16	B214-7E	B214-22	N215-11
in wt.%							
SiO_2	48.24	47.28	43.90	41.99	46.74	45.61	46.20
TiO_2	1.52	0.91	0.81	0.90	0.70	1.92	0.14
Al_2O_3	15.15	14.92	17.55	19.17	11.95	14.32	18.69
Fe_2O_3*	11.44	9.32	9.89	11.20	10.28	13.88	5.13
MnO	0.19	0.24	0.21	0.14	0.60	0.65	0.11
MgO	6.32	8.54	6.77	7.54	14.23	7.93	9.69
CaO	11.98	15.15	17.28	15.62	12.16	12.72	16.38
Na_2O	3.32	0.98	1.27	1.21	1.12	0.79	1.25
K_2O	0.62	0.38	0.32	0.43	0.26	0.21	0.27
P_2O_5	0.16	0.49	0.35	0.02	0.01	0.08	0.06
SrO	0.03	0.05	0.07	0.07	0.02	0.04	0.03
BaO	0.02	0.02	0.01	0.01	0.02	0.02	0.02
Cr_2O_3	0.04	0.06	0.04	0.01	0.12	0.02	0.14
Ni	0.01	0.02	0.02	0.01	0.07	0.01	0.02
Zn	0.01	0.01	0.01	0.01	0.02	0.01	0.01
Total	100.13	100.08	100.15	100.03	99.85	99.75	100.26
LOI	1.08	1.72	1.65	1.71	1.54	1.55	2.14
in ppm							
Rb	10.20	9.20	5.75	10.80	2.80	3.50	6.20
Th	0.21	1.17	0.69	0.04	8.21	0.31	0.61
U	0.15	2.16	6.85	0.06	1.22	3.13	3.13
Nb	2.73	3.68	2.99	0.57	10.80	6.74	0.25
Ta	0.42	0.75	0.59	0.29	0.98	0.86	0.36
La	4.32	4.07	2.24	0.86	23.10	5.27	0.64
Ce	10.50	9.36	4.96	2.32	51.80	13.90	1.30
Pb	2.00	6.00	8.00	3.00	12.00	17.00	10.00
Pr	2.04	1.41	0.86	0.39	5.70	2.48	0.21
Nd	10.40	6.88	4.32	2.51	22.40	13.60	1.00
Zr	90.50	39.00	30.50	15.00	95.00	112.00	6.00
Hf	2.61	1.34	1.16	0.54	2.60	3.27	0.21
Sm	3.39	1.99	1.46	0.98	4.64	4.65	0.47
Eu	1.28	0.73	0.58	0.60	1.03	1.76	0.27
Gd	4.88	2.57	2.32	1.32	4.38	6.12	0.73
Tb	0.86	0.49	0.46	0.25	0.69	1.17	0.15
Dy	5.77	3.17	3.58	1.67	4.20	7.57	1.09
Y	32.30	20.60	25.30	10.10	23.30	41.90	6.24
Ho	1.27	0.74	0.85	0.40	0.88	1.68	0.22
Er	3.62	2.36	2.78	1.17	2.49	4.75	0.60
Tm	0.54	0.40	0.42	0.18	0.42	0.67	0.10
Yb	3.63	2.64	2.84	1.16	2.52	4.24	0.60
Lu	0.47	0.38	0.43	0.17	0.38	0.59	0.08

L.O.I.=loss on ignition; b.d.=below detection limit; n.d.=not determined; Fe_2O_3* = total Fe

Table 2.2 Continued

Lithology	Amphibolite					
Locality	Dalrymple			Botoon		
Sample	D113-9	D113-11	D113-14A	B213-4	B214-2H	B214-13
in wt.%						
SiO_2	47.06	48.12	45.02	46.69	45.58	44.97
TiO_2	0.60	0.31	1.59	0.57	0.81	0.88
Al_2O_3	12.05	10.84	13.93	13.47	13.94	14.24
Fe_2O_3*	11.02	10.41	12.79	10.40	11.58	11.93
MnO	0.38	0.32	0.35	0.39	0.38	0.56
MgO	14.30	15.12	12.72	14.14	14.26	13.13
CaO	10.36	10.90	9.46	9.24	9.23	9.63
Na_2O	2.05	1.91	2.04	2.36	1.72	1.58
K_2O	0.38	0.42	0.51	0.45	0.48	0.59
P_2O_5	0.01	0.12	0.15	0.04	0.03	0.04
SrO	0.01	0.01	0.01	0.01	0.01	0.01
BaO	0.02	0.02	0.01	0.01	0.02	0.02
Cr_2O_3	0.14	0.04	0.09	0.03	0.13	0.06
Ni	0.06	0.02	0.04	0.01	0.06	0.02
Zn	0.02	0.02	0.01	0.02	0.02	0.02
Total	99.99	99.92	100.07	99.67	100.11	99.71
LOI	1.53	1.35	1.35	1.85	1.86	2.03
in ppm						
Rb	8.65	7.70	12.20	11.50	12.30	16.20
Th	1.10	0.70	2.25	0.03	1.48	23.60
U	0.12	0.07	0.34	0.12	0.26	1.71
Nb	4.28	0.50	30.70	1.63	12.50	7.99
Ta	0.41	0.23	2.24	0.23	1.24	0.88
La	4.26	5.92	8.32	0.62	5.39	66.80
Ce	12.50	13.60	22.30	2.14	16.80	149.00
Pb	b.d.	b.d.	2.00	8.00	2.00	6.00
Pr	2.06	1.90	3.30	0.50	2.54	16.40
Nd	10.70	8.66	16.50	2.89	14.40	60.90
Zr	86.00	8.50	164.00	38.50	130.00	60.00
Hf	2.54	0.43	4.24	1.26	3.67	2.09
Sm	3.40	2.29	5.39	1.25	4.89	12.80
Eu	0.97	0.80	1.44	1.53	1.44	2.97
Gd	4.01	2.29	6.56	2.11	5.81	12.90
Tb	0.66	0.35	1.14	0.46	1.02	2.24
Dy	4.35	1.89	7.15	3.41	6.52	14.10
Y	25.30	10.30	41.40	18.40	37.10	73.50
Ho	0.91	0.38	1.55	0.75	1.37	2.84
Er	2.67	0.96	4.63	2.19	4.11	7.77
Tm	0.39	0.15	0.67	0.32	0.62	1.09
Yb	2.62	0.98	4.24	1.92	3.93	6.54
Lu	0.38	0.15	0.61	0.27	0.60	0.85

L.O.I.=loss on ignition; b.d.=below detection limit; n.d.=not determined; Fe_2O_3* = total Fe

Table 2.2. Continued

Lithology	Grt amphibolite						
Locality	Dalrymple			Botoon			
Sample	D113-14G	D113-15	D113-18	B213-8	B213-9		B214-21
in wt.%							
SiO_2	39.76	53.63	47.46	44.34	38.03	41.83	43.16
TiO_2	2.52	2.90	1.08	1.36	1.73	1.42	2.20
Al_2O_3	17.27	15.83	14.66	14.75	19.52	21.55	14.02
Fe_2O_3*	21.30	14.01	15.90	16.55	22.63	11.15	15.84
MnO	0.34	0.26	0.45	1.22	3.03	0.32	0.57
MgO	6.99	3.17	8.69	10.86	9.39	11.63	11.02
CaO	8.86	4.55	6.91	7.50	4.38	6.98	8.90
Na_2O	1.25	4.72	0.97	1.21	0.42	1.38	1.33
K_2O	1.09	0.54	0.81	0.36	0.20	1.50	0.51
P_2O_5	0.01	0.03	0.13	0.03	0.03	0.16	0.06
SrO	0.02	0.03	0.01	0.01	0.01	0.01	0.01
BaO	b.d.	0.03	0.02	0.02	0.01	0.04	0.01
Cr_2O_3	0.02	b.d.	0.00	0.01	0.01	0.05	0.02
Ni	0.02	0.00	0.00	0.01	0.01	0.04	0.01
Zn	0.01	0.01	0.07	0.08	0.03	0.01	0.02
Total	100.27	100.07	99.80	99.33	99.41	100.06	99.32
LOI	39.76	53.63	47.46	1.03			1.63
in ppm							
Rb	29.50	8.05	27.30	8.85	6.70		10.40
Th	0.05	0.06	1.00	0.20	3.26		1.10
U	0.03	0.08	0.13	0.22	0.44		1.00
Nb	0.77	0.91	1.45	1.44	20.80		20.30
Ta	0.66	0.69	0.50	0.75	2.77		1.95
La	0.90	1.01	4.64	2.59	9.92		4.63
Ce	2.82	2.80	11.10	7.66	20.30		12.80
Pb	b.d.	2.00	2.00	b.d.	b.d.		4.00
Pr	0.51	0.47	1.63	1.44	2.26		2.06
Nd	2.79	2.40	8.66	8.10	8.08		10.60
Zr	16.50	27.00	51.00	60.00	90.50		121.00
Hf	0.56	0.82	1.56	1.99	2.76		3.61
Sm	0.98	0.90	2.68	3.09	1.80		3.87
Eu	0.73	0.70	0.99	1.04	0.49		1.14
Gd	1.68	1.40	3.67	4.06	3.11		5.44
Tb	0.35	0.27	0.68	0.78	0.89		1.11
Dy	2.50	1.87	4.84	5.46	8.14		7.50
Y	15.40	11.00	27.90	31.90	58.80		41.30
Ho	0.62	0.41	1.07	1.23	2.20		1.62
Er	1.80	1.16	3.42	3.69	7.56		4.74
Tm	0.30	0.18	0.48	0.57	1.24		0.72
Yb	1.85	1.26	3.22	3.89	8.83		4.75
Lu	0.29	0.17	0.48	0.54	1.37		0.67

L.O.I.=loss on ignition; b.d.=below detection limit; n.d.=not determined; Fe_2O_3* = total Fe

Table 2.2 Continued

Lithology	Ky-Ilm-Grt quartzite	Ep-Bt-Ms schist	Camp-Ky-quartzite	Metacarbonate
Locality	Nanad	Dalrymple	Botoon	Botoon
Sample	N215-4	D215-7	B214-26	B214-7C
in wt.%				
SiO_2	76.34	42.99	57.96	28.41
TiO_2	0.46	3.26	1.20	0.59
Al_2O_3	11.76	19.22	18.58	13.89
Fe_2O_3*	5.46	15.64	11.18	9.32
MnO	0.42	0.14	0.20	0.91
MgO	2.01	3.36	4.62	5.20
CaO	0.70	3.84	2.32	27.32
Na_2O	0.10	3.19	0.47	0.34
K_2O	0.99	4.77	1.62	0.06
P_2O_5	0.34	1.31	0.11	0.06
SrO	b.d.	0.03	0.01	0.06
BaO	0.02	0.13	0.03	0.01
Cr_2O_3	0.01	0.04	0.01	0.06
Ni	0.01	0.01	0.01	0.02
Zn	0.00	0.01	0.01	0.01
Total	99.72	100.04	99.72	99.74
LOI	1.1	2.09	1.4	13.49
in ppm				
Rb	37.80	106.00	77.00	0.55
Th	9.77	8.62	0.92	10.90
U	0.70	0.93	0.29	3.19
Nb	5.01	90.00	2.91	10.40
Ta	1.55	5.14	1.09	1.17
La	44.20	75.70	4.39	55.90
Ce	70.80	118.00	10.50	74.50
Pb	2.00	4.00	b.d.	33.00
Pr	11.00	15.40	1.54	14.50
Nd	43.30	58.90	7.28	59.80
Zr	106.00	275.00	68.50	120.00
Hf	3.00	6.57	2.14	3.29
Sm	8.40	11.30	2.21	12.60
Eu	1.69	3.33	0.79	2.83
Gd	7.72	10.20	3.24	12.00
Tb	1.06	1.49	0.64	1.79
Dy	6.47	8.54	4.54	11.10
Y	37.60	47.60	26.90	70.00
Ho	1.35	1.71	1.09	2.44
Er	4.22	4.51	3.24	7.10
Tm	0.60	0.63	0.51	1.04
Yb	4.07	3.64	3.52	6.44
Lu	0.60	0.49	0.48	0.98

L.O.I.=loss on ignition; b.d.=below detection limit; n.d.=not determined; Fe_2O_3* = total Fe

Table 2.3. Measured major and trace element data of matrix in Dalrymple Amphibolite

Lithology	Ky-Grt-Bt-Camp schist	Ky-Camp schist	Ky-Camp-Bt schist	Ky-Camp schist	Ky schist	Ky-Grt-Camp schist
Locality	Botoon	Dalrymple	Dalymple	Botoon	Botoon	Botoon
Sample	B214-2G	D113-21	D217-2	B214-15	B214-16	B214-25
in wt.%						
SiO_2	41.83	51.78	38.67	51.87	28.75	38.14
TiO_2	1.42	0.65	1.22	0.70	2.34	2.29
Al_2O_3	21.55	17.84	22.01	17.56	29.99	15.25
Fe_2O_3*	11.15	8.57	14.85	9.27	23.93	23.89
MnO	0.32	0.35	0.29	0.40	0.36	0.52
MgO	11.63	9.80	10.17	9.63	5.52	10.27
CaO	6.98	2.40	3.38	3.03	1.20	6.36
Na_2O	1.38	1.14	0.89	1.25	0.46	0.99
K_2O	1.50	3.21	3.25	2.02	2.87	0.61
P_2O_5	0.16	0.09	0.16	0.12	0.58	0.04
SrO	0.01	0.01	0.01	0.01	0.01	0.01
BaO	0.04	0.06	0.06	0.03	0.04	0.01
Cr_2O_3	0.05	0.07	0.07	0.08	0.03	0.00
Ni	0.04	0.04	0.05	0.04	0.03	0.01
Zn	0.01	0.01	0.01	0.01	0.02	0.01
Total	100.06	100.26	99.80	99.50	100.10	99.79
LOI	1.98	4.25	4.72	3.47	3.98	1.38
in ppm						
Rb	54.10	101.00	104.00	76.60	106.00	22.10
Th	28.80	11.60	22.60	12.60	42.60	11.10
U	0.88	0.85	0.56	0.54	0.97	0.31
Nb	22.60	7.34	10.10	6.93	16.10	4.88
Ta	1.91	0.80	0.70	0.85	0.98	0.68
La	80.80	27.40	54.00	31.40	115.00	30.10
Ce	180.00	64.20	127.00	72.10	252.00	66.40
Pb	2.00	15.00	5.00	7.00	10.00	3.00
Pr	17.20	6.59	12.50	7.58	28.70	7.33
Nd	59.50	25.20	46.00	28.80	113.00	28.20
Zr	239.00	115.00	209.00	122.00	397.00	83.50
Hf	6.73	3.48	5.92	3.63	11.20	2.54
Sm	9.34	5.30	8.43	5.85	22.20	5.42
Eu	1.96	1.40	1.85	1.20	4.52	1.65
Gd	7.00	4.95	7.17	4.96	18.10	5.82
Tb	1.04	0.80	1.09	0.81	2.38	1.01
Dy	6.66	4.91	7.17	5.21	12.10	7.13
Y	36.60	29.90	37.10	27.40	53.50	41.90
Ho	1.47	1.07	1.46	1.05	2.12	1.68
Er	4.29	3.23	4.19	3.00	5.61	5.05
Tm	0.60	0.46	0.62	0.46	0.78	0.79
Yb	4.20	3.27	4.20	2.95	5.17	5.37
Lu	0.59	0.43	0.60	0.45	0.78	0.75

L.O.I.=loss on ignition; b.d.=below detection limit; n.d.=not determined; Fe_2O_3* = total Fe

Table 2.3. Continued

Lithology	Ky-Grt schist	Ky-Camp-Bt schist	Ky-Camp schist	Ky-Camp-Bt schist	Ky-Hbl-Qz schist	Grt-Hbl-Bt schist
Locality	Botoon	Botoon	Botoon	Botoon	Botoon	Nanad
Sample	B213-7	B214-10	B214-01	B214-08	B214-29	N215-3
in wt.%						
SiO_2	36.16	32.65	34.23	39.40	49.92	49.92
TiO_2	1.65	1.86	1.78	1.37	0.63	0.63
Al_2O_3	23.56	33.64	24.54	20.78	14.90	14.90
Fe_2O_3*	15.83	18.66	19.69	15.19	9.53	9.53
MnO	1.50	0.57	0.33	0.57	0.41	0.41
MgO	10.25	6.61	10.13	14.74	13.85	13.85
CaO	3.05	0.63	1.48	1.97	2.63	2.63
Na_2O	0.60	0.14	0.41	0.73	1.26	1.26
K_2O	3.03	2.55	2.81	1.83	2.74	2.74
P_2O_5	0.63	0.27	0.26	0.35	0.12	0.12
SrO	0.02	0.01	0.01	0.01	0.01	0.01
BaO	0.08	0.03	0.01	0.02	0.03	0.03
Cr_2O_3	0.06	0.04	0.04	0.09	0.12	0.12
Ni	0.03	0.03	0.04	0.06	0.06	0.06
Zn	0.01	0.01	0.01	0.01	0.01	0.01
Total	100.14	100.08	100.06	100.13	99.68	99.68
LOI	3.68	2.39	4.29	3	4.39	3.46
in ppm						
Rb	104.00	98.30	133.00	77.90	105.00	122.00
Th	35.80	28.30	27.30	21.70	16.10	8.95
U	1.45	1.21	0.46	0.60	0.53	0.91
Nb	45.30	11.70	7.96	3.14	3.86	7.35
Ta	3.11	0.94	0.58	0.46	0.43	0.79
La	107.00	70.70	79.20	66.00	45.40	24.30
Ce	220.00	172.00	175.00	144.00	101.00	53.80
Pb	6.00	3.00	b.d.	2.00	b.d.	8.00
Pr	27.20	16.80	18.90	15.80	10.70	5.95
Nd	103.00	60.80	71.20	58.30	39.20	22.60
Zr	310.00	307.00	311.00	229.00	175.00	96.00
Hf	8.87	8.54	8.75	6.31	4.92	2.75
Sm	20.00	9.86	13.00	9.96	6.97	4.78
Eu	3.19	1.78	2.61	1.66	1.32	1.07
Gd	17.90	6.81	11.10	7.19	5.48	4.30
Tb	3.03	0.88	1.70	0.93	0.84	0.70
Dy	19.40	6.06	11.00	5.36	5.34	4.42
Y	110.00	37.10	56.60	27.60	27.30	25.00
Ho	4.10	1.48	2.32	1.09	1.08	1.00
Er	11.80	4.97	6.78	2.87	3.12	2.61
Tm	1.69	0.82	0.94	0.47	0.45	0.41
Yb	11.30	6.01	6.07	3.08	2.91	2.62
Lu	1.59	0.93	0.78	0.45	0.44	0.39

L.O.I.=loss on ignition; b.d,=below detection limit; n.d.=not determined; Fe_2O_3*=total Fe

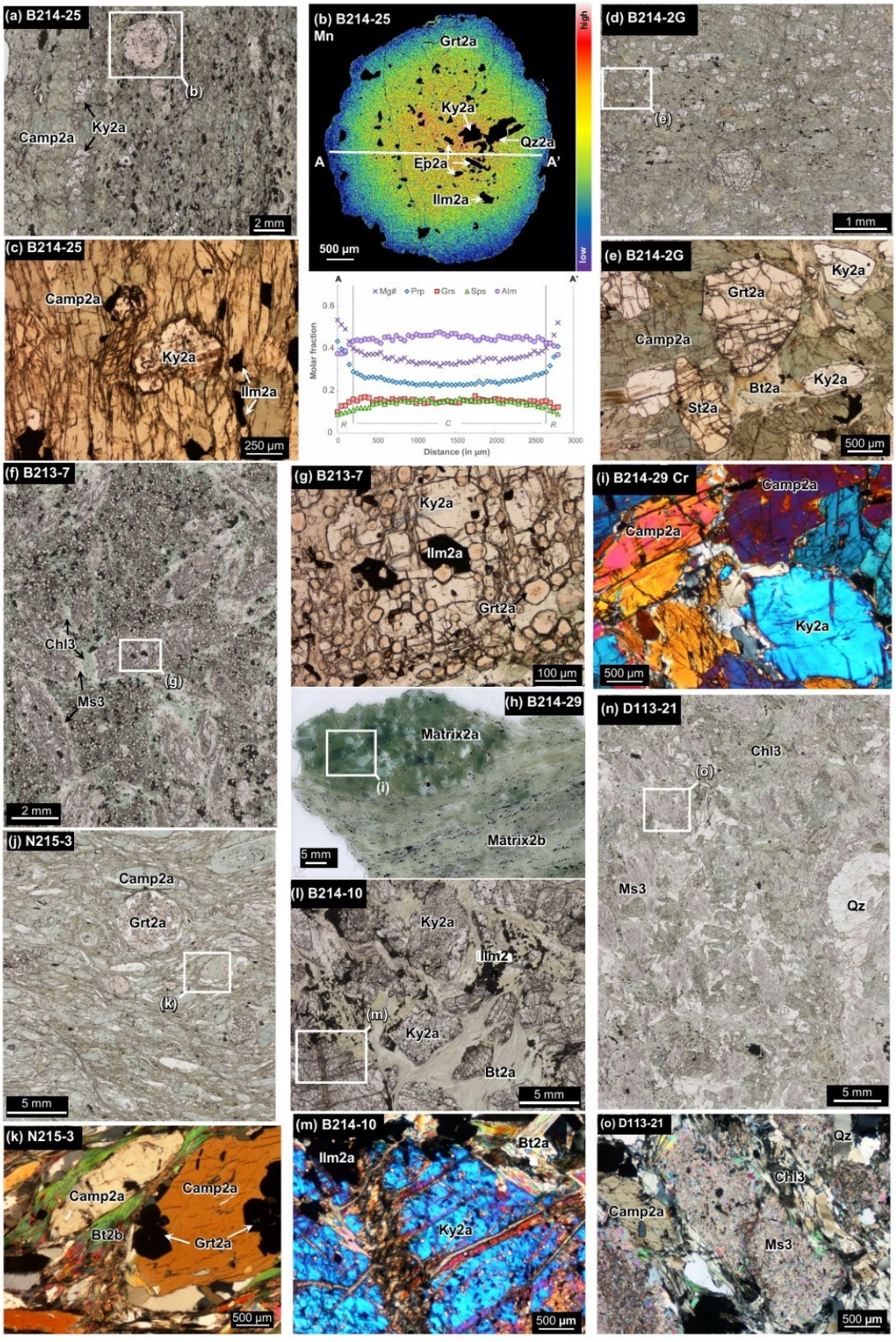
(a) B214-25
(b)
Camp2a
Ky2a
2 mm
(b) B214-25
Mn
Grt2a
Ky2a
Qz2a
A
A'
Ep2a
Ilm2a
500 µm
high
low
(d) B214-2G
(e)
1 mm
(c) B214-25
Camp2a
Ky2a
Ilm2a
250 µm
A
A'
Mg#
Prp
Grs
Sps
Alm
Molar fraction
0.6
0.4
0.2
0
R
C
R
0
500
1000
1500
2000
2500
3000
Distance (in µm)
(e) B214-2G
Ky2a
Grt2a
Camp2a
Bt2a
Ky2a
St2a
500 µm
(f) B213-7
Chl3
(g)
Ms3
2 mm
(g) B213-7
Ky2a
Ilm2a
Grt2a
100 µm
(i) B214-29 Cr
Camp2a
Camp2a
Ky2a
500 µm
(h) B214-29
Matrix2a
(i)
Matrix2b
5 mm
(n) D113-21
Chl3
(o)
Ms3
Qz
5 mm
(j) N215-3
Camp2a
Grt2a
(k)
5 mm
(l) B214-10
Ky2a
Ilm2
(m)
Ky2a
Bt2a
5 mm
(k) N215-3
Camp2a
Camp2a
Bt2b
Grt2a
500 µm
(m) B214-10
Ilm2a
Bt2a
Ky2a
500 µm
(o) D113-21
Qz
Chl3
Camp2a
Ms3
500 µm

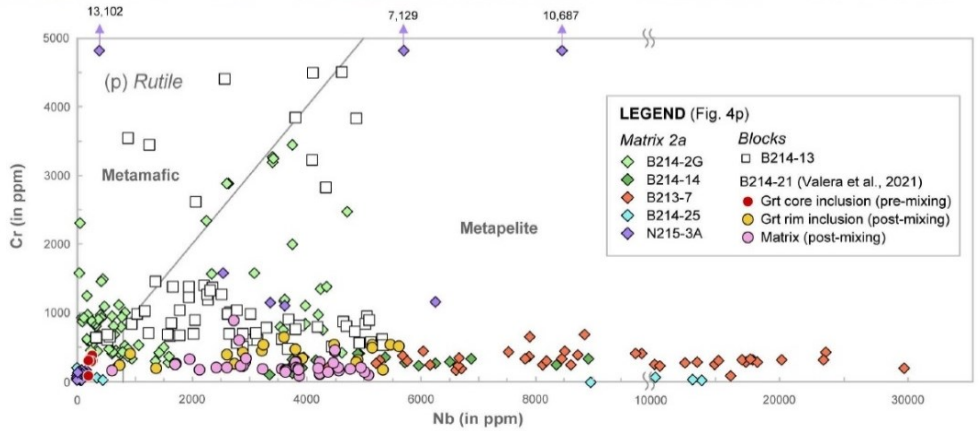

Fig. 2.4. Photomicrographs and compositional map of matrix samples. a) Hornblende-rich sample B214-25 which contain b) Coarse garnet with subtle prograde zonation in contrast to the pronounced zonation in garnet amphibolite blocks (Valera et al., 2021). c) Kyanite (Ky2a) in the matrix in textural equilibrium with hornblende (Camp2a) and ilmenite (Ilm2a). d) Aluminosilicate-rich matrix sample B214-2G where e) Garnet (Grt2a), kyanite (Ky2a), and staurolite (St2a) coexist with hornblende and biotite (Bt2a). f) Hornblende-free, garnet-rich matrix sample B213-7 composed exclusively of g) kyanite, fine euhedral garnet and ilmenite. Surrounding these Stage 2 minerals are replacement phases such as chlorite (Chl3) and muscovite (Ms3). h–k) Matrix samples containing both matrix2a and matrix2b. i) B214-29 only consist of kyanite (Ky2a) and amphibole (Camp2) while k) N215-3 also contain coarse garnet porphyroclasts and finer euhedral garnet grains included in hornblende. l) Metapelitic-looking matrix sample B214-10 composed almost exclusively of m) Biotite, ilmenite, and relatively unaltered coarse kyanite. n) Hornblende-rich matrix sample D113-21, extensively affected by Stage 3 retrograde metamorphism. o) Fine muscovite pseudomorph after kyanite. All photomicrographs are in plane polarized light, except i, k, m, and o which are in crossed polarized light. p) Cr-Nb contents of rutile in matrix2a and some block samples showing mixed metapelite-metamafic signatures. Metapelite and metamafic fields are from Meinhold et al. (2008). Some metamafic blocks exhibit enriched LREEs and Th concentration and are labelled as "Sedimentary" signature. Rutile with high Nb content are also found in such samples (e.g. B214-13).

2.6 Results

2.6.1 Whole-rock geochemistry: Blocks

The metamafic blocks which vary from amphibolite, Grt amphibolite and to Ep amphibolites show basaltic andesite (D113-15; SiO_2 = 54 wt.%) to basaltic (other samples; SiO_2 <49 wt.%) composition. The mafic crust of the CPO has similar SiO_2 content. As mentioned above, earlier works on the petrogenesis of the metamafic blocks suggest its genetic relationship with the mafic crust of the CPO (e.g. Keenan et al., 2016). In order to constrain the effects of magmatic differentiation possibly inherited by the metamafic blocks from their basaltic protoliths, binary plots with FeO*/MgO (FeO* = total Fe as FeO) as the fractionation index (i.e. Fenner diagrams) are constructed (Fig. 2.5). The metamafic blocks along with the mafic crust of the central Palawan

Ophiolite exhibit decreasing CaO (Fig. 2.5a), MgO (Fig. 2.5b), Ni (Fig. 2.5c), and Cr (Fig. 2.5d) contents and increasing Al_2O_3, TiO_2 (Fig. 2.5e), FeO* (Fig. 2.5f), Y (Fig. 2.5g), and Zr (Fig. 2.5h) concentrations with increasing FeO*/MgO.

There is no systematic difference between the metamafic blocks although the amphibolites generally have higher MgO, Cr, Ni and lower FeO* and TiO_2 contents at a given FeO*/MgO ratio compared to garnet- and epidote-bearing varieties (Fig. 2.5). In the Zr-Ti-Y tectonic discrimination diagram, most of the amphibolites from earlier works plot in the MORB field together with the mafic crust of the CPO (Fig. 2.5i). Metamafic blocks sampled in this study, on the other hand, exhibit a more variable signature. A distinct group of the amphibolites, labelled gabbroic protolith in Fig. 2.5, have low Zr contents and plot outside all tectonic fields. These metamafic blocks with low Zr contents (e.g. D113-8 and D113-15) have higher Al_2O_3 and CaO and lower Ni and Y concentrations compared to other blocks.

In the rare earth element (REE) diagrams, most metamafic blocks have flat patterns and similar concentrations as the mafic crust of the central Palawan Ophiolite (Fig. 2.6a–c). There is also no systematic difference in the REE patterns among the different amphibolite types, i.e. Ep amphibolite and Grt amphibolite, although one amphibolite block (D113-11) exhibits slight depletion in middle (MREE) to heavy rare earth elements (HREE; Fig. 2.6b). The low-Zr metamafic blocks (e.g. D113-8 and D113-15) also have the lowest REE concentrations (Fig. 2.6a–c). Their LREEs are also slightly depleted such as in the amphibolite block B213-04 (La_N/Sm_N = 0.48) and a distinct positive Eu anomaly (Eu/Eu* = 3.08) is notable. One sample of each amphibolite type, i.e. the Ep amphibolite (B214-7E), amphibolite (B214-13), and Grt amphibolite (B213-9) blocks are also enriched in LREEs. These blocks either contain a relict metasedimentary domain or are found adjacent to the surrounding matrix (see section 2.5.1).

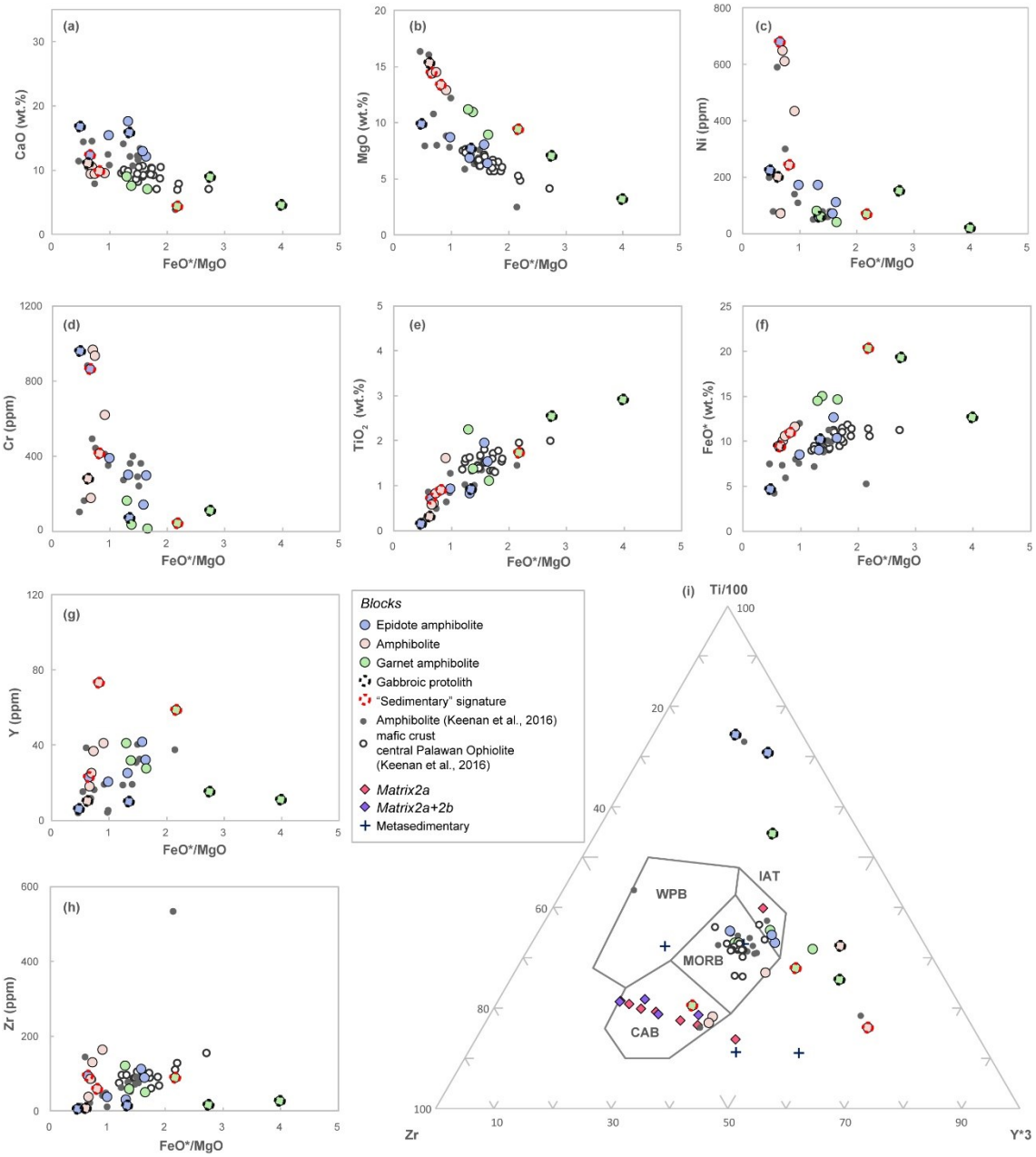

Fig. 2.5. a–h) Binary plots against FeO*/MgO of the mafic crust of central Palawan Ophiolite (Keenan et al., 2016) and Dalrymple Amphibolite (this study and Keenan et al., 2016). Compatible elements such as a) CaO, b) MgO, c) Ni, and d) Cr of the amphibolite and mafic crust of the central Palawan Ophiolite show decreasing trend with increasing differentiation (increasing FeO*/MgO). Tholeiitic signature is also preserved in these lithologies as increasing e) TiO_2 and f) FeO* with increasing FeO*/MgO. Incompatible elements g) Y and h) Zr show a positive slope which is consistent with magmatic differentiation trends while amphibolites derived from gabbroic cumulates recorded the lowest concentrations. See text for details. FeO* = Total Fe as FeO. i) Zr-Ti-Y tectonic discrimination diagram (after Pearce and Cann, 1971). Most amphibolite of Keenan et al. (2016) and mafic crust of the central Palawan ophiolite plot within the MORB field, while amphibolites from this study exhibit more extensive variability. Metasedimentary blocks and matrix samples have distinctly higher Zr content. The fields are as follows: IAT – island arc tholeiites, WPB – within plate basalts, MORB – mid oceanic ridge basalts and CAB – calc-alkaline basalts.

The metamafic blocks and the mafic crust of the CPO also generally show similar trends in the extended trace element spidergram (Fig. 2.6d–f). This include enrichments in fluid mobile elements such as Rb, Ba, U, Pb and Sr. Some notable difference between the metamafic blocks and the mafic crust of the CPO is the enrichment in Nb and Ta in the former (Fig. 2.6). The low-Zr metamafic blocks also have lower trace element concentration than the other metamafic blocks. They also exhibit positive Sr anomaly not seen in the other amphibolite and Grt amphibolite blocks. The low-Zr Grt amphibolite blocks (i.e. D113-14G, D113-15) also show positive Ti anomaly. The LREE-enriched metamafic blocks exhibit marked enrichment in Th, Nb, Ta. A negative Ti anomaly was observed in the Ep amphibolite and amphibolite blocks.

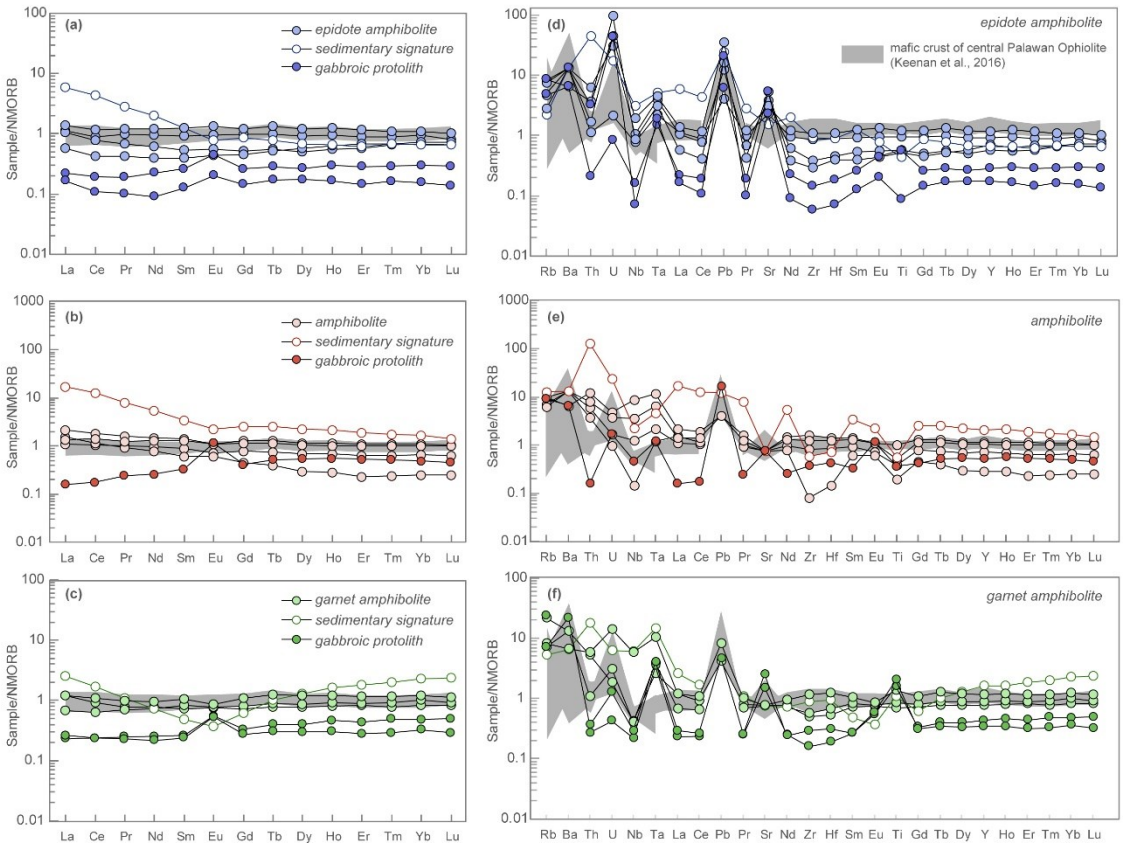

Fig. 2.6. Trace element data of the metamafic blocks. a–c are normal mid-oceanic ridge basalt (NMORB)-normalized rare earth element (REE) plots of a) epidote amphibolite b) amphibolite, and c) garnet amphibolite blocks of the Dalrymple Amphibolite. Fig. d–f are NMORB-normalized extended trace element diagram of d) epidote amphibolite, e) amphibolite and f) garnet amphibolite blocks. Shown as open symbols are samples with sedimentary signature while darker shades are used for amphibolite blocks derived from a gabbroic protolith (see text for details). Also shown as grey fields are the data for the mafic crust of central Palawan Ophiolite from Keenan et al. (2016).

2.6.2 Whole-rock geochemistry: Matrix and metasedimentary blocks

Samples which consist of matrix2a alone and those including both matrix2a and 2b do not exhibit systematic difference in whole-rock major and trace elements compositions (Fig. 2.7a–f). The matrix surrounding the blocks exhibit variable phase assemblage as well as distinct geochemical characteristics compared with the metamafic blocks. The Al_2O_3 (Fig. 2.7a) and Zr contents of the matrix increase with their TiO_2 concentration and are generally higher compared to the metamafic and metasedimentary blocks (Fig. 2.7a). Direct correlation is also found between their Cr content and whole-rock Mg# (Fig. 2.7b) and La vs Th (Fig. 2.7c) concentrations of the matrix samples. Distinct signatures are observed for more fluid-mobile elements in the matrix samples. Their CaO (Fig. 2.7d) and SiO_2 (Fig. 2.7e) concentrations are generally lower at a given FeO*/MgO ratio compared to the metamafic blocks while K_2O, Ba and Rb contents of the matrix are higher (Fig. 2.7f). The latter group of elements also exhibit positive correlation with each other (Fig. 2.7f). The concentrations of these three elements (K_2O, Ba and Rb) in the matrix samples are linked to the degree of Stage 3 replacement in the matrix. For example, the matrix 2a D113-21 with kyanite grains completely replaced by fine pseudomorphic muscovite (Ms3; Fig. 2.4n, o) have higher K_2O, Ba and Rb contents than B214-2G (Fig. 2.4d, e) which largely preserves its aluminosilicates (e.g. kyanite and staurolite).

Except for the metacarbonate block B214-7C, the metasedimentary blocks generally exhibit the same trends in terms of major oxide concentrations as the matrix surrounding them. The Cr (= 28–1045 ppm) and Ni (= 71–632 ppm) contents of the matrix samples are comparable with the metamafic blocks (Cr = 14–966 ppm; Ni = 20–680 ppm) at a given FeO*/MgO (Fig. 2.7b). These values are higher than the metasedimentary blocks (Cr = 49–459 ppm; Ni = 51–174 ppm) but are much lower than the overlying ultramafic rocks of the Palawan Ophiolite (Cr = 1528–3072 ppm; Ni = 1045–2499 ppm).

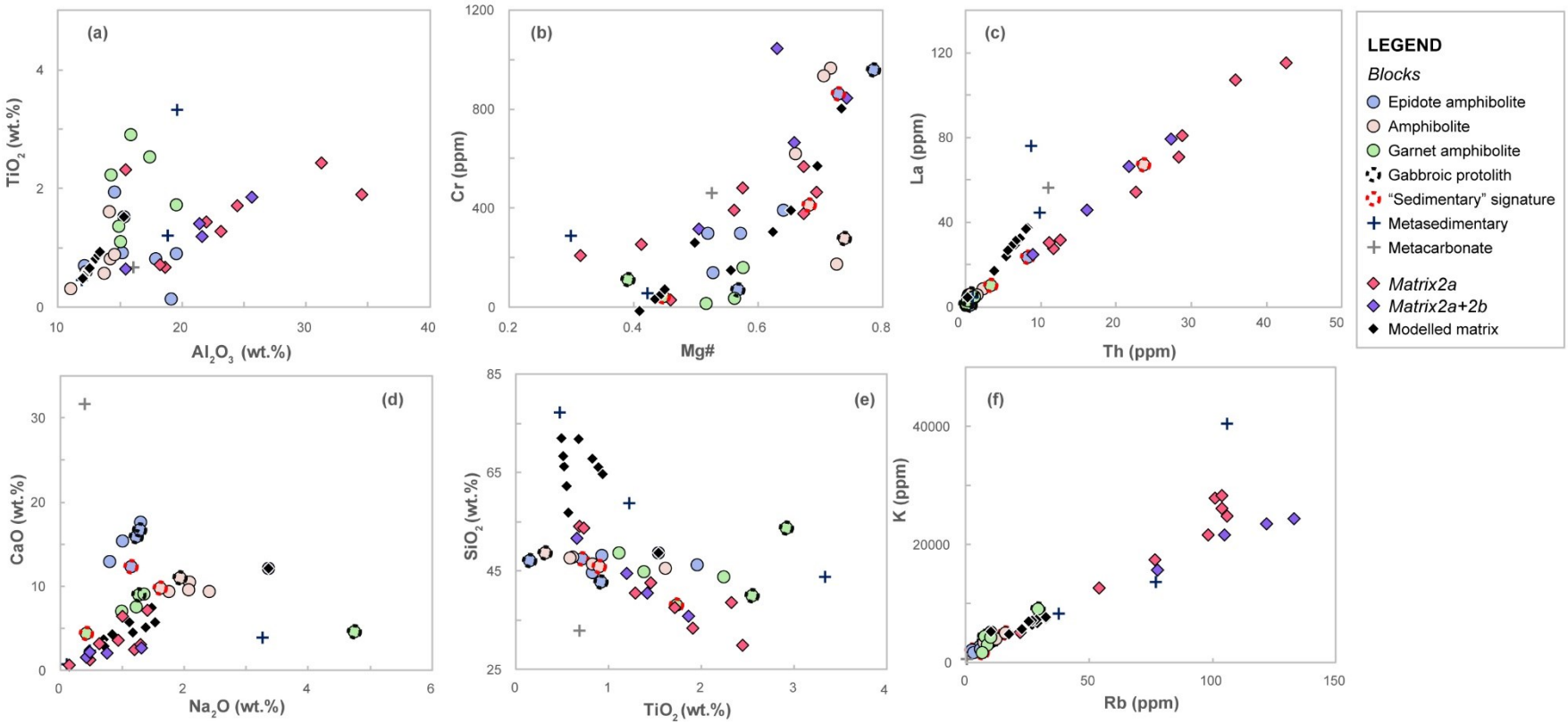

Fig. 2.7. a–f) binary plots of whole-rock composition of matrix and block samples. The modelled matrix composition is also shown as black diamonds. a) The matrix samples show positive correlation in their Al_2O_3 vs. TiO_2, b) Cr vs Mg#, and c) La vs Th compositions. The measured matrix compositions have notably higher Al_2O_3, La, and Th contents compared to the modelled matrix and the block samples. d) The measured matrix compositions generally have less CaO and Na_2O compared to the metamafic blocks. e) Slight differences in major oxide contents of the two metamafic end-members (metamafic2A and 2EA) inevitably result to distinct trends for the modelled matrix. Regardless of the metamafic end-member used however, both arrays of modelled matrix compositions predict an originally higher SiO_2 content in contrast to the generally depleted SiO_2 of the measured matrix. f) The matrix samples have higher K_2O, Rb, and Ba (not shown) than the amphibolite blocks and the modelled matrix.

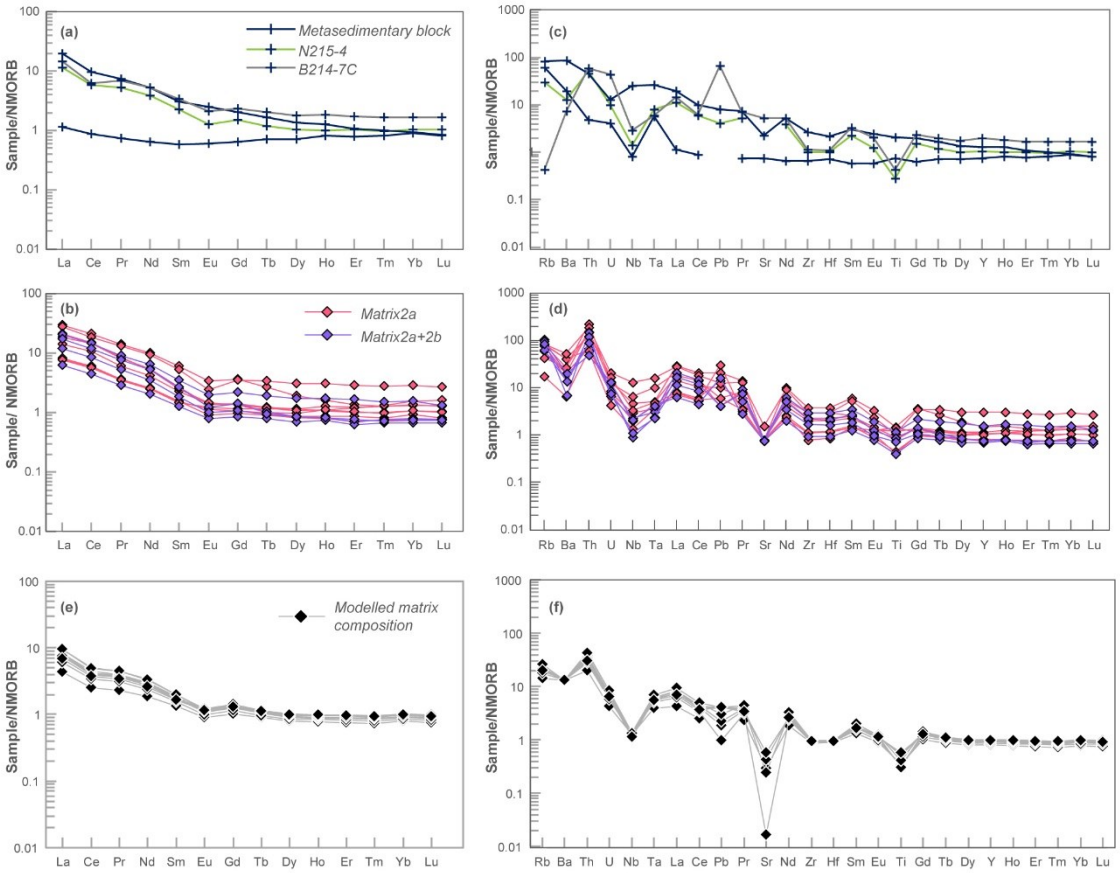

Fig. 2.8. a, b) NMORB-normalized REE and c,d) extended trace element plots of a,b) metasedimentary blocks, c,d) measured matrix compositions. The metasedimentary block N215-4 exhibits similar REE and trace element patterns as the matrix samples characterized by negative anomaly in Eu, Ba, Nb, Sr and Ti. The same trends are also replicated in the modelled matrix composition. e, f) REE and extended trace element plot of the modelled matrix composition.

The REE contents of the metasedimentary block and matrix samples normalized to NMORB (Hofmann, 1988) are shown in Fig. 2.8a and b. In contrast to most metamafic blocks, all matrix samples exhibit elevated LREEs ($(La_N/Sm)_N$ = 4.90–8.33). All samples also show a negative Eu anomaly (Eu/Eu* = 0.55–0.96; Eu* = $(Sm*Gd)^{1/2}$). Similar to the metamafic blocks however, the M-HREEs of the matrix samples are flat. The metasedimentary blocks, aside from B214-26, shows the same elevated LREEs and flat M-HREEs as the matrix (Fig. 2.8a). The Ky-Ilm-Grt quartzite (N215-4) block shows the same slightly negative Eu anomaly (Fig. 2.8a). The metasedimentary block sample B214-26 exhibits a flat REE trend with concentrations comparable to NMORB.

In contrast to the metamafic blocks, the matrix samples and the metasedimentary block N215-4 both record negative Ba, Nb, Sr, and Ti anomalies in the extended trace element spidergram (Fig. 2.8c,d). The metacarbonate block B214-7C exhibits distinct trends relative to other metasedimentary blocks such as depletion in Rb, and enrichments in Th, U, and Pb (Fig. 2.8c). In the extended trace element spidergram, both matrix2a only and matrix2a-2b samples show the same trend characterized by elevated incompatible elements i.e. Rb, Ba, Th, U (Fig. 2.8d) and depletion in Nb and Ta.

2.6.3 Correlation coefficient (*r*)

In order to distinguish the effects of mechanical mixing, fluid advection and other controls on the petrological characteristics of the matrix samples, the procedural work flow illustrated in Fig. 2.9 was used. First, Pearson product-moment coefficient of correlation (*r*) was applied (Sachs, 1984). This calculation measures the strength of linear association among the suite of major and trace elements and helps identify which elements behave similarly, i.e. exhibit strong positive correlation with one another. The correlation coefficients shown as matrices in Table 2.4 are based on the expression:

$$r = \frac{n\sum(xy) - \sum(x)\cdot\sum(y)}{\sqrt{[n((\sum x^2) - (\sum x)^2)]\cdot[n((\sum y^2) - (\sum y)^2)]}} \qquad \text{(Eqn. 1)}$$

where n (= 12) represents the number of matrix samples and x, y variables are the concentration of the elements being correlated. A 5% significance level limit of r = 0.497 for a degree of freedom (DF) of 10 (DF = $n-2$) was used (Sachs, 1984).

If advection is the dominant process, elements mobilized by the fluids should either exhibit systematic enrichment or depletion in the affected rocks, depending on the stability of sink minerals of such elements. Fluid-immobile elements however, will not be affected and will remain in the rock. Their concentration in the rock will thus change systematically depending on whether fluid-mobile elements are added or removed from the rock volume (Gresens, 1967; Grant, 1986). Meanwhile, if mechanical mixing is prevalent then at least two groups of elements should emerge, each

representing an end-member component. It is however possible that both processes coupled by other factors, e.g. phase assemblage control, could have affected the matrix samples. In order to address this possibility, the correlation coefficient among fluid-immobile elements is investigated.

Based on the calculated correlation coefficients (Fig. 2.10a, Table 2.4), at least two groups of fluid-immobile elements are identified. Group 1 elements include TiO_2, Al_2O_3, Zr, Th and LREEs (triangle symbols in Fig. 2.10a). The concentration of Th, Zr and the LREEs in the matrix samples in particular show very high correlation coefficients, e.g. correlation coefficient between Th and La (Th-La) is $r = 0.99$. These group of elements exhibit strong negative correlation with the whole-rock Mg#, SiO_2 and Na_2O contents of the matrix samples (Fig. 2.10a). Group 2 (cross symbols in Fig. 2.10a) includes Cr, Ni (Cr-Ni correlation coefficient $r = 0.88$) and MgO which are all negatively correlated with the TiO_2 (e.g. Cr-TiO_2 $r = -0.72$) and FeO* (e.g. Cr-FeO* $r = -0.65$) contents of the matrix samples (Fig. 2.10a).

The distinct grouping of these elements suggest end-member components contributing to the chemistry of the matrix samples. In particular, the context of a slab-mantle wedge interface for the Dalrymple Amphibolite (Valera et al., 2021) suggests the possibility of mechanical mixing among crustal (sedimentary and mafic) lithologies from the subducting slab and/or an ultramafic end-member from the hanging wall. This information will be used in identifying the end-members and mixing ratio estimation discussed below. Two more groups of elements which also exhibit positive linear correlation with one another are identified. Group 3 includes MnO (circles in Fig. 2.10a) which is strongly correlated with the Nb, Ta and the HREEs of the matrix. Group 4 is the large ion lithophile elements: K_2O, Ba and Rb (triangles in Fig. 2.10a).

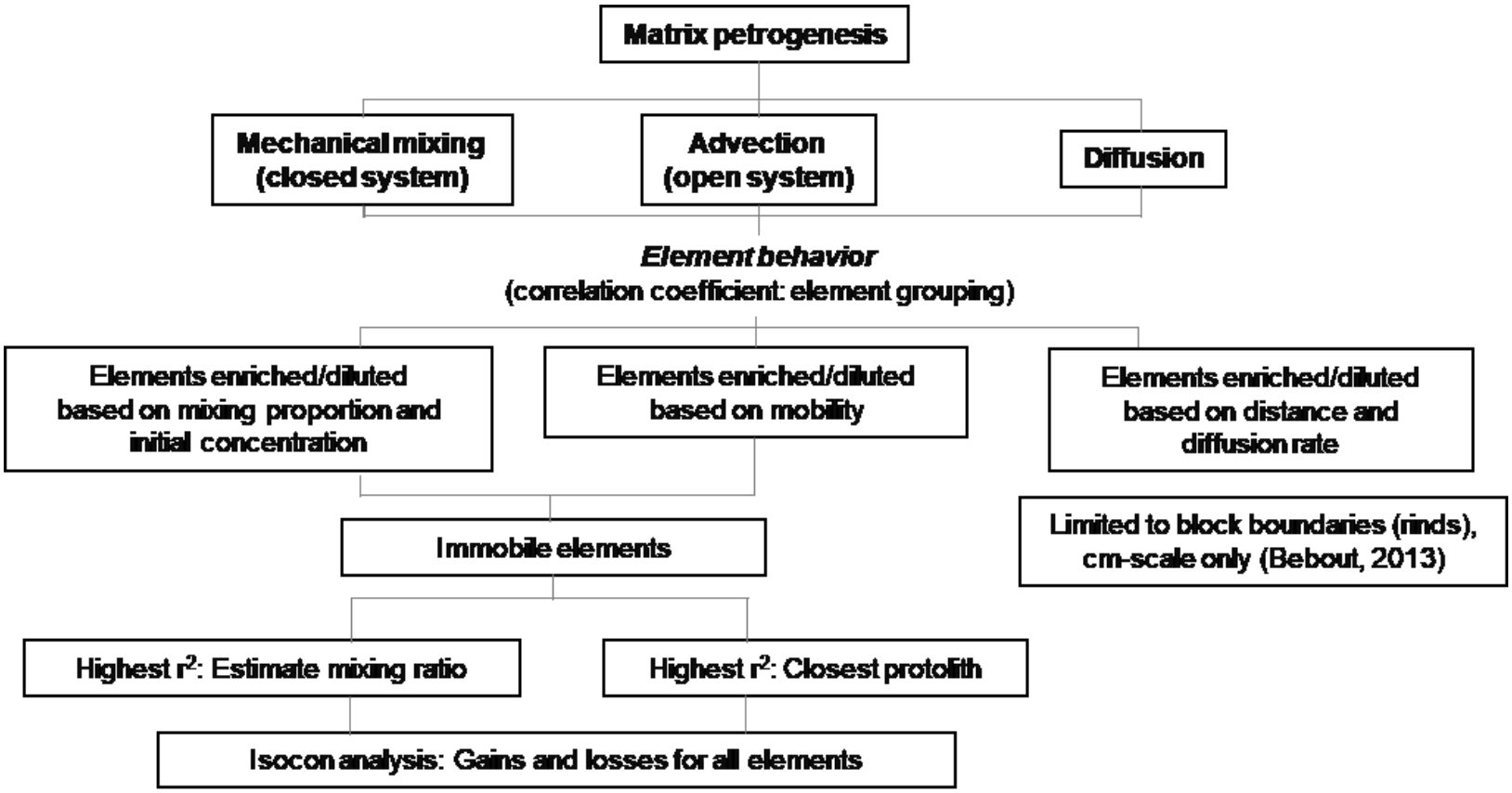

Fig. 2.9 Schematic diagram showing the procedural work flow employed in this study to distinguish the effects of mixing and advection which may have controlled the whole-rock chemistry of the matrix. Diffusion was not considered due to sampling limitations. Its effect however would likely be limited in scale (Bebout, 2013) and restricted to rind formation along block/matrix boundaries. The first step is to find groups of elements which behave similarly through the correlation coefficient among the elements. If mixing is dominant, then distinct groups of elements representative of end-member components will exhibit strong correlation with one another. If advection is prevalent, fluid mobile elements should behave similarly and exhibit strong positive correlation with one another while showing negative or no correlation with fluid-immobile elements. By fitting the measured concentration of immobile elements in the matrix with a hypothesized original composition, we can either estimate the mixing ratio between end-member components if mixing occurred, or the closest protolith prior to metasomatism if advection is the dominant process. Finally, mass balance calculation (Isocon analysis) was done to quantify relative gains and losses in elements incurred by the matrix samples if infiltrating fluids caused changes in the concentration of these elements relative to the original matrix composition.

Table 2.4. Correlation matrices for the measured matrix composition in Table 2.3

	SiO_2	TiO_2	Al_2O_3	FeO*	MnO	MgO	CaO	Na_2O	K_2O	P_2O_5	Cr	Ni	Rb	Ba	Th	U	Nb	Ta	La	Ce	Pb	Pr	Sr	Nd	Zr	Hf	Sm	Eu	Gd	Tb	Dy	Y	Ho	Er	Tm	Yb	Lu
SiO_2	1.00																																			
TiO_2	0.86	1.00																																		
Al_2O_3	0.58	0.31	1.00																																	
FeO*	0.78	0.92	0.25	1.00																																
MnO	0.05	0.03	0.01	0.01	1.00																															
MgO	0.25	0.29	0.47	0.27	0.00	1.00																														
CaO	0.04	0.00	0.31	0.01	0.00	0.07	1.00																													
Na_2O	0.56	0.36	0.62	0.42	0.07	0.21	0.45	1.00																												
K_2O	0.00	0.08	0.13	0.04	0.01	0.04	0.43	0.08	1.00																											
P_2O_5	0.39	0.24	0.38	0.18	0.39	0.10	0.16	0.28	0.12	1.00																										
Cr	0.32	0.52	0.12	0.42	0.00	0.40	0.06	0.02	0.07	0.05	1.00																									
Ni	0.22	0.51	0.05	0.41	0.02	0.41	0.11	0.03	0.17	0.00	0.78	1.00																								
Rb	0.00	0.06	0.13	0.02	0.00	0.00	0.59	0.15	0.79	0.10	0.15	0.27	1.00																							
Ba	0.01	0.04	0.01	0.09	0.24	0.03	0.00	0.02	0.35	0.17	0.00	0.00	0.05	1.00																						
Th	0.64	0.42	0.66	0.28	0.11	0.27	0.05	0.30	0.07	0.73	0.17	0.06	0.05	0.10	1.00																					
U	0.05	0.00	0.24	0.01	0.38	0.09	0.07	0.05	0.18	0.41	0.01	0.00	0.09	0.43	0.29	1.00																				
Nb	0.09	0.06	0.08	0.00	0.61	0.04	0.03	0.01	0.05	0.47	0.07	0.05	0.01	0.50	0.40	0.58	1.00																			
Ta	0.03	0.02	0.02	0.00	0.59	0.01	0.08	0.00	0.01	0.32	0.06	0.05	0.00	0.46	0.26	0.54	0.96	1.00																		
La	0.61	0.41	0.55	0.26	0.17	0.17	0.04	0.29	0.05	0.79	0.14	0.04	0.05	0.09	0.97	0.28	0.45	0.31	1.00																	
Ce	0.65	0.43	0.64	0.27	0.12	0.21	0.05	0.32	0.05	0.74	0.15	0.05	0.05	0.07	0.99	0.28	0.39	0.26	0.99	1.00																
Pb	0.18	0.14	0.01	0.08	0.02	0.06	0.14	0.03	0.38	0.00	0.02	0.01	0.27	0.18	0.02	0.03	0.00	0.01	0.03	0.04	1.00															
Pr	0.61	0.42	0.54	0.29	0.21	0.19	0.07	0.32	0.07	0.86	0.14	0.05	0.06	0.10	0.96	0.31	0.46	0.31	0.99	0.97	0.02	1.00														
Sr	0.03	0.01	0.01	0.00	0.91	0.00	0.00	0.04	0.08	0.42	0.00	0.01	0.03	0.43	0.16	0.41	0.79	0.75	0.22	0.16	0.00	0.26	1.00													
Nd	0.60	0.43	0.53	0.31	0.21	0.21	0.08	0.32	0.08	0.88	0.14	0.05	0.07	0.10	0.94	0.29	0.44	0.28	0.97	0.94	0.01	0.99	0.26	1.00												
Zr	0.67	0.39	0.79	0.29	0.06	0.27	0.18	0.48	0.12	0.68	0.12	0.02	0.14	0.03	0.93	0.24	0.24	0.12	0.90	0.94	0.02	0.89	0.08	0.88	1.00											
Hf	0.66	0.40	0.79	0.30	0.07	0.29	0.18	0.47	0.13	0.69	0.13	0.03	0.14	0.04	0.94	0.24	0.26	0.13	0.91	0.95	0.01	0.90	0.09	0.89	1.00	1.00										
Sm	0.52	0.39	0.44	0.31	0.23	0.22	0.09	0.28	0.11	0.91	0.13	0.05	0.09	0.13	0.87	0.29	0.44	0.28	0.90	0.86	0.00	0.95	0.30	0.98	0.79	0.81	1.00									
Eu	0.55	0.50	0.39	0.43	0.08	0.33	0.05	0.21	0.07	0.71	0.25	0.13	0.05	0.08	0.80	0.16	0.30	0.16	0.79	0.76	0.02	0.83	0.14	0.87	0.70	0.73	0.92	1.00								
Gd	0.46	0.38	0.31	0.31	0.29	0.21	0.06	0.23	0.11	0.86	0.16	0.08	0.08	0.16	0.76	0.26	0.50	0.33	0.80	0.74	0.01	0.87	0.39	0.91	0.66	0.68	0.97	0.91	1.00							
Tb	0.34	0.29	0.19	0.23	0.44	0.14	0.02	0.16	0.10	0.78	0.14	0.09	0.06	0.22	0.62	0.27	0.63	0.47	0.68	0.61	0.01	0.75	0.59	0.79	0.50	0.53	0.86	0.76	0.95	1.00						
Dy	0.31	0.26	0.15	0.20	0.55	0.10	0.01	0.15	0.08	0.67	0.15	0.11	0.05	0.23	0.52	0.27	0.70	0.55	0.59	0.52	0.00	0.66	0.71	0.67	0.41	0.44	0.73	0.61	0.84	0.96	1.00					
Y	0.24	0.21	0.10	0.14	0.68	0.07	0.00	0.12	0.06	0.57	0.15	0.13	0.03	0.27	0.40	0.31	0.76	0.64	0.48	0.41	0.00	0.53	0.82	0.54	0.30	0.32	0.58	0.44	0.69	0.86	0.96	1.00				
Ho	0.28	0.25	0.12	0.17	0.63	0.08	0.00	0.14	0.05	0.57	0.17	0.14	0.03	0.22	0.43	0.28	0.73	0.61	0.51	0.44	0.00	0.56	0.77	0.57	0.33	0.36	0.60	0.47	0.71	0.87	0.97	0.99	1.00			
Er	0.29	0.26	0.14	0.18	0.64	0.10	0.00	0.16	0.05	0.50	0.20	0.18	0.02	0.21	0.41	0.29	0.72	0.61	0.47	0.41	0.01	0.52	0.76	0.52	0.32	0.34	0.54	0.41	0.64	0.80	0.93	0.98	0.99	1.00		
Tm	0.31	0.28	0.15	0.19	0.68	0.10	0.00	0.18	0.03	0.49	0.22	0.21	0.01	0.19	0.38	0.31	0.70	0.59	0.43	0.38	0.02	0.48	0.76	0.48	0.30	0.32	0.50	0.36	0.59	0.75	0.88	0.96	0.96	0.99	1.00	
Yb	0.32	0.29	0.17	0.19	0.67	0.12	0.00	0.19	0.03	0.47	0.25	0.23	0.01	0.21	0.38	0.34	0.70	0.60	0.43	0.39	0.02	0.48	0.74	0.47	0.30	0.32	0.48	0.35	0.56	0.71	0.84	0.93	0.93	0.97	0.99	1.00
Lu	0.35	0.30	0.22	0.20	0.69	0.15	0.00	0.22	0.03	0.50	0.24	0.23	0.01	0.21	0.41	0.40	0.71	0.61	0.45	0.41	0.03	0.50	0.73	0.49	0.33	0.34	0.50	0.35	0.56	0.69	0.81	0.89	0.89	0.93	0.97	0.99	1.00

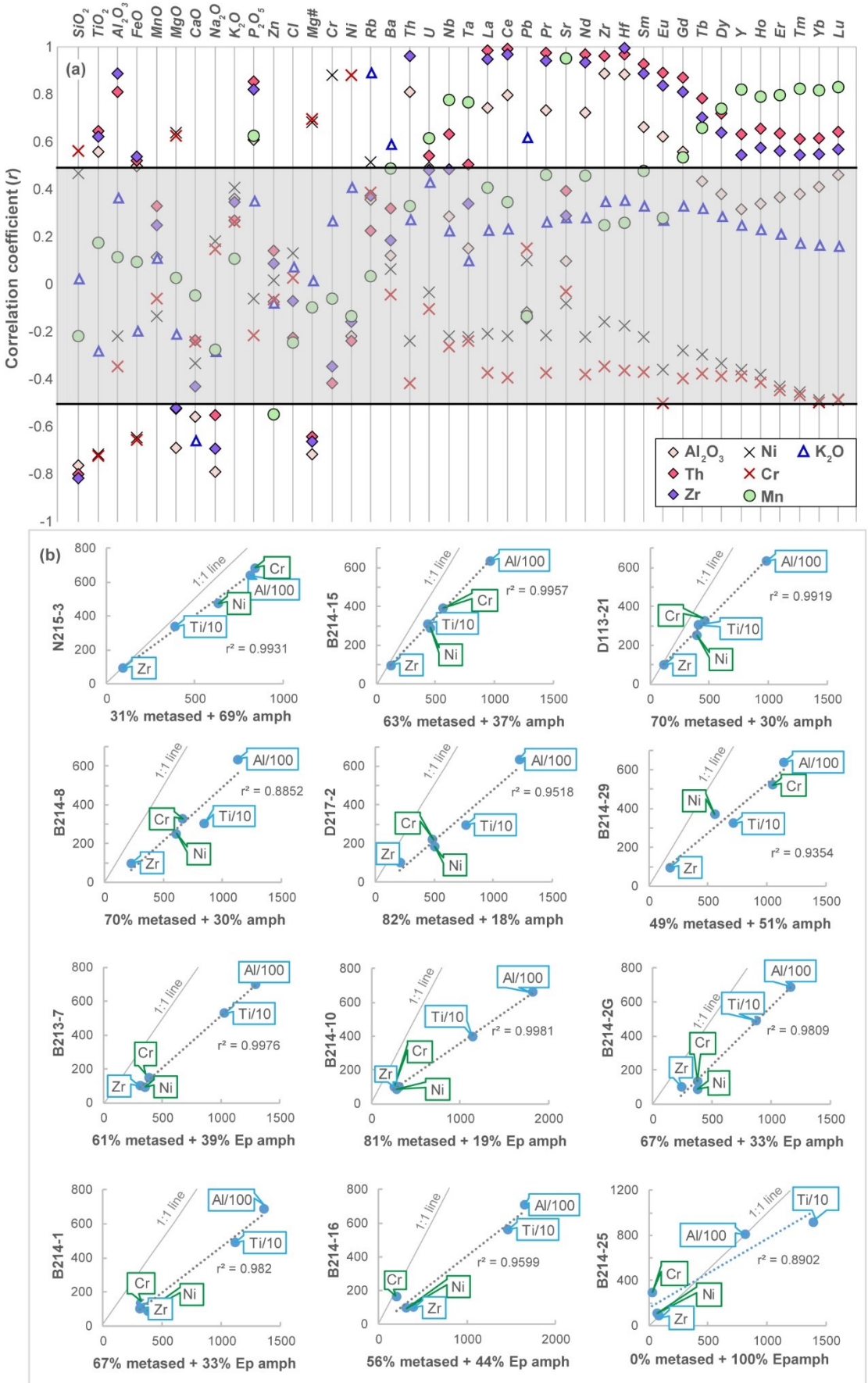
(a)
Correlation coefficient (r)
SiO2 TiO2 Al2O3 FeO MnO MgO CaO Na2O K2O P2O5 Zn Cl Mg# Cr Ni Rb Ba Th U Nb Ta La Ce Pb Pr Sr Nd Zr Hf Sm Eu Gd Tb Dy Y Ho Er Tm Yb Lu
Al2O3 Ni K2O
Th Cr
Zr Mn
(b)
N215-3
31% metased + 69% amph
r² = 0.9931
B214-15
63% metased + 37% amph
r² = 0.9957
D113-21
70% metased + 30% amph
r² = 0.9919
B214-8
70% metased + 30% amph
r² = 0.8852
D217-2
82% metased + 18% amph
r² = 0.9518
B214-29
49% metased + 51% amph
r² = 0.9354
B213-7
61% metased + 39% Ep amph
r² = 0.9976
B214-10
81% metased + 19% Ep amph
r² = 0.9981
B214-2G
67% metased + 33% Ep amph
r² = 0.9809
B214-1
67% metased + 33% Ep amph
r² = 0.982
B214-16
56% metased + 44% Ep amph
r² = 0.9599
B214-25
0% metased + 100% Epamph
r² = 0.8902
1:1 line
Al/100
Ti/10
Cr
Ni
Zr

Fig. 2.10. a) coefficient of correlation showing the similarity in behavior of distinct groups of elements/components comprising the matrix samples. The values are given in Table 2.4. In particular, the strong correlation among Cr, Ni, and Mg suggest a metamafic end-member while the Al_2O_3, Th, and Zr contents of the matrix are strongly correlated with its LREE content indicating a metasedimentary end-member. The strong correlation of MnO with HREE content of the matrix meanwhile indicates strong control of certain minerals (e.g. garnet) in the chemistry of the matrix. Positive correlation between K_2O, Rb, and Ba on the other hand is related to the growth and abundance of Stage 3 replacement phases in the matrix samples. b) Fitting results between measured matrix composition (*y*-axis) and varying ratios of metasedimentary (N215-4) and metamafic (D113-9 and D113-5) blocks in the *x*-axis. The metased:metamafic ratio with the highest r^2 was used to determine the concentration of other elements resulting to the modelled matrix composition.

2.6.4 Mixing ratio estimation

Regression analysis was performed to identify the most likely end-members controlling the concentration of Groups 1 and 2 elements/components in the matrix samples and the mixing proportion of these end-members. This was done by fitting the concentration of Cr, Ni, Zr, TiO_2, and Al_2O_3 (assumed to be immobile) of the measured and modelled matrix compositions using least squares method (Figs. 2.4; 2.10b). The modelled matrix composition was obtained by changing the end-members used and their relative proportions. The combination of end-members and corresponding mixing proportion with the highest coefficient of determination for linear regression (r^2) was then utilized to calculate the concentration of other elements in the modelled matrix.

The high values of Group 1 elements in the matrix samples, especially Zr, Th and the LREEs, suggest a metasedimentary end-member. A possible end-member, the Ky+Ilm+Grt quartzite block N215-4, was selected from the metasedimentary blocks, referred hereafter as simply metased1. This is supported by the remarkable similarity in REE and trace element pattern among matrix samples which is the same as the trends in the block sample N215-4 (Fig. 2.8a, c). Other possible sedimentary end-member values such as the North American shale composite (NASC; Gromet et al., 1984), average South China Sea sediment (Li et al., 2003) were considered for metased1 but consistently resulted to lower regression values.

Group 2 elements/components (Cr, Ni and MgO) can indicate either a mafic or an ultramafic end-member. An ultramafic end-member is not considered since such an end-member is inconsistent with the following lines of evidence: 1. Neither blocks of ultramafic composition nor highly Mg-rich matrix, i.e. dominated by serpentine+talc+Mg-chlorite was observed in the Dalrymple Amphibolite; 2. The dunite-harzburgite interlayers overlying the Dalrymple Amphibolite are relatively fresh with the serpentine phases replacing some olivine and pyroxenes in the ultramafic rocks being predominantly low-*T* species (e.g. chrysotile and lizardite); 3. The *P-T-D* conditions of the Dalrymple Amphibolite are above the stability field of serpentine (Valera et al., 2021). Numerical modelling (Gerya et al., 2002; Agard et al., 2016) revealed that deformation and incorporation of basalts rather than "fresh" unserpentinized mantle material as matrix material is most likely at these *P-T* conditions due to the rheological strength of the latter relative to the former.

The end-member likely controlling Group 2 elements/components was therefore selected from the amphibolites, Ep- and Grt amphibolite blocks, the average central Palawan Ophiolite basalt (data from Encarnacion et al., 1995 and Keenan et al., 2016), and the average normal MORB (NMORB; Hofmann, 1988). The highest regression values are obtained when the amphibolite block D113-9 (metamafic2A) is used as end-member for some samples (Table 2.5) and the Ep amphibolite D113-5 (metamafic2EA; Table 2.5) for others (Fig. 2.10b). We selected the metamafic end-member with the highest regression value depending on the matrix samples (Table 2.5).

In order to account for the difference in the concentration between the major oxides and trace elements, which affects the regression value vis-à-vis the proportion between end-members, the ratios Ti/10 and Al/100 were utilized. The metased1: metamafic2(A or EA) ratio with the highest coefficient of determination for linear regression (r^2) is then used to obtain the complete set of modelled composition of the matrix sample given in Table 2.5. These modelled values are interpreted to correspond to the original composition of the matrix samples which was subsequently affected by infiltrating fluids as discussed in more detail in the Discussion section. These modelled values were thus used as the 'original' composition in the mass balance calculation (isocon analysis).

Table 2.5. Calculated major and trace element data of matrix in Dalrymple Amphibolite

Metamafic2a: Amphibolite (D113-9)						
_%metased1	31	67	70	49	70	82
Sample	N215-3	B214-15	D113-21	B214-29	B214-08	D217-2
in wt.%						
SiO_2	56.91	66.31	68.37	62.20	68.37	71.90
TiO_2	0.56	0.52	0.51	0.54	0.51	0.49
Al_2O_3	12.13	12.02	11.99	12.07	11.99	11.95
Fe_2O_3*	9.43	7.62	7.22	8.41	7.22	6.54
MnO	0.40	0.41	0.41	0.40	0.41	0.42
MgO	10.65	6.65	5.78	8.40	5.78	4.28
CaO	7.48	4.34	3.65	5.71	3.65	2.47
Na_2O	1.47	0.83	0.70	1.11	0.70	0.46
K_2O	0.58	0.77	0.81	0.69	0.81	0.89
P_2O_5	0.11	0.22	0.24	0.17	0.24	0.28
Total	99.72	99.70	99.70	99.71	99.70	99.69
in ppm						
Cr	683.57	392.22	328.49	519.69	328.49	219.23
Ni	473.54	291.44	251.61	371.11	251.61	183.32
Rb	17.69	27.01	29.06	22.93	29.06	32.55
Ba	181.67	181.42	181.37	181.53	181.37	181.27
Th	3.79	6.56	7.17	5.35	7.17	8.21
U	0.30	0.49	0.53	0.40	0.53	0.60
Nb	4.51	4.74	4.79	4.64	4.79	4.88
Ta	0.76	1.13	1.21	0.97	1.21	1.34
La	16.64	29.42	32.22	23.83	32.22	37.01
Ce	30.57	49.23	53.31	41.07	53.31	60.31
Pr	4.83	7.69	8.32	6.44	8.32	9.39
Nd	20.81	31.24	33.52	26.67	33.52	37.43
Zr	92.20	98.60	100.00	95.80	100.00	102.40
Hf	2.68	2.83	2.86	2.77	2.86	2.92
Sm	4.95	6.55	6.90	5.85	6.90	7.50
Eu	1.19	1.42	1.47	1.32	1.47	1.56
Gd	5.16	6.35	6.61	5.83	6.61	7.05
Tb	0.78	0.91	0.94	0.86	0.94	0.99
Dy	5.01	5.69	5.83	5.39	5.83	6.09
Y	29.11	33.05	33.91	31.33	33.91	35.39
Ho	1.05	1.19	1.22	1.13	1.22	1.27
Er	3.15	3.65	3.76	3.43	3.76	3.94
Tm	0.46	0.52	0.54	0.49	0.54	0.56
Yb	3.07	3.53	3.64	3.33	3.64	3.81
Lu	0.45	0.52	0.53	0.49	0.53	0.56

Table 2.5. Continued

Metamafic2EA: Epidote amphibolite (D113-5)					
_%metased1	61	67	67	81	56
Sample	B213-7	B214-2G	B214-1	B214-10	B214-16
in wt.%					
SiO_2	66.11	67.81	67.81	71.79	64.68
TiO_2	0.88	0.82	0.82	0.67	0.94
Al_2O_3	13.23	13.02	13.02	12.54	13.40
Fe_2O_3*	7.88	7.52	7.52	6.67	8.18
MnO	0.33	0.35	0.35	0.38	0.32
MgO	3.73	3.47	3.47	2.86	3.95
CaO	5.15	4.47	4.47	2.87	5.73
Na_2O	1.37	1.18	1.18	0.72	1.53
K_2O	0.85	0.88	0.88	0.93	0.84
P_2O_5	0.27	0.28	0.28	0.31	0.26
Total	99.81	99.79	99.79	99.74	99.83
in ppm					
Cr	149.75	135.23	135.23	101.34	161.86
Ni	92.71	90.89	90.89	86.65	94.23
Rb	27.04	28.69	28.69	32.56	25.66
Ba	181.11	181.12	181.12	181.12	181.11
Th	6.04	6.62	6.62	7.95	5.56
U	0.49	0.52	0.52	0.60	0.46
Nb	4.12	4.26	4.26	4.58	4.01
Ta	1.11	1.18	1.18	1.34	1.05
La	28.65	31.04	31.04	36.62	26.65
Ce	47.28	50.90	50.90	59.34	44.27
Pr	7.51	8.04	8.04	9.30	7.06
Nd	30.47	32.44	32.44	37.05	28.82
Zr	99.96	100.89	100.89	103.06	99.18
Hf	2.85	2.87	2.87	2.93	2.83
Sm	6.45	6.75	6.75	7.45	6.20
Eu	1.53	1.55	1.55	1.61	1.51
Gd	6.61	6.78	6.78	7.18	6.47
Tb	0.98	0.99	0.99	1.02	0.97
Dy	6.20	6.24	6.24	6.34	6.16
Y	35.53	35.85	35.85	36.59	35.27
Ho	1.32	1.32	1.32	1.33	1.31
Er	3.99	4.02	4.02	4.11	3.96
Tm	0.58	0.58	0.58	0.59	0.57
Yb	3.90	3.92	3.92	3.99	3.88
Lu	0.55	0.56	0.56	0.58	0.54

The coefficient of determination for linear regression (r^2) are high ranging from 0.88–0.99 (Fig. 2.10b). The metased1 / (metased1 + metamafic2A or EA) ratios are high, generally above 50% except for N215-3 (31%) and B214-29 (49%; Fig. 2.10b). One matrix sample B214-25, shows the highest r^2 value when the metased1: metamafic2EA ratio is at a minimum, i.e. zero (Fig. 2.10b). The trace element content of this matrix sample, however, exhibit enrichment in LILE (e.g. Th) and LREEs similar to the other matrix samples (Fig. 2.8c, d). The sample is mainly composed of Ca-amphibole with minimal (< 5%) garnet and kyanite partly replaced by muscovite (Fig. 2.4a–c). Compositional maps of the garnet porphyroblasts in this sample (Fig. 2.4b) revealed the same chemical zonation pattern characteristic of garnets in the matrix, i.e. higher Mg# and subtle change in chemistry from core to mantle, in contrast to the garnet porphyroblasts of the blocks (Valera et al., 2021). These contrasting signatures present the limitation of the method applied in this study in estimating the mixing ratio. This sample is not considered further in the isocon analysis since its 'original' composition cannot be determined.

Small differences in the concentration of some major elements/components, e.g. TiO_2 and CaO, between the two metamafic end-members used inevitably resulted to modelled matrix compositions with slightly different trends (e.g. Fig. 2.7e). Comparing the modelled against the measured matrix composition as a whole however reveals similar characteristics regardless of whether the amphibolite block D113-9 (metamafic2A) or the Ep amphibolite block D113-5 (metamafic2EA) is used. The modelled matrix compositions show lower TiO_2, Al_2O_3 (Fig. 2.7a), Zr, La, Th (Fig. 2.7c) than the measured matrix concentration. The concentration of these elements/components in the modelled matrix are more similar to the metamafic and metasedimentary blocks. The CaO (Fig. 2.7d) and SiO_2 (Fig. 2.7e) contents of the modelled matrix meanwhile are intermediate between the metamafic and metasedimentary end-member blocks and higher than the measured matrix. The opposite is true for the concentrations of K_2O, Rb, and BaO in the modelled matrix which are consistently higher in the measured matrix (Fig. 2.7f). The REE (Fig. 2.8e) and extended trace element pattern (Fig. 2.8f) of the modelled matrix also largely reproduced the trends and concentrations observed in the matrix samples. Such signatures include enrichment in

LREEs and Th, and negative anomalies in Eu, Ba, Nb, Sr, and Ti. Difference exists with regard to La and Ta which are slightly enriched relative to Ce and Nb, respectively, in the calculated matrix (Fig. 2.8e, f). Such trend is not observed in the measured matrix data (Fig. 2.8b, d). The use of two different metamafic end-members did not also affect the trace element concentrations and trends of the modelled matrix.

2.6.5 Mass balance calculations: Isocon analysis

The interaction between infiltrating fluids and surrounding wall rock in metasomatic environments such as the slab-mantle wedge interface can result in the removal and/or addition of elements to the surrounding rocks (e.g. Bebout, 2013). The mass change during these metasomatic events can be calculated from the initial and final concentrations of element *i* and the ratio of the final to initial volume of the rock in question (Gresens, 1967; Grant, 1986). Alternatively, the mass change (m_0/m_a) can be calculated graphically by plotting the concentration of each component *i* in the affected (i.e. metasomatized) and in the original rock (unmetasomatized). Connecting the concentration of elements assumed to have not moved during metasomatism (i.e. immobile elements) through the origin defines the isocon line. The relative gain or loss of the other elements can then be calculated using Eqn. 2 (Gresens, 1967; Grant, 1986):

$$\frac{\Delta C_a^i}{C_0^i} = \left(\frac{m_a}{m_0}\right) \cdot \left(\frac{C_a^i}{C_0^i}\right) - 1 \qquad \text{(Eqn. 2)}$$

where C_a^i and C_0^i is the final and initial concentrations of element *i* respectively. The ΔC_a^i is the change in the concentration of element *i* relative to its concentration prior to alteration and (m_0/m_a) is the slope of the isocon line. The Microsoft excel-based EASYGRESGRANT (Lopez-Moro, 2012) was used in the mass balance calculations for the matrix samples assuming TiO_2, Al_2O_3, Cr, Nd, Zr, and Hf as immobile. The modelled composition of the matrix samples is used as the original (unmetasomatized) rock while the measured composition of the samples is considered to be the affected (metasomatized) rock.

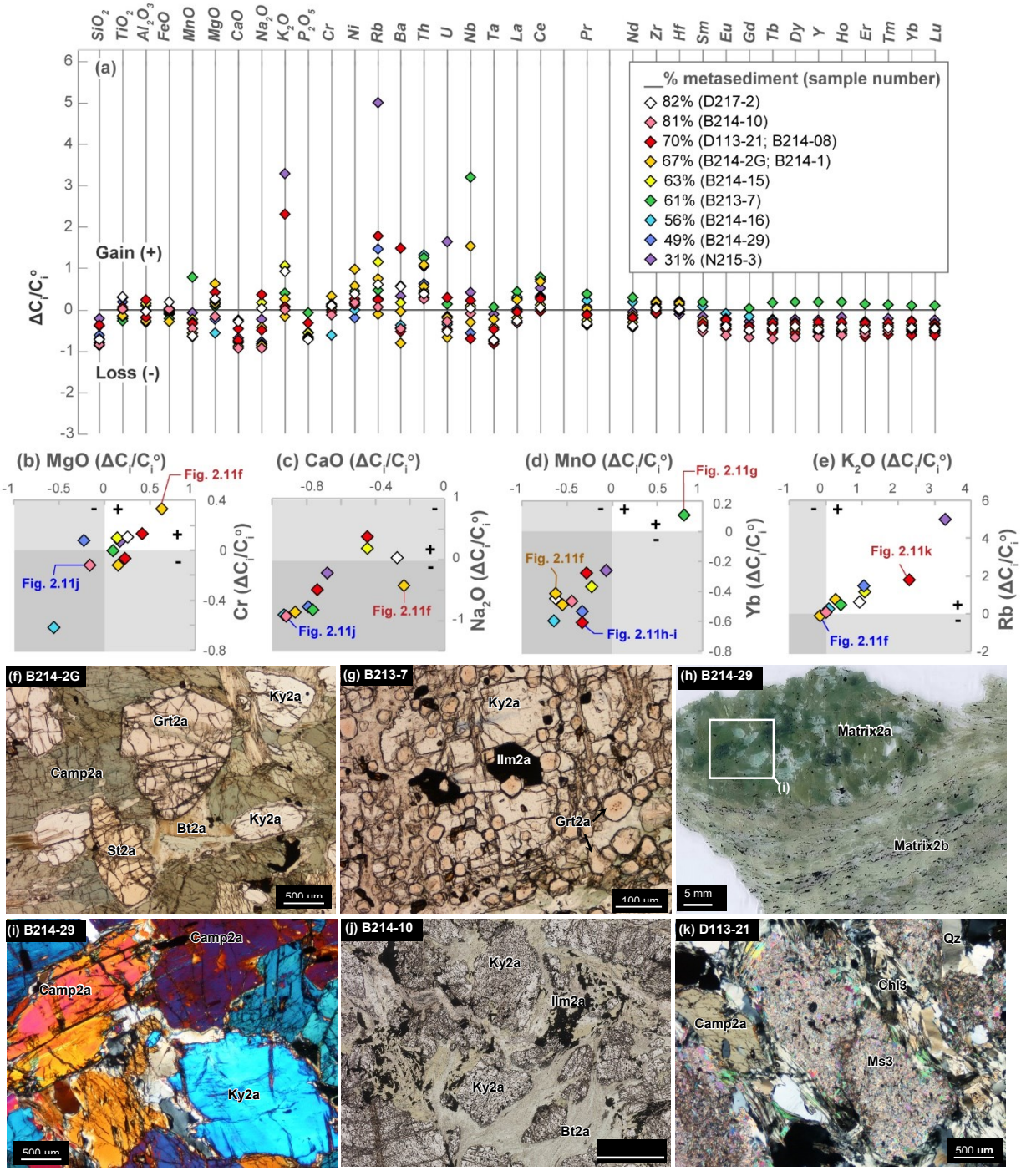

Fig. 2.11. a) Mass balance calculations showing the relative gains (+) and losses (-) in the matrix samples in terms of b) MgO and Cr, c) CaO and Na_2O, d) MnO and Yb, and e) K_2O, Rb. Also indicated are the representative photomicrographs of notable samples which exhibit systematic gains and losses in figures f–k. These samples evidence the strong control of phase assemblage in the early leaching process, and later fluid infiltration. Figs. 2.11f–h, and j are in plane-polarized light while i and k are in crossed polarized light.

The relative gains and losses in the matrix samples calculated graphically from the isocon line is best represented as the ratio of the change in concentration of element *i* to the original concentration of the element ($\Delta C_a^i/C_0^i$), calculated using Eqn. 2 (Fig. 2.11a–e; Lopez-Moro, 2012). The isocon line was defined by fitting TiO_2, Al_2O_3, Cr, Nd, Zr and Hf with a line passing through the origin using the least squared method. Aside from these assumed immobile elements/components, FeO* and the LREEs (except Ce) exhibit general immobility, i.e. showing neither relative gain or loss.

The matrix samples exhibit consistent loss in SiO_2, CaO, and P_2O_5 (Fig. 2.11a). Some matrix samples record gains in MnO, Na_2O, Ba, Nb, Ta, and in M-HREEs while others show relative losses in these elements/components. These relative gains or losses appear to be closely linked to the phase assemblage of the matrix. The garnet-rich matrix2a sample B213-7 (Figs. 2.4f, g, 2.11g), for example, show relative gains in MnO, Nb, Ta and HREEs. Another garnet-bearing matrix 2a-2b sample N215-3 have minimal losses in these elements (Fig. 2.11d). Matrix samples like B214-1, B214-16 and B214-29 (Figs. 2.4h, i, 2.11h), which completely lack garnet, show significant losses in these elements (Fig. 2.11d). An exemption to this is B214-2G (Figs. 2.4e, 2.11f) which contain coarse garnet porphyroblasts but also exhibit loss in Mn and HREEs (Fig. 2.11d). Rutile grains equilibrated with zircon and quartz in this sample however show higher Zr-concentration (= 645 ppm) than rutile found in B213-7 (= 450 ppm) or N215-3 (= 318 ppm). Losses expressed as $\Delta C_a^i/C_0^i$ in terms of MgO, Cr (Fig. 2.11b), CaO, and Na_2O (Fig. 2.11c) are also minimized in hornblende-rich samples such as B214-2G (MgO = +0.63; Cr = +0.33; CaO = −0.24; Na_2O = −0.43; Figs. 2.4d, e, 2.11f) and B217-2 (MgO = +0.26; Cr = +0.11; CaO = −0.28; Na_2O = −0.03), compared to the hornblende-poor matrix sample B214-10 (MgO = −0.16; Cr = −0.11; CaO = −0.92; Na_2O = −0.93; Figs. 2.4l, m, 2.11j) which is largely composed of kyanite and biotite.

All matrix samples exhibit gains in Th and Ce. A few of the matrix samples exhibit loss in K_2O and Rb while the majority record variable gains in these elements. Matrix samples which either incurred a loss in K_2O and Rb (B214-2G) or did not show any change in concentration of these

elements (B214-10) preserve their Stage 2 minerals, especially kyanite (Ky2), compared to the moderate to extensive degree of Stage 3 replacement observed in other matrix samples.

As mentioned above, some of the metamafic blocks exhibit enrichment in LREEs and incompatible elements (e.g. Th) similar to the matrix surrounding them. In the case of B213-9, the whole-rock composition of the core of the block (B213-8) do not show such enriched signatures and preserves a flat REE pattern (Fig. 2.6c,f). In order to determine if the same process which formed the matrix affected this block, we utilized the same procedure of mixing ratio estimation and isocon analysis applied to the matrix samples.

In estimating mixing proportion, the whole-rock composition of the surrounding matrix (B213-7) and the core of the Grt amphibolite block (B213-8) were used as end-members. Cr, Ni, Zr, TiO_2 and Al_2O_3 contents of B213-9 were fitted with variable proportions of metamafic (B213-8) and matrix2a (B213-7). The resulting matrix / (matrix + amphibolite) ratio was low (11%, $r^2 = 0.99$). Mass-balance calculation was done using the kyanite-bearing Grt amphibolite B213-9 as the metasomatized rock volume and the kyanite-free Grt amphibolite block B213-8 as the original (unmetasomatized) composition. The fluid immobile elements/components TiO_2, Al_2O_3, Cr, Nd, Zr, and Hf were also used to fit an isocon through the origin. The results revealed neither gain nor loss in most elements ($\Delta C_a^i/C_0^i = \pm 0.2$) while more mobile elements such as K_2O ($\Delta C_a^i/C_0^i = -0.6$), Rb ($\Delta C_a^i/C_0^i = -0.6$), and P_2O_5 ($\Delta C_a^i/C_0^i = -0.7$) record losses relative to Grt amphibolite block, B213-8.

2.7 Discussion

2.7.1 Origin of the metamafic blocks

The increasing FeO* and TiO_2 (Fig. 2.5e,f) with magmatic differentiation, i.e. increasing FeO*/MgO, observed in the mafic crust of the CPO are consistent with a tholeiitic magmatic series typical of MOR lavas (e.g. Irvine and Baragar, 1971). A MOR tectonic setting of formation is further supported by the Zr-Ti-Y plot where the CPO lithologies fall in the MORB field (Fig. 2.5i), as well as their flat trends in the NMORB-normalized REE diagrams (Fig. 2.6a-c). In contrast to NMORB,

the mafic crust of CPO exhibit enrichment in LILEs such as Rb, Ba, U, Pb and Sr (Fig. 2.6d-f). Earlier works suggest that such enriched signature indicate that these lavas are tholeiites formed in a transitional island arc (IAT) tectonic setting (Keenan et al., 2016; Gibaga et al., 2020). Depletion in HFSEs such as Nb, Ta, Zr characteristic of IAT lavas (Tatsumi, 2005) are however not observed in the mafic crust of the CPO. Alternatively, the LILE enrichment is more likely related to *in situ* hydrothermal alteration of the mafic crust of the ophiolite which is prevalent in mid-oceanic ridge spreading centers (e.g. Bebout, 2013; Starr and Pattison, 2019). This interpretation is also more consistent with its genetic relationship with the metamafic blocks of the Dalrymple Amphibolite discussed below.

The magmatic differentiation trends exhibited by the mafic crust of CPO are largely preserved in the metamafic blocks (Figs. 2.5, 2.6). This is evidenced by the decreasing trend of compatible elements/components such as CaO (Fig. 2.5a), MgO (Fig. 2.5b), Ni (Fig. 2.5c), Cr (Fig. 2.5d) and increase in incompatible elements such as Y (Fig. 2.5g) and Zr (Fig. 2.5h) with increasing FeO*/MgO values. The tholeiitic basalt signature of the mafic crust of CPO, i.e. increasing TiO_2 (Fig. 2.5e) and FeO* (Fig. 2.5f) and flat REE trends (Fig. 2.5a, c, e), are also preserved by most metamafic blocks. Similar enrichments in LILEs such as Rb, Ba, U, Pb, and Sr are also observed in both the mafic crust of CPO and the metamafic blocks (Fig. 2.5b, d, f). These lines of evidence suggest the genetic relationship of the Dalrymple Amphibolite with the mafic crust of CPO. In particular, basaltic lavas similar to the CPO likely served as the protolith for the metamafic blocks. This supports the existing model of a spreading center-turned subduction zone model for the Palawan Ophiolite (Keenan et al., 2016; Dycoco et al., 2021; Valera et al., 2021). According to this model, the Dalrymple Amphibolite represents the subducted oceanic lithosphere whereas the other half of the oceanic lithosphere is now emplaced as the CPO.

The low-Zr metamafic blocks with low concentrations of incompatible elements such as Y (Fig. 2.5g) and Zr (Fig. 2.5h) and higher amounts of Al_2O_3 and CaO (Fig. 2.5a) at a given FeO*/MgO ratio suggest a distinct protolith. These geochemical signatures as well as the positive Eu

and Sr anomalies in the extended trace element plot (Fig. 2.6), and slight depletion in LREEs are comparable to MOR-cumulate gabbros (e.g. Kelemen et al., 1997). These blocks therefore likely represent the metamorphosed equivalent of deeper sections of the subducting oceanic lithosphere, i.e. cumulate gabbro section. Such interpretation is consistent with higher An-content of plagioclases in these block samples compared to other metamafic blocks (Valera et al., 2021) indicating an overall higher CaO/Na_2O budget of their mafic protolith. Lastly, the LREE-enriched blocks exhibit similar REE and extended trace element trends as the metasedimentary blocks and the matrix surrounding the blocks (Fig. 2.6d-f). Their petrogenesis are discussed further in the subsequent section.

2.7.2 Mixing of sedimentary-mafic components: Initial clues and limitations of the modelled matrix composition

The *P-T-D* history of the Dalrymple Amphibolite revealed the timing of deformation events which led to its block-in-matrix configuration (Valera et al., 2021). It was shown that matrix-forming processes started as the whole sequence was being subducted towards peak metamorphic conditions (~700 °C, 13 kbar). The variation in Nb content of rutile grains in the block sample B214-21 (Fig. 2.4p; Valera et al., 2021) provides evidence of the relative timing of mixing between sedimentary and mafic end-members. Rutile included in the garnet core (Stage 1a) has low Nb content and indicates a metamafic protolith while those in the garnet rim and matrix (Stage 1b) record a ten-fold increase in Nb content and plot into the metapelite field (Fig. 2.4p; Valera et al., 2021). The similar peak metamorphic conditions preserved in the matrix compared with the blocks and the successful pseudosection modelling of the matrix2a sample B214-10 by Valera et al. (2021) further indicate that such mixing process in the matrix was largely completed before the sequence reached peak *P-T* condition. The Nb and Cr contents of rutile grains in some blocks especially in B214-13 (Fig. 2.4p) also hint mixing between metamafic and metasedimentary end-member components.

A more comprehensive view on the mixing process that operated in this shear zone can be established by looking at the whole-rock composition of the sheared matrix surrounding the blocks.

The distinct grouping of elements, identified based on their correlation coefficient (Fig. 2.10a), suggests the strong control of two end-member components in the chemistry of the matrix samples. The metasedimentary end-member controlled the Al_2O_3, TiO_2, Zr and LREEs composition (Group 1 elements/components) of the matrix whereas the metamafic end-members (metamafic2A and 2EA) are linked with Group 2 elements/components such as MgO, Cr and Ni (Fig. 2.10b). Such distinct grouping of fluid-immobile elements/components with similar behavior suggests that mechanical mixing of these two end-member components was indeed the predominant process in this slab-mantle wedge interface locality.

In other high-*P/T* type metamorphic terranes, mixing ratios are estimated using stable isotopes of highly siderophile elements (e.g. $^{187}Os/^{188}Os$; Gorman et al., 2019). The limited involvement of ultramafic end-member in the mixing process in the Dalrymple Amphibolite however made application of this technique inappropriate. As discussed in sections 2.6.3 to 2.6.4, this study identified end-members and estimated their mixing ratios using fluid-immobile elements which are representative of each end-member (metased1: Al_2O_3, TiO_2, and Zr; metamafic2A and 2EA: Cr and Ni). The regression analysis using only major and trace elements done in this study, however, has its own limitations. In order to account for the difference in the concentration between the major oxides and trace elements, the ratios Ti/10 and Al/100 were utilized. These values were selected because they represent a satisfactory spread of elements along the linear regression line for most samples (Fig. 2.10b). Changing the denominator values e.g. Al/1000, Ti/100 and Ti/50, Al/500, also changes the value for the best-fit ratio between the end-members albeit mostly within a margin of ±12% except D113-21 (±26%) and B214-16 (±31%). Despite changes in the metased1/(metased1 + metamafic2A or EA) ratios, the relative ranking of the matrix samples with regard to which samples have higher or lower metased1:metamafic2A or EA ratios, is more uniform. The results of mass balance calculations which depend on the modelled matrix composition as the original (unmetasomatized) rock volume, do not also change in terms of elements that were lost or gained.

This limitation nonetheless highlights that the metased1: metamafic2A or EA ratios (Fig. 2.10b, Table 2.5) cannot be treated as absolute values but are better utilized as qualitative measure of mixing between the metasedimentary and metamafic end-members which controlled the chemistry of the matrix of the Dalrymple Amphibolite. The subsequent discussion on mixing and mass balance calculations are therefore drawn considering the metased1/(metased1 + metamafic2A or EA) ratios not as absolute values but rather as qualitative measures of metasedimentary-metamafic ratios. More importantly however, this procedural workflow allowed this study (1) to estimate the 'original' bulk composition of the matrix (i.e. modelled matrix composition), and (2) to distinguish the effect of fluid infiltration through mass balance calculations. The validity of the procedure employed in this study can be assessed by looking at how consistent the modelled matrix composition and mass-balance calculations are with the observed petrological characteristics (section 1.7.4).

The measured whole-rock composition of the matrix records the lowest values in terms of fluid mobile elements such as CaO, SiO_2 and Na_2O (Fig. 2.7d,e). The metasedimentary blocks also register comparably low concentrations of these elements. The measured matrix composition also records pronounced enrichment in some fluid immobile elements/components, most notably Zr and Al_2O_3 (Fig. 2.7a) and less mobile elements La and Th (Fig. 2.7a–c). One possible explanation for such signatures is the preferential leaching of fluid mobile components (e.g. CaO, SiO_2, Na_2O) which left behind more immobile elements/components (e.g. Zr, Al_2O_3). As will be discussed in more detail in the subsequent section, the preferential retention of immobile components such as Al_2O_3 and TiO_2 during leaching is consistent with the abundance of kyanite and ilmenite in the matrix (Table 2.1).

In order to assess the characteristics of the original whole-rock composition of the matrix (i.e. pre-leaching), the modelled matrix composition can be utilized. Notably, the whole-rock CaO, Na_2O (Fig. 2.7d), and SiO_2 (Fig. 2.7e) contents of the modelled matrix is intermediate between the metamafic and metasedimentary blocks. A more CaO- and Na_2O-rich whole-rock composition could explain the abundance of Ca-amphibole in the matrix samples and may reflect its metamafic roots.

This is further supported by the mass balance calculations wherein losses in MgO and Cr (Fig. 2.11b), as well as CaO and Na_2O (Fig. 2.11c) are generally minimized in the hornblende-rich matrix samples (e.g. B214-2G; Fig. 2.4d,e, 2.11f) compared to the hornblende-poor samples (e.g. B214-10; Figs. 2.4l,m, 2.11b,c,j). The similarity in LREE and trace element patterns and concentrations of the modelled (Fig. 2.8e,f) and measured matrix compositions (Fig. 2.8b,d) supports the inference of a metasedimentary end-member in the mixing process. The remarkable similarity in the trace element patterns of the measured and modelled matrix samples and the metasedimentary block N215-4 also indicates the strong control of this end-member on the trace element contents of the matrix. The interpretations drawn from the whole-rock composition of the matrix samples are also consistent with their petrographic characteristics and trace element content of rutile in the matrix.

Exhibiting highly variable mineralogy, most matrix samples consist of minerals more commonly observed in metapelites (e.g. kyanite-biotite in B214-10; Figs. 2.4l,m, 2.11j) as well as assemblages dominated by Ca-amphibole and/or garnet reminiscent of the metamafic blocks (N215-3; Fig. 2.4j,k). This is exemplified by the matrix2a sample B214-2G which contains abundant aluminosilicates (Grt+Ky+St), along with biotite and hornblende (Figs. 2.4d,e, 2.11f) and of B214-29 (Ky+Camp+Oam; Fig. 2.4h,i, 2.11h). The rutile grains of the matrix samples also exhibit variable Nb-Cr concentrations within each sample as well as within a single grain (i.e. core vs. rim). Looking at it as a whole however, the Cr-rich rutile (e.g. N215-3 Cr = 1,115–13,102 ppm), indicating metamafic protolith, and/or Nb-rich rutile (e.g. N213-7 Nb = 4,369–29,695 ppm), typically found in metasedimentary blocks, are both observed in the matrix samples (Fig. 2.4p).

2.7.3 Fluid infiltration: Stages and imprints on the matrix samples

The effect of fluid-rock interaction in the relative gains and losses in certain elements throughout the *P-T-D* history of the Dalrymple Amphibolite was assessed using isocon analysis (Fig. 2.11a–e). Mass balance calculation and the petrological characteristics of the matrix samples suggest distinct stages of fluid infiltration which had contrasting effects on the sheared matrix samples. The presence of ilmenite, kyanite, and zircon in the matrix is consistent with the assumption in the isocon

analysis which considered TiO_2, Al_2O_3, Zr, and Hf as immobile, i.e. retained in the rock as leaching progressed. This is exemplified by the matrix sample B214-10 (Figs. 2.4l,m, 2.11j) dominated by coarse euhedral kyanite and high concentrations of ilmenite in the interstices. The matrix samples also appear to have retained their original FeO* content (Fig. 2.11a). The preferential retention of this relatively mobile element is again most likely due to the widespread stabilization of ilmenite in all matrix samples (Table 2.1). In contrast, other fluid-mobile elements such as SiO_2, CaO and P_2O_5 record losses. The depletion in fluid-mobile components (e.g. CaO, SiO_2, Na_2O) and enrichment in fluid-immobile elements/components especially Al_2O_3, Zr, La, and Th in the measured matrix relative to the modelled matrix indicate the predominant leaching effect of these infiltrating fluids.

The control of phase assemblage on the variable degree of loss of elements in the matrix during the leaching process is even more apparent when we look at the relative loss of Mn, HREEs and Y in the matrix samples (Fig. 2.10b–e). The high correlation coefficients of these elements (Fig. 2.10a) suggest similar behavior which was likely controlled by the presence or absence of garnet in the matrix sample. This is evidenced by the mass balance calculations which feature garnet-rich samples either retaining their original composition (e.g. B213-7; Figs. 2.4f,g, 2.11d,g) or whose losses in these elements are minimal (e.g. N215-3; Figs. 2.4j,k, 2.11d) relative to samples which completely lack garnet (e.g. B214-29; Figs. 2.4h,i, 2.11d,h). Relative losses in the fluid-mobile elements Ca and Na are also apparently linked to the abundance of Ca-amphibole in the matrix samples. As noted above, loss in Ca and Na are minimal in hornblende-rich matrixes (e.g. B214-2G; Figs. 2.4d,e, 2.11c,f), compared to the hornblende-poor matrix sample such as B214-10 (Figs. 2.4l,m, 2.11c,j).

The strong control of phase assemblage in the degree of leaching in matrix samples further suggest that this fluid-infiltration event likely occurred early (Stage 2) in the *P-T-D* history of the Dalrymple Amphibolite, i.e. as the matrix-forming minerals such as kyanite, ilmenite, garnet and hornblende were being formed. The variable degree of loss in some elements (e.g. CaO, NaO, M-HREEs, Y) from the matrix of the Dalrymple Amphibolite indicates that the stabilization of sink

minerals (e.g. Al_2O_3 in kyanite; TiO_2 and FeO* in ilmenite) is required prior to the leaching process for the retention of these elements within the matrix (Figs 2.12a, c, d). Such fluid-infiltration may have been promoted by the shearing and mixing of metasedimentary and metamafic end-members, as the slab-mantle wedge interface lithologies were being deformed into its current block-in-matrix configuration (Fig. 2.12 c,d). Losses during this early fluid infiltration are more uniform among matrix samples, that is the values of $\Delta C_a^i/C_0^i$ are relatively small ranging from 0 to -1 (Fig. 2.11b–e), suggesting the pervasive nature of the fluid infiltration.

The early timing of fluid infiltration resulting in leaching of certain elements from the original matrix samples is supported by the high degree of loss in Mn, HREEs and Y recorded by B214-2G (Figs. 2.6e; 2.11d) compared to B213-7 (Figs. 2.6g, 2.11d). Both are garnet-rich samples and contain rutile grains equilibrated with zircon and quartz. The rutile grains in B214-2G hosted in hornblende and garnet record higher Zr content indicating a higher peak *T* (~730 °C at 13 kbar) compared with B213-7 (~700 °C at 13 kbar; Fig. 2.11a). This possibly indicates that the infiltrating fluids may have already leached out Mn, HREEs and Y from B214-2G before it crystallized the rutile-hosting hornblende and garnet at higher *T*. Early crystallization of garnet in B213-7 enabled the retention of these elements, which is supported by low-Zr rutile grains (i.e. low-*T* rutile grains) found in this sample (Fig. 2.12a). The estimated *P*-*T* conditions of fluid infiltration and leaching are close to the peak metamorphic conditions recorded in the matrix (Stage 2; Fig. 2.1c) and are consistent with the interpretations of Valera et al. (2021) that matrix-forming processes (i.e. mixing, fluid infiltration, and deformation) were active as the sequence was being subducted towards greater depths.

Similar to the leaching out of fluid-mobile elements/components (e.g. SiO_2 and CaO), losses in K_2O, Ba, and Rb were likely originally preserved in the matrix sample. This is still recorded in B214-2G (Fig. 2.7d) whose Stage 2 phase assemblage records minimal replacement by Stage 3 minerals. In other matrix samples, however, moderate to advanced imprints of Stage 3 masked this leaching signature as gains in fluid mobile elements/components K_2O, Rb, and Ba (Fig. 2.11e). This is supported by the increase in the concentration of these elements/components in matrix samples

(e.g. D113-21; Figs. 2.4n,o, 2.7f, 2.11k) with higher degree of Stage 3 replacement (especially muscovite) compared to other samples which preserved their Stage 2 mineral assemblages. This is consistent with the strong correlation between the K_2O, Rb and Ba contents of the matrix samples with one another but not with other fluid-mobile elements (e.g. CaO and SiO_2; Fig. 2.10a). These lines of evidence suggest a later fluid infiltration event related to the retrograde metamorphism of the Dalrymple Amphibolite as the mélange sequence was being exhumed towards the surface (Fig. 2.12a). Valera et al. (2021) described low-salinity aqueous fluid inclusions related to the growth of kyanite-replacing muscovite. The gains associated with Stage 3 minerals are also much more variable, i.e. $\Delta C_a^i/C_0^i$ = 0 to +3.29 for K_2O, compared to the losses due to early fluid-infiltration. This possibly reflect the limited nature of this retrograde event as evidenced by the variable degree of replacement in the matrix samples (e.g. kyanite by muscovite).

2.7.4. Assessing Mixing, fluid Infiltration, Leaching, and Deformation (MILD) processes in the slab-mantle wedge interface

In the calculations presented above, a single metasedimentary and metamafic end-member were used to reproduce the calculated composition of all matrix samples. However, in an actively deforming shear zone, an end-member (e.g. metamafic) can be added into the mixing zone incrementally as distinct "batches" instead of being consumed in a single deformation event. Looking at the whole-rock composition of the matrix samples allowed the evaluation of mechanical mixing between end-member components but masked the finer details of how such process progressed. The product of initial stages of mixing, i.e. a hybridized matrix, can also be recycled and used as raw material to be deformed, mixed, and reacted with infiltrating fluids (Fig. 2.12d). This scenario is supported by the two distinct generations of matrix observed in Botoon and Nanad where the earlier formed matrix2a are transformed into blocks themselves and surrounded by matrix2b. In the mixing-isocon analyses done for the Grt amphibolite block B213-9 (Fig. 2.2c–f), the use of the surrounding matrix (B213-7) and the core of the block (B213-8) largely reproduced its whole-rock composition aside from losses in more fluid mobile elements/components (e.g. K_2O, P_2O_5, and Rb).

These preferential losses in fluid-mobile elements/components from the margin of the blocks are likely related to leaching by infiltration of fluids.

Accounting the contributions of deformation, mixing, and fluid-rock interaction in the slab-mantle wedge interface is therefore complicated by its cyclical feedback nature. The procedure outlined in this study, while simplistic, is thus meant to provide a workflow in the study of matrix formation in slab-mantle wedge interface localities especially those dominated by mafic and sedimentary end-members. Indeed, future works gathering more block and matrix samples and employing other geochemical techniques (e.g. stable isotope geochemistry) are expected to refine end-member identification and estimation of mixing ratios, albeit still as a cumulative and not incremental effect. More importantly, the notable consistency between the interpretations for the matrix petrogenesis (i.e. mixing-leaching) and its petrological characteristics (i.e. phase assemblage), whole-rock data (measured vis-à-vis modelled), and mineral chemistry (e.g. Nb-Cr contents of rutile) give merit to the procedural workflow employed in this study. Application of this procedure to other slab-mantle wedge localities may help in distinguishing end-member components, estimating their mixing ratios, and determining the effects of infiltrating fluids.

2.7.5 MILD processes in slab-mantle wedge interfaces and its implications to arc magmatism

The cooler paleogeothermal gradient preserved in the Dalrymple Amphibolite compared to typical metamorphic soles (e.g. Semail Ophiolite; Soret et al., 2017) suggests that it represents the slab-mantle wedge interface of an arc already in transition from the much warmer conditions during subduction initiation (Valera et al., 2021; Fig. 2.12a,b). The mixing process between metasedimentary-metamafic end-members observed in the Dalrymple Amphibolite also differs from typical high-*P/T* type metamorphic terranes thought to dominate developed subduction zones (e.g. Bebout and Penniston-Dorland, 2016; Agard et al., 2018). In such environments, the colder, wetter conditions allow the prevalence of lower-*T* phases such as serpentine and chlorite derived from the ultramafic end-member, i.e. serpentinized mantle wedge (e.g. Guillot et al., 2009).

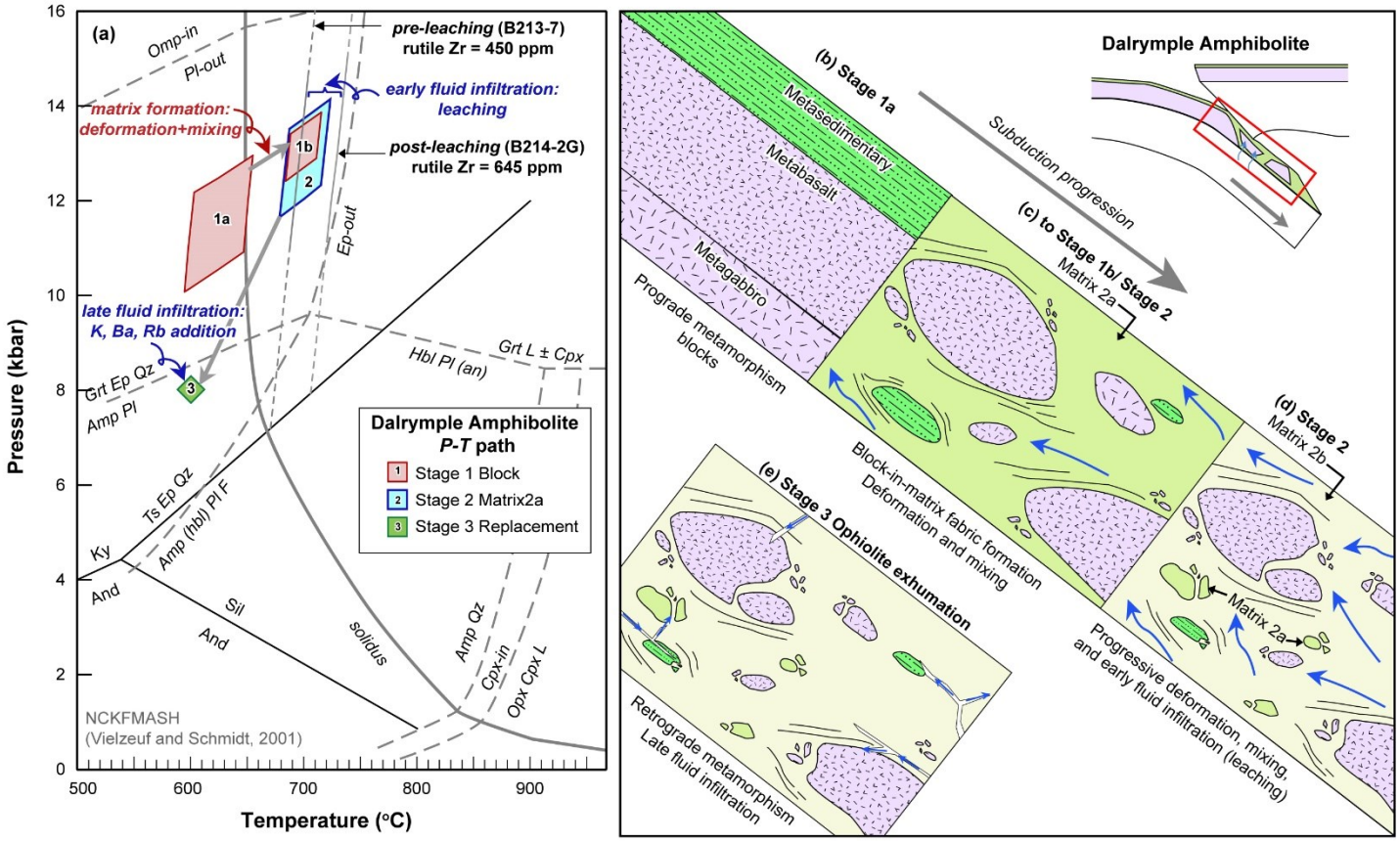

Fig. 2.12. a) Updated *P-T* history of the Dalrymple Amphibolite (modified from Valera et al., 2021) and its b–e) schematic representation. b,c) One evidence on the approximate timing of matrix formation as the sequence was subducted towards peak *P-T* conditions is the ten-fold increase in Nb content of rutile grains included in Stage 1b garnet relative to those in the garnet core (Stage 1a; Fig. 2.4p). The timing of early fluid infiltration (Fig. 2.12a, c, d) was constrained by the mean maximum Zr content of rutile (cf. Penniston-Dorland et al., 2018) in B213-7 and B214-2G. B213-7 did not reflect losses in garnet-related elements (i.e. MnO, HREEs; Fig. 2.11d) while B214-2G which exhibits notable losses in these elements recorded higher peak *P-T* conditions marking the maximum *P-T* conditions by which time leaching has already commenced (Fig. 2.12a, c, d). The peak *T* for B214-2G is slightly higher than those constrained for Stage 2 by Valera et al. (2021) albeit *P* cannot be constrained for this sample. This early fluid infiltration therefore likely started close to or at peak *P-T* conditions (Stage 2; Fig. 2.12c, d) possibly promoted by the extensive deformation of the sequence at this time. e) Finally, during ophiolite exhumation (Stage 3), later fluid infiltration resulted in the growth of replacement minerals (e.g. muscovite), and the addition of fluid mobile elements/components such as K_2O, Ba, and Rb in the matrix samples. Blue arrows in Figs. 2.12c–e represent infiltrating fluid.

Recent studies dealing with the petrogenesis of the surrounding matrix in slab-mantle wedge interface complexes (e.g. Gorman et al., 2019) mainly utilized stable isotopes (e.g. $^{187}Os/^{188}Os$) and highly siderophile trace elements (e.g. platinum group elements) to elucidate petrogenetic processes preserved in these rocks. This procedure has been done in relatively well studied localities such as the Monviso Eclogite in western Alps (e.g. Angiboust et al., 2014), and the Attic-Cycladic Complex in Syros, Greece (Gorman et al., 2019). Although most high-*P*/*T* type metamorphic terranes do preserve an ultramafic-derived matrix, this does not fully encapsulate other possible mixing scenarios in the slab-mantle wedge interface.

Empirical (Nielsen and Marschall, 2017) and experimental (Codillo et al., 2018) analyses of global arc lavas, clearly show the important role of the crustal section (i.e. sediments and mafic basalts) of the down-going slab to account for variations in the arc magma chemistry. Early stages of subduction characterized by warmer geothermal gradients than what is observed in developed arcs and early dehydration at shallower depths, limit the formation of low-*T* phases such as serpentine and chlorite along the slab-mantle wedge interface of an incipient arc. Indeed, these common matrix-forming minerals (chlorite, serpentine, and talc) are only stable in mature arcs characterized by high-*P/T* metamorphic field gradients (Agard et al., 2016).

If the serpentinization of the overlying mantle wedge is not pervasive, deformation along the slab-mantle wedge interface is likely accommodated by the crustal section of the down-going slab (e.g. Agard et al., 2016; Valera et al., 2021). Observations of metamorphic soles in some ophiolites (e.g. Semail Ophiolite) show that in such scenarios, shearing is accommodated by the deformation of rheologically weaker sediments (e.g. Soret et al., 2017). The chemistry of the matrix comprising the subduction channel during incipient subduction will therefore represent the mixture of crustal components while the contribution of the ultramafic end-member will likely be minimal (Fig. 2.12c). The type of end-members constituting the matrix of the Dalrymple Amphibolite and the high metased1: metamafic2A or EA ratio support such scenario.

The petrological characteristics of the matrix surrounding the blocks of the Dalrymple Amphibolite thus provide a unique perspective on sediment- and mafic-dominated slab-mantle wedge interface. Based on the characteristics of the matrix of this mélange sequence, relatively stiff minerals such as kyanite, Ca-amphibole, and garnet are more prevalent than softer, more magnesian minerals i.e. serpentine, talc and chlorite. A similar observation was noted for the matrix surrounding the amphibolite blocks of Catalina Schist (Penniston-Dorland et al., 2018). The mixing between sediment and mafic end-members also has implications on the elements that are retained and those that are mobilized during the interaction of such matrix with infiltrating fluids.

In the case of the Dalrymple Amphibolite, fluid infiltration at relatively high *P-T* conditions (~700 °C, 13 kbar) at relatively shallow depths (~45 km) resulted in the preferential leaching of fluid mobile elements/components (e.g. SiO_2, Na_2O, K_2O, Ba) while more immobile elements/components are retained (e.g. Al_2O_3, Zr, Th) and enriched in the matrix. As these fluids ascend towards shallower depths, they will likely interact and react with the mantle wedge lithologies in the hanging wall. It must be noted however, that this study deals with processes occurring at relatively shallower depths (~45 km) beneath an incipient arc with a high paleogeothermal gradient (~16 °C/km). The generally cooler geothermal gradients in more developed arcs may result to deeper depths of devolatilization and therefore different fluid properties and composition (e.g. Manning and Frezzotti, 2020). The local temperature-depth structure of the subduction system for example may affect the preferential stabilization of certain sink minerals and thus affect which elements are leached out and which are retained as was shown for the Dalrymple Amphibolite. Considering these caveats, the interaction between fluids similar to what is reported here and the overlying mantle material may explain, at least in part, signatures observed in arc volcanic rocks and subarc mantle xenoliths.

Ba-enriched, Th-depleted fluids were likely produced during the leaching process of the matrix in the Dalrymple Amphibolite. If such type of fluid reacts with the mantle wedge it may explain the Ba-rich, Th-poor ‘shallow subduction component’ found in most arcs (e.g. Elliot et al., 2003; Pearce

et al., 2005; Manning and Frezzotti, 2020). These shallow subduction components are thought to be transported by dilute, aqueous fluids released from the downgoing slab during metamorphic devolatilization at depths of around ~20–70 km, depending on the local *P/T* gradient (e.g. Manning and Frezzotti, 2020). Retention and enrichment of Th on the matrix of the Dalrymple Amphibolite after leaching on the other hand, ensures its availability during melting and/or devolatilization of the slab at deeper levels (>90 kms, Manning and Frezzotti, 2020). Melt and/or fluid derived from this Th-rich matrix material, considering that Th-sink minerals are stabilized, could explain the Th-enriched 'deep (>90 km) subduction component' also reported in most arcs (e.g. Elliot et al., 2003). A more direct evidence of the interaction between the mantle wedge and percolating Si- and Na-rich hydrous fluids has also been documented in a number of subarc xenolith localities (e.g. Western Pacific arcs; Arai and Ishimaru, 2008). Silica enrichment is typically observed as the growth of secondary orthopyroxenes at the expense of olivine (e.g. Batanes; Valera et al., 2019) while the crystallization of hydrous minerals such as phlogopite and/or pargasite in mantle wedge xenoliths (e.g. Pinatubo; Payot et al., 2018) attests to the interaction of percolating cation-rich hydrous fluids with mantle wedge lithologies albeit at deeper depths than those in this study (~45 km).

References

Agard, P., Plunder, A., Angiboust, S., Bonnet, G., Ruh, J., 2018. The subduction plate interface: Rock record and mechanical coupling (from long to short timescales). Lithos 320–321, 537–566.

Agard, P., Yamato, P., Soret, M., Pringent, C., Guillot, S., Plunder, A., Dubacq, B., Chauvet, A., Monie, P., 2016. Plate interface rheological switches during subduction infancy: Control on slab penetration and metamorphic sole formation. Earth and Planetary Science Letters 451, 208–220.

Angel, R.J., Mazzuccheli, M.L., Alvaro, M., Nestola, F., 2017. EoSFit-Pinc: A simple GUI for host-inclusion elastic thermobarometry. American Mineralogist 102, 1957–1960.

Angiboust, S., Pettke T., Hoog, J.C.M., Caron, B., Oncken, O., 2014. Channelized fluid flow and eclogite-facies metasomatism along the subduction shear zone. Journal of Petrology 55, 883–916.

Arai, S., Ishimaru, S., 2008. Insights into petrological characteristics of the lithosphere of mantle wedge beneath arcs through peridotite xenoliths: A review. Journal of Petrology 49, 665–695.

Bebout, G.E., 2013. Metasomatism in subduction zones of subduction zones of subducted oceanic slabs, mantle wedges, and the slab-mantle interface *In*: Harlov, D.E., Austrheim, H. Metasomatism (eds.) Metasomatism and the chemical transformation of rock. Lecture notes in Earth system sciences, Springer-Verlag Berlin Heidelberg, 289–349.

Bebout, G.E., Barton, M.D., 2002. Tectonic and metasomatic mixing in a High-*T*, subduction-zone melange – Insights into the geochemical evolution of the slab-mantle interface. Chemical Geology 187, 79–106.

Bebout, G.E., Penniston-Dorland, S.C., 2016. Fluid and mass transfer at subduction interfaces - The field metamorphic record. Lithos 240–243, 228–258.

Codillo, E.A., Le Roux, V., Marschall, H.R., 2018. Arc-like magmas generated by melange-peridotite interaction in the mantle wedge. Nature Communications 9, 1–11.

Droop, G.T.R., 1987. A general equation for estimating Fe^{3+} concentrations in ferromagnesian silicates and oxides from microprobe analyses, using stoichiometric criteria. Mineralogical Magazine 51, 431–435.

Dycoco, J.M.A., Payot, B.D., Valera, G.T.V., Labis, F.A.C., Pasco, J.A., Perez, A.d.C., Tani, K., 2021. Juxtaposition of Cenozoic and Mesozoic ophiolites in Palawan island, Philippines: New insights on the evolution of the Proto-South China Sea. Tectonophysics 819, 229085.

Elliot, T., 2003. Tracers of the Slab. In: Eiler, J. (Ed.) Inside the subduction factory. Geophysical Monograph 138, American Geophysical Union, Washington D.C. 23–45.

Encarnacion, J.P., Essene, E.J., Mukasa, S.B., Hall, C.H., 1995. High-pressure and -temperature subophiolitic kyanite-garnet amphibolites generated during initiation of Mid-Tertiary subduction, Palawan, Philippines. Journal of Petrology 36, 1481–1503.

Gerya T., Stöckhert, B., Perchuk, A.L., 2002. Exhumation of high-presure metamorphic rocks in a subduction channel: A numerical simulation. Tectonics 21, 1–15.

Gibaga, C.R., Arcilla, C.A., Hoang, N., 2020. Volcanic rocks from the Central and Southern Palawan Ophiolites, Philippines: Tectonic and mantle heterogeneity constraints. Journal of Asian Earth Sciences: X. 4, j.jaesx.2020.100038

Gorman, J.K., Penniston-Dorland, S.C., Marschall, H.R., Walker, R.J., 2019. The roles of mechanical mixing and fluid transport in the formation of reaction zones in subduction-related mélange: Evidence from highly siderophile elements. Chemical Geology 2019, 96–111.

Grant, J.A.,1986. The isocon diagram – a simple solution to Gresen's equation for metasomatic alteration. Economic Geology 81, 1976–1982.

Gresens, R.L., 1967. Composition-volume relationships of metasomatism. Chemical Geology 2, 47–65.

Gromet, L.P., Dymek, R.F., Haskin, L.A., Korotev, R.L., 1984. The "North American Shale Composite": its compilation, major and trace element characteristics. Geochimica et Cosmochima Acta 48, 2469–2482.

Guillot, S., Hattori, K., Agard, P., Schwartz, S., Vidal, O., 2009. Exhumation processes in oceanic and continental subduction contexts: A review *In*: Lallemand, S., Funiciello, F. (eds.) Subduction zone geodynamics. Springer-Verlag Berlin Heidelberg, 175–205.

Hofmann, A.W., 1988. Chemical differentiation of the Earth: The relationship between mantle, continental crust and oceanic crust. Earth and Planetary Science Letters 90, 297–314.

Irvine, T.N., Baragar, W.R.A., 1971. A guide to the chemical classification of the common volcanic rocks. Candian Journal of Earth Sciences 8, 523–548.

Kapp, P., Manning, C.E., Tropper, P., 2009. Phase-equilibrium constraints on titanite and rutile activities in mafic epidote amphibolites and geobarometry using titanite-rutile equilibria. Journal of Metamorphic Geology 27, 509–521.

Keenan, T.E., Encarnacion, J., Buchwaldt, R., Fernandez, D., Mattinson, J., Rasoazanamparany, C., Leutkemeyer, P.B., 2016. Rapid conversion of an oceanic spreading center to a subduction zone inferred from high-precision geochronology. Proceedings of the National Academy of Sciences 113, E7359–E7366.

Kelemen, P.B., Koga, K., Shimizu, N., 1997. Geochemistry of gabbro sills in the crust-mantle transition zone of the Oman ophiolite: Implications for the origin of the oceanic lower crust. Earth and Planetary Science Letters 146, 475–488.

Labis, F.A.C., Payot, B.D., Valera, G.T.V., Pasco, J.A., Dycoco, J.M.A., Tamura, A., Morishita, T., Arai, S., 2020. Melt-rock interaction in the subarc mantle: Records from the plagioclase

peridotites of the southern Palawan Ophiolite, Philippines. International Geology Review 63, 1067–1089.

Leake, B.E., Woolley, A.R., Arps, C.E.S., Birch, W.D., Gilbert, M.C., Grice, J.D., Hawthorne, F.C., Kato, A., Kisch, H.J., Krivovichev, V., Linthout, K., Laird, J., Mandarino, J.A., Maresch, W.V., Nickel, E.H., Rock, N.M.S., Schumacher, J.C., Smith, D.C., Stephenson, N.C.N., Ungaretti, L., Whittaker, E.J.W., Youzhi, G., 1997. Nomenclature of amphiboles: Report of the subcommittee on amphiboles of the international mineralogical association, commission on new minerals and mineral names. The Canadian Mineralogist 35, 219–246.

Li, C.F., Xu, X., Lin, J., Sun, Z., Zhu, J., Yao, Y.J., Zhao, X.X., Liu, Q.S., Kulhanek, D.K.,Wang, J., Song, T.R., Zhao, J.F., Qiu, N., Guan, Y., Zhou, Z., Williams, T., Bao, R., Briais, A., Brown, E., Chen, Y., Clift, P., Colwell., F., Dadd, K., Ding, W., Almeida, I., Huang, X., Hyun, S., Jiang, T., Koppers, A., Li, Q., Liu, C., Liu, Z., Nagai, R., Peleo-Alampay, A., Su, X., Tejada, M., Trinh, H., Yeh, Y., Zhang, C., Zhang, F., Zhang, G., 2014. Ages and magnetic structures of the South China Sea constrained by deep tow magnetic surveys and IODP Expedition 349. Geochemistry, Geophysics, Geosystems 15, 4958–4983.

Lopez-Moro, F.J., 2012. EASYGRESGRANT – A Microsoft Excel spreadsheet to quantify volume changes and to perform mass-balance modeling in metasomatic systems. Computer and Geosciences 39, 191–196.

Manning, C.E., Frezzotti, M.L., 2020. Subduction-zone fluids. Elements 16, 395–400.

Marschall, H.R., Schumacher, J.C., 2012. Arc magmas sourced from melange diapirs in subduction zones. Nature Geoscience 5, 862–867.

Meinhold, G., Anders, B., Kostopoulos, D., Reischmann, T., 2008. Rutile chemistry and thermometry as provenance indicator: An example from Chios Island, Greece. Sedimentary Geology 203, 98–111.

Nakashima, T., Shimoda, G., Tatsumi, Y., 2000. Porphyritic magnesian andesites in the Setouchi Volcanic Belt, SW Japan. Bulletin of the Volcanological Society of Japan 45, 259–269.

Nielsen, S.G., Marschall, H.R., 2017. Geochemical evidence for mélange melting in global arcs. Science Advances 3:e1602402, 1–6.

Payot, B.D., Arai., S., Yoshikawa, M., Tamura, A., Okuno, M., Rivera, D.J.V., 2018. Mantle evolution from ocean to arc: The record in spinel peridotite xenoliths in Mt. Pinatubo, Philippines. Minerals 8, 1–16. Doi: 10.3390/min8110515.

Peacock, S., Wang, K., 1999. Seismic consequences of warm versus cool subduction metamorphism: Examples from Southwest and Northeast Japan. Science 286, 937–939.

Pearce, J.A., Cann, J.R., 1971. Ophiolite origin investigated by discriminant analysis using Ti, Zr, and Y. Earth and Planetary Science Letters 12, 339–349.

Pearce, J., Stern, R., Bloomer, S., Fryer, P., 2005. Geochemical mapping of the Mariana arc-basin system: Implications for the nature and distribution of subduction components. Geochemistry, Geophysics, Geosystems 6 (2004GC000895).

Penniston-Dorland, S.C., Gorman, J.K., Bebout, G.E., Piccoli, P.M., Walker, R.K., 2014. Reaction rind formation in the Catalina Schist: Deciphering a history of mechanical mixing and metasomatic alteration. Chemical Geology 384, 47–61.

Penniston-Dorland, S.C., Kohn, M.J., Piccoli, P.M., 2018. A melange of subduction temperatures: Evidence from Zr-in-rutile thermometry for strengthening of the subduction interface. Earth and Planetary Science Letters 482, 525–535.

Sachs, L., 1984. Applied statistics: A handbook of techniques, 2nd Ed. Spriver-Verlag, New York, 1–707.

Schumacher, J.C., 1991. Empirical ferric iron corrections: Necessity, assumptions and effects on selected geothermobarometers. Mineralogical Magazine 55, 3–18.

Shimoda, G., Nagai.M., Morishita, Y., 2004. Rare earth elements compositions of Setouchi high Mg andesites (HMAs) and basalt; an implication for a mantle compositional shift beneath the SW Japan arc during the Japan Sea opening. Bulletin of the Geological Survey of Japan 55, 31–38.

Soret, M., Agard, P., Dubacq, B., Plunder, A., Yamato, P., 2017. Petrological evidence for stepwise accretion of metamorphic soles during subduction infancy (Semail ophiolite, Oman and UAE). Journal of Metamorphic Geology 35, 1051–1080.

Starr, P.G., Pattison, D.R.M., 2019. Metamorphic devolatilization of basalts across the greenschist-amphibolite facies transition zone: Insights from isograd mapping, petrography and thermodynamic modelling. Lithos 342–343, 295–314.

Tatsumi, Y., 2005. The subduction factory: How it operates in the evolving Earth. GSA Today 15, 10:1130/1052-5173.

Tomkins, H. S., Powell, R., Ellis, D. J., 2007. The pressure dependence of the zirconium-in-rutile thermometer. Journal of Metamorphic Geology 25, 703–713.

Ulmer, P., Trommsdorff, V., 1995. Serpentine stability to mantle depths and subduction-related magmatism. Science 268, 858–861.

Valera, G.T.V., Kawakami, T., Payot, B.D., 2021. The slab-mantle wedge interface of an incipient subduction zone: Insights from the *P-T-D* evolution and petrological characteristics of the Dalrymple Amphibolite, Palawan Ophiolite, Philippines. Journal of Metamorphic Geology. DOI: 10.1111/jmg.12644, 1–33.

Valera, G.T.V., Payot, B.D., Arai, S., Takeuchi, M., Ishimaru, S., Tamura A., 2019. Petrologic nature of the active subarc crust-mantle boundary: Mixed magmatic-metasomatic processes recorded in xenoliths from Sabtang island, Luzon arc. Journal of Volcanology and Geothermal Research 374, 80–99.

Whitney, D.L., Evans, B.W., 2010. Abbreviations for names of rock-forming minerals. American Mineralogist 95, 185–187.

Yumul, G.P.Jr., Dimalanta, C.B., Gabo-Ratio, J.A.S., Queaño, K.L., Armada, L.T., Padrones, J.T., Faustino-Eslava, D.V., Payot, B.D., Marquez, E.J., 2020. Mesozoic rock suites along western Philippines: Exposed proto-South China Sea fragments? Journal of Asian Earth Sciences: X 4, 100031.

Zack, T., Moraes, R., Kronz, A., 2004. Temperature dependence of Zr in rutile: Empirical calibration of a rutile thermometer. Contributions to Mineralogy and Petrology 148, 471–488.

Conclusions

The *P-T-D* history of the Dalrymple Amphibolite underlying the Palawan Ophiolite are discussed in Part 1 of this thesis. The prograde *P-T* path preserved in the metamafic blocks indicate cooler paleogeothermal gradients (~16 °C/km) compared to typical metamorphic soles (>20 °C/km). The peak *P-T* conditions of the metamafic blocks, i.e. amphibolites, Ep amphibolites and Grt amphibolites, and the surrounding matrix are also shown to be similar (~700 °C, 13 kbar). The block-in-matrix structure of the Dalrymple Amphibolite indicates that this complex likely represents the slab-mantle wedge interface of a subduction zone already in its infancy. Field characteristics, matrix2a *P-T* conditions and Cr and Nb contents of rutile grains indicate that the matrix-forming deformation likely started prior to the rock sequence reaching peak metamorphic conditions at depths of approximately ~45 km. Deformation events accompanying each metamorphic stage also affected the textural and petrological characteristics of this block-in-matrix sequence. Multiple generation of veins and lenses of veins cross-cutting the block-in-matrix sequence reveal the important role of fluids in material transfer along the slab-mantle wedge interface throughout its history. The petrological characteristics and *P-T-D* history of the Dalrymple Amphibolite therefore provide important insights on the nature of the slab-mantle wedge interface of an arc with intermediate *P/T* geothermal gradients which is prevalent during incipient subduction and in warm subduction complexes.

The protolith of the metamafic blocks and the petrogenetic processes preserved in the matrix which comprise the Dalrymple Amphibolite are discussed in Part 2. The metamafic blocks are genetically related to the basalts and gabbros comprising the crustal section of Palawan Ophiolite. The metamafic blocks represent the metamorphosed crustal section of the subducting slab, while the Palawan Ophiolite basalts constitute the unmetamorphosed lithologies of the hanging wall. Both mafic lithologies indicate a mid-oceanic ridge basalt signature with possible indication of seafloor hydrothermal metamorphism marked by enrichment in large ion lithophile elements.

The matrix surrounding the blocks reflects the complex interplay of deformation in this shear zone, mixing of mafic and sedimentary crustal components, and leaching and addition of elements by different generations of infiltrating fluids. In an attempt to decipher the effects of these processes in the whole-rock geochemistry of the matrix, geostatistical, regression and isocon analyses were employed. The results indicate the predominant effect of mixing between metamafic and metasedimentary components in controlling its major and trace element content. The crustal end members identified for the matrix of the Dalrymple Amphibolite with its intermediate paleogeothermal gradient (~16 °C/km) contrast with typical high-*P*/*T* type metamorphic terranes which feature a matrix derived from mixed ultramafic-sedimentary units.

A fluid infiltration event likely occurred during the deformation and mixing of crustal components in the shear zone. This event resulted in the preferential leaching not only of fluid mobile components (e.g. CaO and SiO_2) but also other elements/components not utilized by the crystallizing minerals in the matrix. During the exhumation of the CPO with the Dalrymple Amphibolite at its base, a subsequent fluid infiltration event led to the retrograde metamorphism of the Dalrymple Amphibolite resulting in the addition of K_2O, Rb, and Ba in the whole-rock composition of the matrix as replacive minerals (e.g. muscovite). The exhumation of the ophiolite (i.e. obduction) onto the NPCT is linked to the complete subduction of the oceanic lithosphere in the leading edge of NPCT.

Similar mixing, deformation, and fluid-related mass transfer processes likely operate in other slab-mantle wedge interface localities and actively control the petrological and geochemical signatures of the matrix of these mélange sequences. Fluids infiltrating and interacting with this matrix material with mixed composition, in particular, may preferentially leach some elements and retain and enrich others depending on the stable phase assemblage in the matrix thus gaining distinct geochemical signatures. As these fluids rise along the slab-mantle wedge interface and react with the overlying mantle material, some of these distinct signatures may be imprinted on the mantle wedge and consequently affect arc magma chemistry.